In Situ TEM Investigation on Mechanical Behaviors of Metallic Nanocrystals at the Atomic Scale

by

Sixue Zheng

B.S., Nanjing University of Science and Technology, 2016

M.S., University of Science and Technology of China, 2019

Submitted to the Graduate Faculty of the

Swanson School of Engineering in partial fulfillment

of the requirements for the degree of

Doctor of Philosophy

University of Pittsburgh

2023

UNIVERSITY OF PITTSBURGH

SWANSON SCHOOL OF ENGINEERING

This dissertation was presented

by

Sixue Zheng

It was defended on

February 6, 2023

and approved by

William S. Slaughter, PhD, Associate Professor, Department of Mechanical Engineering and Materials Science

Qihan Liu, PhD, Assistant Professor, Department of Mechanical Engineering and Materials Science

Guangyong Li, PhD, Associate Professor, Department of Electrical and Computer Engineering

Dissertation Director: Guofeng Wang, PhD, Professor, Department of Mechanical Engineering and Materials Science

In Situ TEM Investigation on Mechanical Behaviors of Metallic Nanocrystals at the Atomic Scale

Sixue Zheng, PhD

University of Pittsburgh, 2023

The mechanical reliability of nanoscale metals is a precondition for electronic devices to function well. Deep insights into the mechanical behaviors of metallic nanocrystals are critical for their practical application. In this dissertation, transmission electron microscopy (TEM)-based *in situ* nanomechanical testing is used to investigate the atomic-scale mechanical behaviors of metallic nanocrystals.

Thickening, resulting from pure displacive or diffusive mechanisms, is frequently observed in nanoscale metals during compression. Thus far, the compressive behaviors of metallic nanocrystals, mediated by coupled displacive-diffusive mechanism, remain unexplored. Here, it is found that preexisting dislocations and dislocation slip act as stimuli to activate surface diffusion causing consecutive thinning in silver nanocrystals during compression. As the nanocrystal width reduces to a critical value, surface-diffusion-mediated compression fracture occurs. These findings shed light on atomic-scale diffusion-mediated compressive behavior of metallic nanocrystal.

Fivefold twins are frequently observed in various nanostructured metals. However, the formation mechanisms of fivefold twin remain largely unclear, due to the lack of atomic-scale observation of their dynamic formation process. Here, it shows that sequential twinning slip in varying slip systems and the decomposition of high-energy grain boundary account for the fivefold twin formation in a nanoscale gold single crystal under bending as well as the reversible formation and dissolution of fivefold twin in the nanocrystal with preexisting twin under tension and

shearing. Moreover, the complex stress state in the neck area facilitates fivefold twin formation in a bi-twinned gold nanocrystal, disobeying Schmid law. These findings provide atomic-scale insights into the formation process of high-order twin structures in nanostructured metals

The high-temperature mechanical behaviors of nanoscale metals remain largely unexplored due to the technical limitations. Here, a *in situ* high-temperature nanomechanical testing method based on electric current-induced Joule heating is proposed. By this method, it is found that deformation twinning, phase transformation and dislocation slip sequentially occur in the tungsten nanocrystal at elevated temperature. Such ductile behavior is related to the loading orientation and the experimental temperature.

This dissertation advances the current understanding of the atomic-scale mechanical behaviors of metallic nanocrystals, which is crucial for developing mechanically reliable electronic devices.

Table of Contents

List of Tables

List of Figures

Preface

I would like to take this opportunity to express my deepest gratitude to many people who have helped me during my PhD study. Without their support, this research project would not have been possible. First and foremost, I am deeply grateful to my advisor, Professor Scott X. Mao, who admitted me four years ago. His exceptional insights into the mechanics of materials, rigorous scrutiny into details, contagious enthusiasm for high standard research and frequent inspiration for research orientation enlighten my academic life.

Deep gratitude is also due to my advisor, Professor Guofeng Wang, for his unqualified support, invaluable instructions and meaningful discussions for my research. His patience, his terse style of writing, his noble mortality and his way of interacting people make me cannot stop learning from him. I thank Guofeng for his encouragement and dedicated cultivation during my PhD study.

My sincere thanks and appreciation also go to the other members of my supervisory committee, Professor Qihan Liu, Professor William S. Slaughter and Professor Guangyong Li, for their insightful discussions and precious advice on both my research and dissertation.

Special thanks to my collaborators on multiple projects. Thank Dr. Shuhei Shinzato and Professor Shigenobu Ogata at Osaka University, for their great efforts on molecular dynamics simulation and helpful discussions on analyzing the surface diffusion in metallic nanocrystals; Thank Professor Chuang Deng at University of Manitoba and Professor Christopher R. Weinberger at Colorado State University for their great work on atomic-scale simulation and helpful discussions on the formation mechanisms of fivefold twin in gold nanocrystals.

Same acknowledgement goes to Professor Susheng Tan in Petersen Institute of Nanoscience and Engineering at University of Pittsburgh for his generous help and technical assistance on the operation of FEI Titan TEM.

Special thanks to my group members: Boyang Li, Ying Fang, Zhengwu Fang and Dr. Xiang Wang for their helpful discussion, assistance on my experiments and support on my research. I would also like to convey thanks to my friends: Dr. Zhijie Wang, Yuan Gao, Dr. Xing Wang, Wen Dong, Hao Chen and Dr. Yixuan Wang for their generous help in my life. I'm also grateful for my supervisors in Office of the Provost at University of Pittsburgh, Jennifer Macro and Jennifer Decima, for their generous help and support on the data analysis for student engagement during the program of 2022 summer internship in higher education.

Finally, I would like to thank my family for their unconditional love, especially my wife Yuzhuo Pan. Their unconditional love, support, understanding and encouragement have been and will always be the motivation for me to advance. This dissertation is dedicated to all of them.

1.0 Introduction

With the rapid advances in the field of nanotechnology, a spectrum of nanoscale materials, such as nanoparticles, nanotubes, nanowires, nanofibers and nanoribbons, have emerged, and their synthesis, characterization and application have drawn tremendous interest over the past decades[1, 2, 3, 4, 5, 6, 7, 8, 9]. Due to the small size scale and the ultrahigh surface-to-volume ratio, nanoscale materials possess extraordinary physical properties, such as high electrical conductivity[10, 11, 12, 13], high transparency[6, 8, 14, 15] and remarkable mechanical properties with high strength (~several GPa) and considerable ductility (25%-126%)[16, 17, 18]. Owing to these excellent properties that arise in extremely small volume, nanoscale metal materials are envisioned as promising building blocks in flexible and stretchable electronics[11, 19, 20, 21, 22, 23]. For instance, gold (Au) nanowires with the diameter of ~3 nm have been used as a critical component of a wearable pressure sensor[24]. In a practical application, the materials in microelectronics often serve under various mechanical loading conditions, such as stretching, bending and twisting[12, 20, 25, 26, 27, 28]. Mechanical degradation probably occurs in the nanoscale metals after long term service, which deteriorates their mechanical integrity and electrical stability and threats the service life of the devices. The reliability of nanomaterial-enabled flexible and stretchable electronics calls for a thorough understanding of the mechanical behaviors of nanoscale metal materials. Similar to the physical properties, the mechanical behaviors of nanoscale metal materials differ from their bulk counterparts distinctly[17, 29, 30, 31, 32]. Given that the experimental investigations of the mechanical behaviors of nanomaterials is still in its infancy, significant effort should be dedicated to studying the processes responsible for plastic deformation and the underlying atomic-scale mechanisms,

which is of vital importance for not only material modification and but also the successful design and reliable operation of electronics.

Metallic nanocrystals often surprise us with unexpected mechanical behaviors, due to the pronounced surface effect on plastic deformation[33, 34, 35]. The under-coordinated atoms at the nanocrystal surface tend to minimize surface energy, creating an ultrahigh tensile surface stress, which breaks atomic bonding and facilitates the activation of surface mass transport[36, 37, 38]. With decreasing the size of metallic nanocrystals, diffusional deformation is expected to occur and even dominate over crystal slip[38, 39, 40]. However, how surface atom diffusion mediates the plastic deformation of nanoscale metals remains largely unclear, due to the technical difficulty in fabricating nanoscale metals without surface contamination using focused ion-beam (FIB) milling[41, 42, 43, 44]. Moreover, the free surface of metallic nanocrystal, serving as both the source and drain for dislocations, mediates displacive plasticity (e.g. perfect dislocation slip and deformation twinning), due to the scarcity of the effective dislocation sources (e.g. Frank-Read source and single arm source) in the small volume[45, 46, 47, 48, 49, 50]. The surface nucleation and glide of dislocations may give rise to the formation of high-order defects, such as multifold twin[51, 52, 53]. The formation mechanism of multifold twin under mechanical loading, however, has not been fully elaborated, due to the lack of direct atomic-scale observation of their dynamic formation process.

Owing to the extremely small sample size, the difficulty in fabricating high quality sample with the appropriate microstructure and the lack of reliable clamping method for mechanical testing, investigating the mechanical behaviors of metallic nanocrystals is technically demanding, especially at the atomic scale[54]. The current understanding on the atomic-scale mechanical behaviors heavily relies on Molecular dynamics (MD) simulations. Limited by the computational

resources, MD simulations are normally conducted at high strain rates of 10^7-10^9/s, which fall short in investigating the diffusional deformation of nanocrystals unless at elevated temperature[40, 43, 55, 56, 57]. Moreover, atomistic simulations are often subject to validity issues due to the inaccuracies in interatomic potentials[58, 59, 60] and the uncertainty in sample geometry[61, 62, 63]. Recently, with the help of a Nanofactory scanning tunneling microscope (STM) holder and micro-electromechanical systems (MEMS), advanced *in situ* TEM testing techniques with superior temporal resolution and the capability of observing microstructural and morphological evolutions at the atomic scale were successfully developed for investigating the mechanical behaviors of metallic nanocrystals[30, 64, 65]. Although significant progress has been made for *in situ* room-temperature nanomechanical testing, the real-time high-temperature mechanical investigation of metallic nanocrystals at the atomic scale remains an experimental challenge, which necessitates the development of new testing methods and/or tools.

In this dissertation, high resolution transmission electron microscopy (HRTEM)-based *in situ* nanomechanical tests are conducted on the nanoscale silver (Ag), platinum (Pt), Au at room temperature. Moreover, a *in situ* atomic-scale high-temperature testing method is proposed for investigating the mechanical behaviors of nanoscale tungsten (W) at elevated temperature. The atomic-scale dynamic process of the compressive deformation of Ag and Pt nanocrystals, the fivefold twin formation in nanoscale Au under mechanical loading and the high-temperature ductile deformation in W nanocrystal are directly visualized, and the underlying mechanisms are discussed. This dissertation is organized as follows.

In Chapter 2, surface-mediated plastic deformation in nanoscale metals, twinning behaviors in face-centered cubic (FCC) and body-centered cubic (BCC) nanostructured metals and the previous *in situ* techniques developed to investigate the mechanical behaviors of small-sized

materials are reviewed. Based on the literature review, the research objectives of this dissertation are proposed.

Chapter 3 introduces the materials adopted in this research and the experimental procedures, including sample preparation, experimental setup and *in situ* nanomechanical testing inside TEM.

Chapter 4 reports the compressive deformation behaviors of nanoscale FCC metals. Abnormal thinning and tensile-fracture-like failure, mediated by coupled displacive-diffusive mechanisms, occur in Ag nanocrystals, while local thickening, resulting from dislocation slip, occurs in Pt nanocrystals. Whether thinning or thickening occurs in the nanoscale metals depends on the competition between the rates of thinning by surface diffusion and thickening by crystal slip, which are related to the sample dimensions, the applied strain rate and the type of materials.

Chapter 5 focuses on the atomic-scale dynamic process of fivefold twin formation inside the small volume of FCC nanocrystals. Combining both *in situ* TEM observation and atomistic simulations, it is found that sequential twinning slip in varying slip systems and the decomposition of high-energy grain boundaries account for the fivefold twin formation in nanoscale Au under mechanical loading. Moreover, the complex stress state in the neck area of a Au nanocrystal with a twin boundary parallel to the loading direction results in the formation of fivefold twin, which is not expected by Schmid's law.

In Chapter 6, a *in situ* high-temperature mechanical testing method based on the effect of electric current-induced Joule heating is proposed to investigate the high-temperature ductile behaviors of BCC metals at the atomic scale. Deformation twinning, BCC-FCC-BCC phase transformation and perfect dislocation slip are observed to sequentially occur in the W nanocrystal at elevated temperature. The operating deformation modes in W nanocrystals are related to the

loading orientation and the experimental temperature. The new testing methodology proposed in this chapter tackles the technical difficulties associated with investigating the atomic-scale ductile behaviors of BCC metals at elevated temperature.

Finally, the conclusions of this dissertation are summarized in Chapter 7 and the future research directions are proposed in Chapter 8.

2.0 Background

(*Portions of this chapter have been reproduced with permission from Extreme Mechanics Letters, Volume 45, Page 101284. Copyright 2021 by Elsevier.*)

In this chapter, the surface-mediated deformation in nanosized materials will be firstly reviewed. Then, the twinning-related mechanical behaviors of nanostructured metals will be summarized. Additionally, current testing methods for investigating the atomic-scale deformation behaviors of small-sized metals will be briefly introduced. Finally, current research limitations will be discussed and the research objectives in this dissertation will be proposed.

2.1 Surface-Mediated Displacive And Diffusive Plasticity In Metallic Nanocrystals

2.1.1 Pure Displacive And Diffusive Mechanisms In Nanoscale Metals

Based on the variation of atomic registries during plastic flow, the deformation mechanisms of metal materials are classified into displacive, diffusive and coupled displacive-diffusive mechanisms[66]. Displacive deformation, such as dislocation slip and deformation twinning, is prevalent in solid metals at room temperature, where dislocation is a major carrier of plastic deformation. The behavior of dislocations can be influenced by the characteristic size of the metal materials. In bulk metals, dislocations are usually generated by Frank-Read source[67], grain boundary (GB)[68, 69], the intersection between GB and twin boundary (TB)[70, 71, 72], or other preexisting defects/interfaces[73, 74]. In the micron- and submicron-sized metallic crystals,

dislocations are generated by the operation of single-arm dislocation source, also referred to as truncated Frank-Read source[75, 76, 77]. As the feature size drops below a few tens of nanometers, surface dislocation nucleation is the dominant mechanism[30, 63, 78, 79]. Zheng *et al.*[80] directly demonstrated that free surface, serving as both the source and drain for dislocations, mediated the plastic deformation of sub-10-nm Au nanocrystals (Figure 2.1). During tensile test, significant stress concentration appeared in the area close to the surface step (Figure 2.1d), enabling the surface step to be a preferable dislocation nucleation site. Upon the yielding of the Au nanocrystal, a leading partial dislocation nucleated at the favorable surface site and then glided through the nanocrystal, leaving behind a stacking fault (SF), as shown in Figure 2.1a-b. After the surface-mediated dislocation slip, part of the strain energy in the nanocrystal was released, reducing the elastic lattice strain near the surface step from 0.048 to 0.028 (Figure 2.1d-f). With further deformation, a trailing partial nucleated at the same surface site as the leading partial, and then eliminated the SF (Figure 2.1c). Consequently, a perfect dislocation slip, composed of a 30° leading and 90° trailing partial slipping, occurred in the Au nanocrystal (Figure 2.1c).

Displacive and diffusive deformations are generally viewed as two major competing mechanisms of plastic deformation in metal materials. Displacive deformation is the dominant mechanism at room temperature, causing that atomic registries change collectively and deterministically. By contrast, diffusive deformation, a time-dependent process, often occurs in metal materials at moderate and high temperatures, causing that the atoms move in a chaotic and random manner [66, 81, 82, 83, 84]. In addition to the experimental temperature, sample size is also a critical factor deciding the operative deformation mode in metallic nanocrystal during mechanical test. As the crystal size goes down to a characteristic length scale, diffusive deformation could be activated to dominate plastic deformation at room temperature, especially for some metal materials

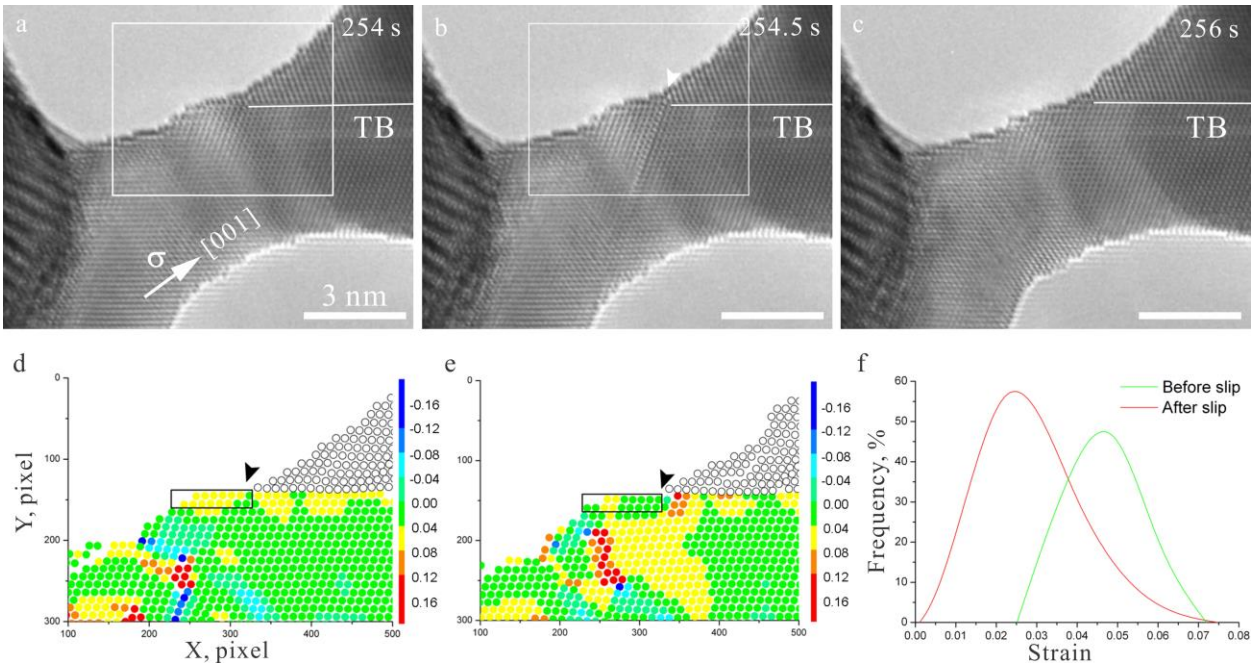

Figure 2.1 Surface dislocation nucleation in a Au nanocrystal[59]. (a-c) Sequential HRTEM images showing the surface nucleation and glide of dislocations in the Au nanocrystal under <001>- tensile loading at room temperature under a strain rate of ~10^{-3} s^{-1}. Scale bars are 3 nm. (d-e) The strain mappings of the white-boxed areas in a and b. The black arrowheads indicate the dislocation nucleation site. (f) A quantitative analysis of the lattice strain gauge (black-boxed region in d and e). Frequency is the number of atoms with that strain divided by the total number of atoms in the lattice strain gauge.

with a low melting point[82]. Owing to the high surface-to-volume ratio of the metallic nanocrystals, a large proportion of the constituent atoms are at free surface[81, 85, 86], which are under-coordinated and tend to reduce surface energy, creating a surface stress. As the crystal size decreases to a few nanometers, the ultrahigh surface stress, which is inversely related to the sample size[63, 79, 87, 88], could break surface atomic bonds and subsequently gives rise to diffusional mass transport along nanocrystal surface[65, 82, 83]. Thus, not only the displacive plasticity but also the diffusional plasticity can be mediated by the free surface of the metallic nanocrystals at room temperature. Sun *et al.*[89] revealed that a sub-10 nm Ag nanoparticle was deformed like a liquid droplet but maintained a

crystalline structure in the interior of the nanoparticle without displacive deformation during cyclic compression and stretching (Figure 2.2a-j), which was mediated by the diffusional events at the free surface and the heterogeneous interfaces. Besides, a number of *in situ* tensile tests of Cu, Ag and Au nanowires (NWs) revealed that crystalline liquid-drop-like retraction behaviors occurred in the fractured NWs after tensile failure, which was mediated by curvature-driven surface atom diffusion[36, 38, 89, 90, 91, 92]. The atoms at the high-curvature sites continuously moved to the locations with low curvatures in the nanotips, causing that the fractured tips retracted rapidly with length reduction and diameter expansion (Figure 2.2k-m). Consequently, surface atom diffusion contributed to the ultralarge contraction strain of the fractured nanowires and resulted in the

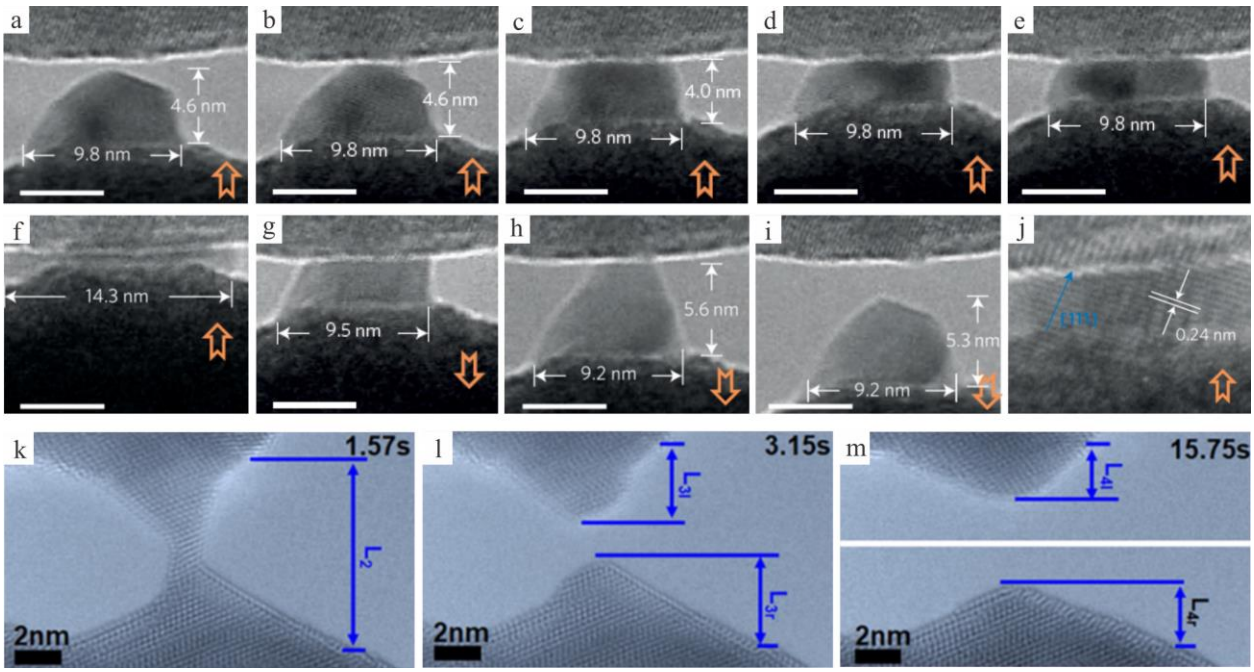

Figure 2.2 Pure diffusion-mediated deformation in nanoscale metals. (a-i) Sequential HRTEM images showing the shape evolution of the Ag nanocrystal during compression (a-f) and streching (g-i)[89]. The shape change of the nanocrystal is reversible during cyclic deformation. All the scale bars are 5 nm. (j) TEM image showing the deformed Au nanocrystal is highly crystalline[89]. (k-m) Atomic-scale images of the contraction process of the fractured Au nanowire mediated by surface atom diffusion[36].

formation of the nanotips with a round and smooth shape. Along with the transition from displacive- mechanism-dominated plasticity to diffusive-mechanism-dominated plasticity, the strength-size relation changes from Hall-Petch-type strengthening ('smaller is stronger') to inverse Hall-Petch relation ('smaller is much weaker'), as demonstrated by Tian *et al.*[66] in tin (Sn) nanopillars.

Based on the above discussion that deformation mechanism changes from displacive to diffusive mechanisms with decreasing the sample size, there may exist a crossover regime where displacive and diffusional plasticity both thrive in metallic nanocrystals similar to bulk nanocrystalline metals[93, 94, 95] (Figure 2.3). Given that free surface plays an essential role in mediating both displacive and diffusive plasticity, displacive mechanisms may cooperate with diffusive mechanisms to mediate the deformation of nanoscale metals within a critical size regime. It naturally raises the question whether the coupled displacive-diffusive deformation can replace pure crystal slip or diffusional creep to be the dominant deformation mode in nanoscale metals.

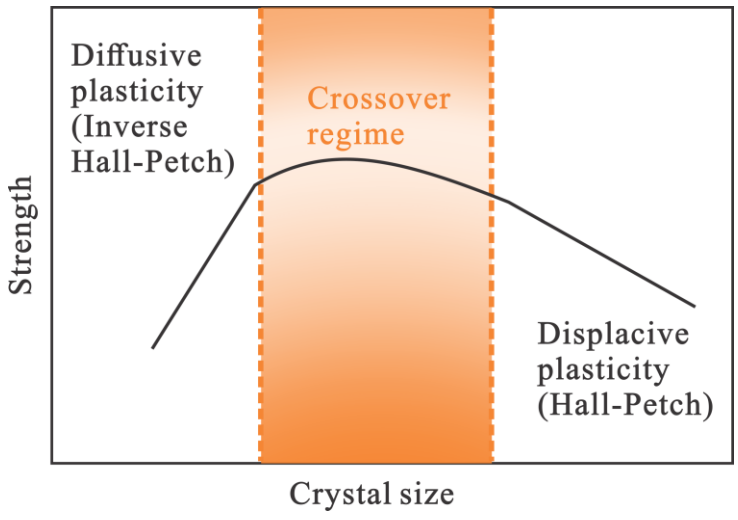

Figure 2.3 Schematic illustration of deformation mechanism change from displacive to diffusive mechanisms with decreasing sample size. There may exist a crossover regime where coupled displacive-diffusive mechanism is dominant.

What are the mechanical behaviors of nanoscale metals, mediated by the coupled displacive-diffusive deformation mechanism? This will be discussed in **2.1.2**.

2.1.2 Coupled Displacive-Diffusive Mechanisms In Nanosized Metals

In addition to the size-dependent competition, a cooperative interplay between diffusive and displacive deformations could occur in metallic nanocrystals during mechanical loading. Zhong *et al*.[38] revealed that coupled displacive-diffusive mechanism dominated the plastic deformation of Ag nanocrystals over a sample diameter range. Upon tensile loading, a full dislocation slip event led to the formation of an atomic-scale surface step with the step height of one atomic layer (Figure 2.4a). Compared to the surface atoms elsewhere, the chemical potentials of the atoms at the step edge were much higher, favoring the migration of surface atoms from the step edge towards the end of the Ag nanocrystal, which lowered the overall system energy. The successive occurrence of stress- and curvature-driven surface atom diffusion at the edge of the surface step resulted in the experimental observation of the continuous lateral movement of the surface step (Figure 2.4a-c). Consequently, the coupled displacive-diffusive mechanism maintained a relatively smooth surface morphology and prevented the tendency of plastic instability, contributing to the room-temperature super-elongation of the Ag nanocrystals within a critical size regime. In addition, Sun *et al*.[96] found that partial dislocation slip could also activate surface atom diffusion via introducing a surface step with a height of one-third of one atomic layer. Compared to the other surface atoms, the atoms at the step edge were of a lower coordination number and suffered from a higher chemical potential, favoring the initiation of atom diffusion at free surface during tensile loading. In addition to the slip-activated surface atom diffusion, the localized diffusion of surface atoms could also influence dislocation behaviors, as demonstrated by Cao *et al*.[97] in the tensile tests of

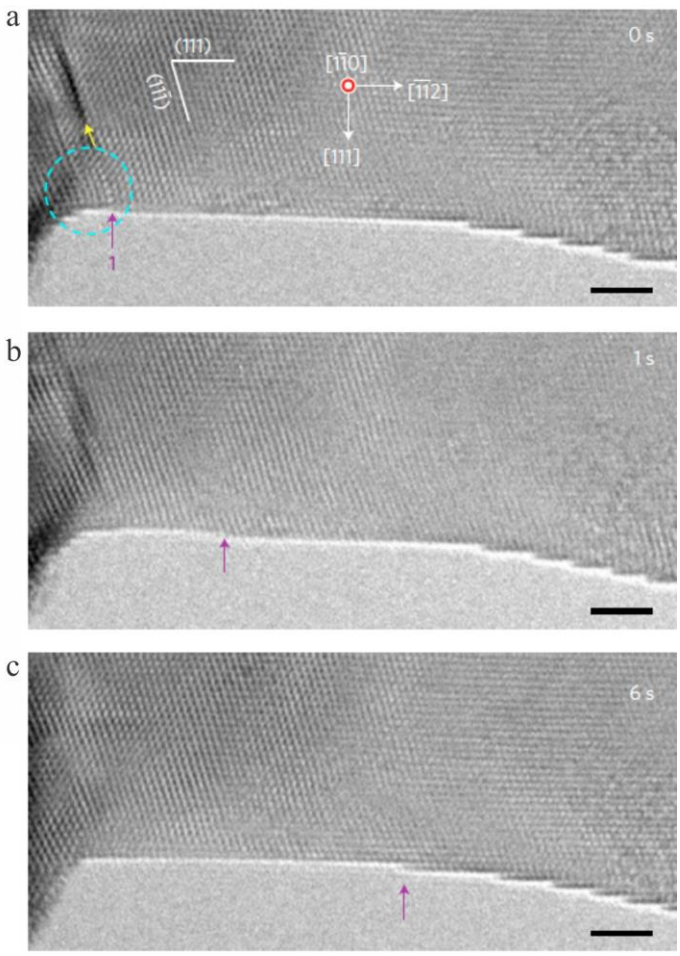

Figure 2.4 Slip-activated surface diffusional creep in a 20-nm Ag nanocrytal during tensile loading[38]. (a-c) Continuous migration of a atomic-scale surface step towards the end of the nanocrystal, assisted by surface atom diffusion. All the scale bars are 2 nm.

Au nanowires. Surface diffusion of individual atoms occurred occasionally, which smoothed surface contour via changing the height and length of the surface steps (Figure 2.5a-b). Such change in the local surface morphology alleviated the stress concentration near the surface steps (Figure 2.5c-d), therefore eliminating the possibility of dislocation nucleation and the subsequent deformation localization at the same surface site.

In summary, considerable efforts have been devoted to investigating surface-mediated displacive and diffusive plasticity in nanoscale metals. Thus far, most research efforts focus on the

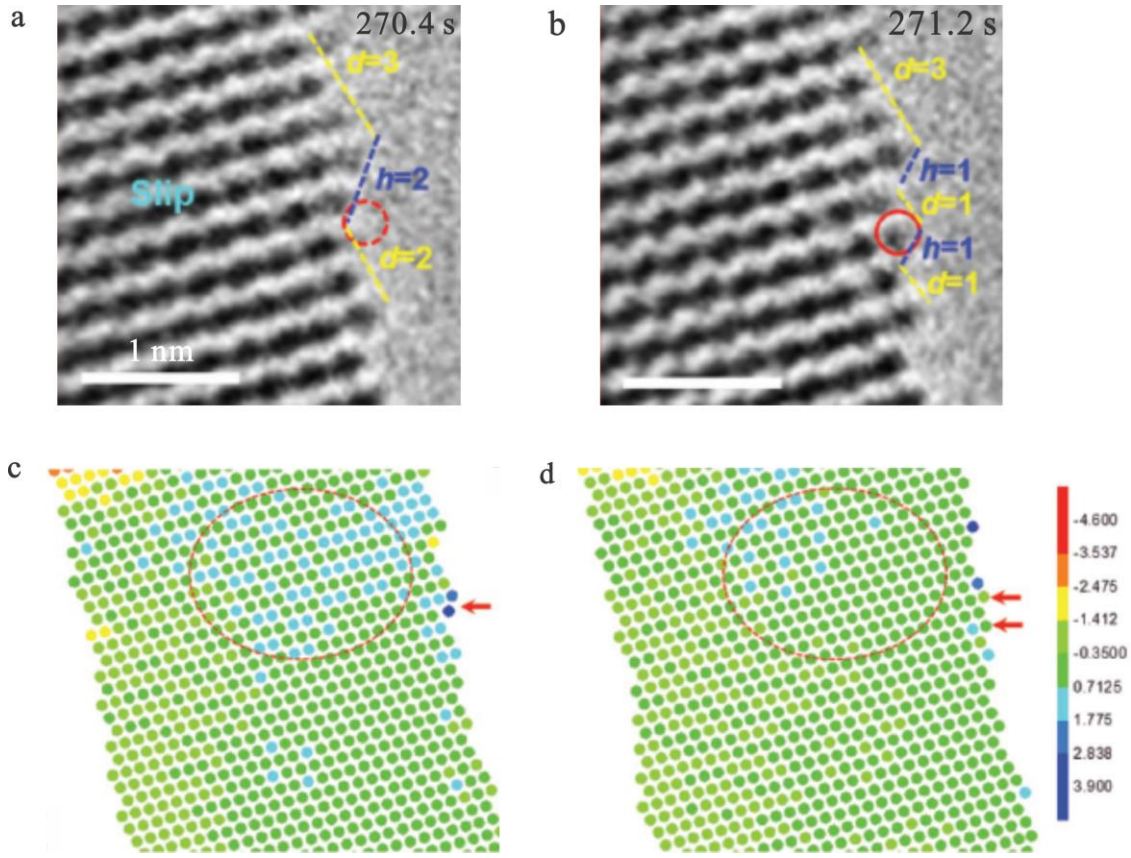

Figure 2.5 The influence of localized diffusion of surface atoms on dislocation nucleation in Au NWs[97]. (a-b) TEM images showing the surface morphology of the Au nanowire before (a) and after (b) surface diffusion. The surface step (step height (h)=2 and step depth (d)=2) decomposes into two small surface steps (h=1,d=1) after localized surface atom diffusion. The red circles with dashed and solid lines represent the surface site before diffusion and new atomic column after diffusion, respectively. The scale bars are 1 nm. (c-d) Quantitative lattice strain analysis on the Au nanowire showing that localized surface diffusion eliminates the stress concentration at the surface step (indicated by the red arrows).

role of diffusional deformation in the tensile deformation behaviors of nanoscale metals. The influence of diffusive mechanisms on the compressive deformation behaviors of metallic nanocrystals remains largely unexplored, especially at the atomic scale, due to the technical difficulties in fabricating and testing the nanoscale metals with clean surface. In addition, some previous studies reported that either pure displacive or pure diffusive mechanisms led to the thickening of nanoscale metals during compression[40, 98]. It naturally raises the question that how the coupled diffusive–displacive process mediates the compressive deformation of nanoscale metals. Moreover, it remains unclear how the diffusive process mediates the compressive deformation of the metallic nanocrystals without GBs and heterogeneous interfaces serving as highways for mass transport. MD simulation has been proved to be an effective method to investigate the atomic-scale mechanical behaviors of small-sized metals. However, suffering from the extremely high strain rate (usually 10^7 /s–10^9 /s), diffusional deformation in MD simulations is not obvious unless at elevated temperature[57, 99]. The current research fundings from computational studies are questionable to be directly extrapolated to those under ambient laboratory conditions. Given that the occurrence of surface diffusional creep severely threatens the long-term shape stability of the nanoscale metals[89], profound insights into the diffusional deformation are of vital importance for the precise shape control of nanostructured metals, guaranteeing the reliability of nanoscale electronic devices in a practical application.

2.2 Deformation Twinning In Nanostructured Metals

2.2.1 Deformation Twinning In FCC Metals

As a common and important mode of plastic deformation in metal materials, deformation twinning has been the subject of ongoing discussions[69, 70, 99, 100]. Deformation twinning in bulk FCC metals has been well documented and summarized in the previous studies. Numerous experimental and computational studies indicate that the twinnability (twinning tendency) of a FCC polycrystalline metal materials is largely determined by its stacking fault energy (SFE)[101, 102, 103, 104, 105, 106, 107], strain rate[108], experimental temperature[109, 110] and grain size[111, 112]. Low SFE, high strain rate, cryogenic test temperature and small grain size (<100 nm) are believed to be the favorable conditions for activating deformation twinning as the major carrier of plasticity in bulk FCC metals. Under mechanical loading, deformation twin nucleates and then thickens through the layer-by-layer movement of partial dislocations[58, 113, 114, 115], as demonstrated by Seo *et al.*[114, 116] in Au nanowires, Sedlmayr *et al.*[117] in Au nanowhiskers, and Kim *et al.*[118, 119] in aluminum (Al) nanowires. In contrast to the classical layer-by-layer twinning route, Wang *et al.* [120] recently revealed a new route for deformation twinning in FCC nanocrystalline Pt. A three-layer twin embryo was nucleated through the formation of two stacking faults (SFs) separated by one atomic layer (Figure 2.6a-b) and the subsequent partial dislocation slip between these two previously formed SFs (Figure 2.6c). Not only twin nucleation but also twin growth in the nanostructured metals could proceed unfollowing the classical layer-by-layer fashion. Sun *et al.*[95] observed that partial dislocations randomly nucleated from the surface of Ag nanowires and glided on non-neighboring planes[121], leading to a high density of SFs, as shown in Figure 2.6d-f. With further tensile loading, the slip of partial dislocations between the separated SFs resulted in the ultimate

formation of a single deformation twin, as shown in Figure 2.6g-i. The atypical twinning routes in the nanostructured metals may be facilitated by the local stress concentration at GBs and surface steps, which effectively bypasses the high stacking fault energy and the activation energy barrier for dislocation nucleation.

As a special morphology of deformation twinning, multifold twinned structures are frequently observed in both annealed and deformed FCC metal materials with low stacking-fault

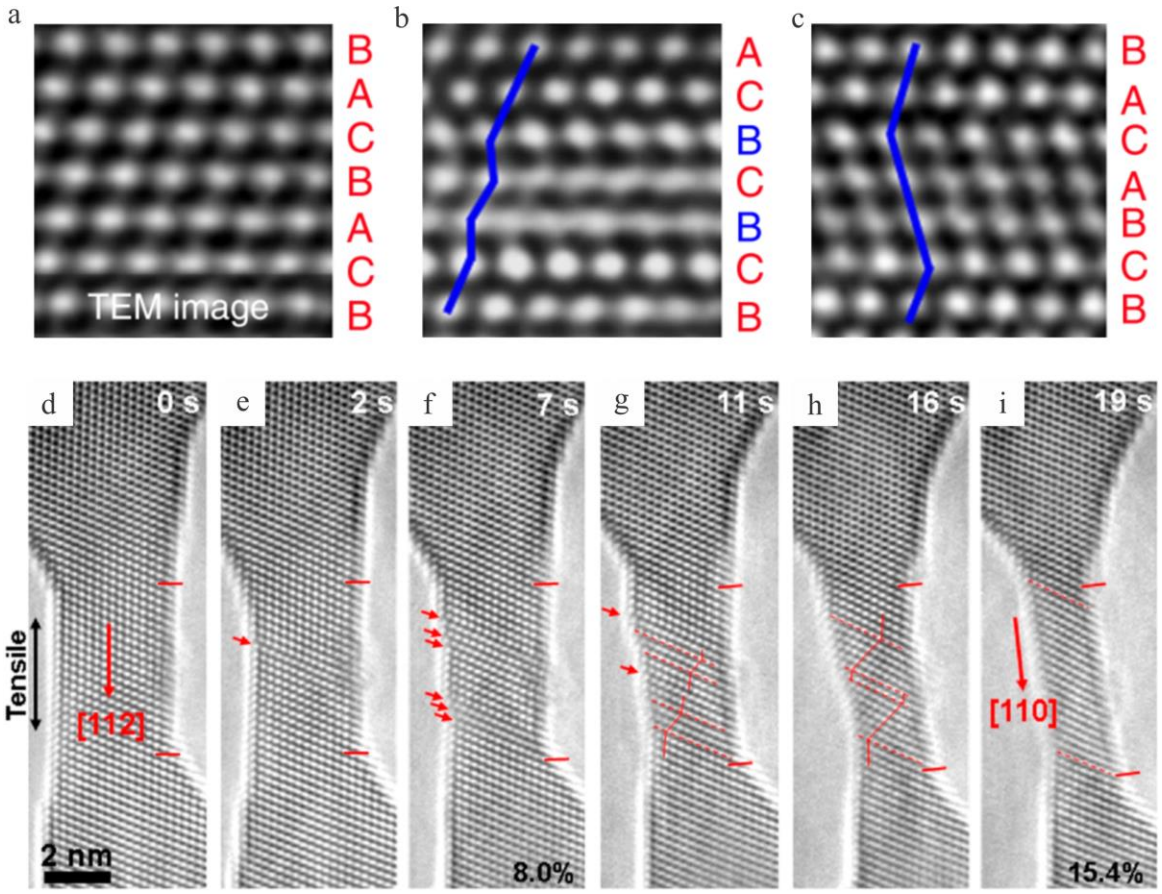

Figure 2.6 Deformation twinning in FCC nanostructured metal materials. (a-c) HRTEM images and associated schematic illustrations showing the dynamical process of the nucleation of a three-layer twin embryo[120]. (d-i) A series of HRTEM images showing the formation of a single deformation twin in the Ag nanowire during tensile loading[95]. The stacking faults are indicated by the red arrows. The twin boundaries are marked out by the red dash lines.

energy[52]. As a particular multifold twin, fivefold twin (FFT) emerges when five coherent twin boundaries (CTBs) concurrently converge at their common [110] rotation axis. Since the angles between any {111} planes in FCC metals are 70.53°, the FFT leaves a mismatched angle of 7.35° (360° − 5 × 70.53°), which is accommodated by the elastic strains (lattice distortion) within the constitutive twinning variants[122]. To date, some mechanisms for FFT formation, deduced from the postmortem TEM observations of the twin morphology and MD simulations, have been proposed. For instance, Liao *et al.*[109, 123], An *et al.*[124] and Zhu *et al.*[125] reported that FFT was observed in nanocrystalline FCC metal materials under ball milling and high pressure torsion at ambient temperature, as shown in Figure 2.7. High external stress and variation in stress orientation were the critical prerequisite conditions for FFT formation. During severe plastic deformation, partial dislocations successively emitted from GBs and TBs and then propagated on the slip planes of different twinning systems, causing sequential twinning dislocation slip in varying slip systems and thus the formation of FFT in nanocrystalline metal materials. Via MD simulations, Cao *el al.*[126] and Shao *et al.*[127] revealed that the complex stress state within a grain of the nanocrystalline metals facilitated the operation of different twinning systems under uniaxial loading. Besides, Zhang *et al.*[128] revealed that the high stress concentration at the incoherent twin boundaries (ITBs) activated successive emission of partial dislocations, resulting in FFT formation in a FCC single-crystalline alloy under indentation. In addition to the mechanical deformation, recrystallization of the nanocrystalline metal materials during annealing treatment could also result in the formation of FFT. Huang *et al.*[129], Cao *et al.*[130] and Bringa *et al.*[131] demonstrated that fivefold annealing twin were formed in nanocrystalline metals under zero external stress at high temperature, where GB decomposition during GB migration[129, 132], grain rotation via dislocation absorption and motion[130], SF overlapping[130] and successive partial emission at TBs or GBs[131] were the dominant

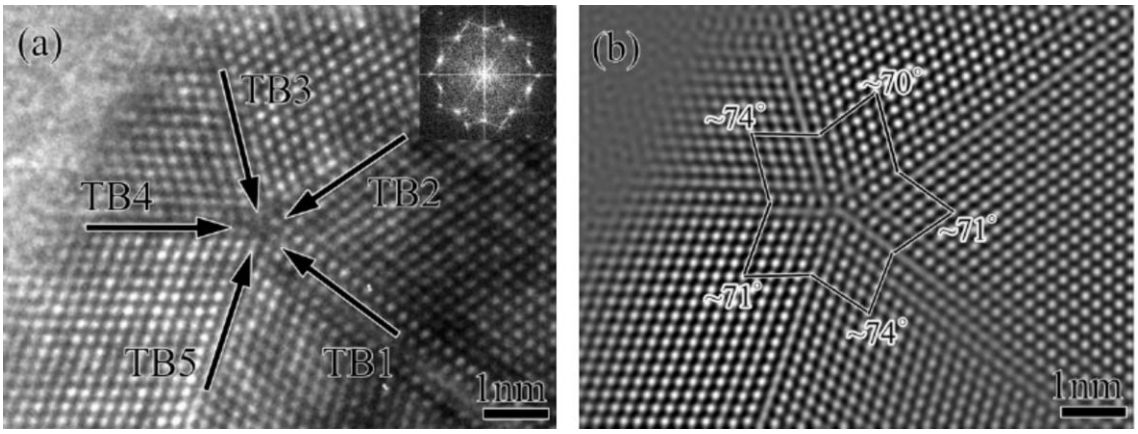

Figure 2.7 The formation of fivefold twin in a ultrafine-grained Cu alloy under high-pressure torsion[124] . (a) HRTEM image showing a fivefold twin. The inset is the corresponding fast Fourier transform image. (b) The inverse fast Fourier transform image of (a).

mechanisms. Furthermore, the high internal stress within the nanograins, such as the high stress concentration at the twin tip[129] and GB curvature-induced local stress[131], could facilitate FFT formation during annealing.

From the above summarizations, it can be seen that deformation twinning in various metal materials has been well understood. As a special twin morphology, FFT has been attracting considerable research attention recently. The previous experimental studies on FFT, however, fell short in obtaining timely and atomic-resolved observation. The formation mechanisms of FFT deduced by postmortem TEM observation remain questionable. In addition, limited by the inherent high strain rate (usually 10^7 /s–10^9/s)[133, 134] and uncertainties in the interatomic potentials[57, 59, 79], the formation mechanisms of FFT revealed by MD simulations need to be further validated by powerful experimental tests, which are capable of achieving *in situ* atomic-scale observation of the dynamic process of FFT formation.

2.2.2 Deformation Twinning In BCC Metals

In contrast to deformation twinning in FCC metals, only screw dislocation-mediated plasticity is mostly reported to be the dominant deformation mechanism in bulk and small-scale BCC metals at room temperature[135, 136, 137, 138, 139, 140, 141, 142]. By performing *in situ* HRTEM testing, Wang *et al*.[143] revealed that deformation twinning was the dominant mechanism in tungsten (W) nanowires at room temperature under the strain rate of 10^{-3} s^{-1} (Figure 2.8). Under compression, a twin embryo nucleated from the intersection between the GB and surface (Figure 2.8a-b) and then propagated laterally into the nanowire (Figure 2.8b-e). The deformation twin thickened through the sequential nucleation and propagation of twinning partial dislocations on consecutive twinning planes. Furthermore, it was found that the nucleated twin embryo in W nanowire had a minimum size of six atomic layers and deformation twin grew in the increments of three atomic layers[144]. The twinning-mediated plasticity was also observed in niobium (Nb) nanowires during tensile

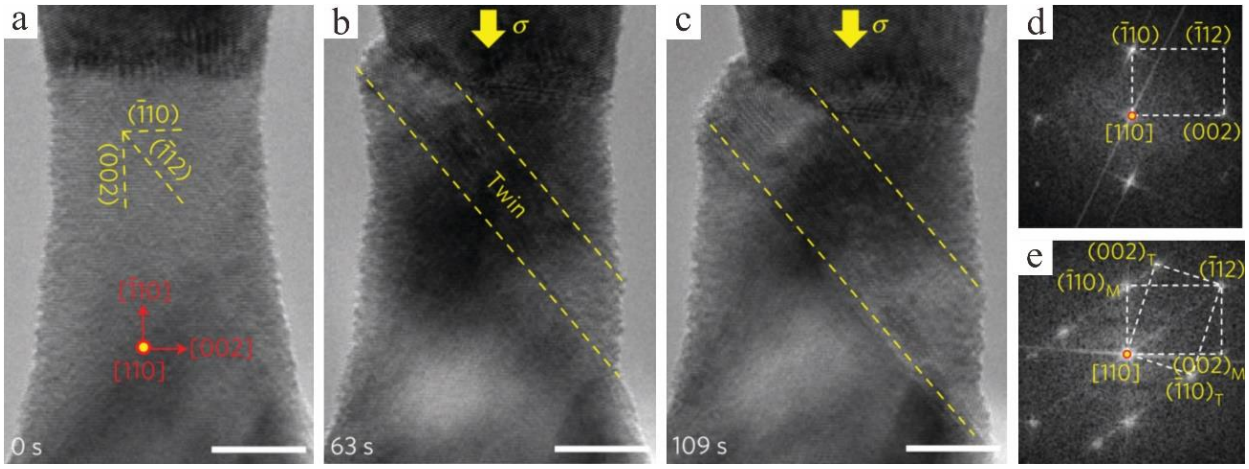

Figure 2.8 Twinning-mediated plasticity in BCC W nanowires[143]. (a-c) Sequential HRTEM images showing the twinning process. All the scale bars are 5 nm. (d-e) Fast-Fourier transformed (FFT) patterns of the original W nanowire (d) and the deformation twinning (e), respectively.

test[145]. Very recently, Wang *et al.*[146] discovered that W nanowire deformed by twinning under tensile loading along a <110> anti-twinning loading direction, which was deemed impossible in the previous studies.

Up to now, BCC nanocrystals usually surprise us with their unexpected mechanical behaviors. The study of deformation twinning in nanoscale BCC metals and the underlying mechanism at the atomic scale is still in their infancy, due to the technical difficulty in fabricating and testing the BCC nanocrystals. Given that BCC nanocrystals hold promising potential for application in small-sized device under extreme operating condition, deep insights into the deformation twinning in BCC nanocrystals is important both scientifically, for the comprehensive understanding of deformation twin in crystalline solids, and technologically, for its practical application.

2.2.3 The Competition Between Deformation Twinning And Perfect Dislocation Slip

The two major displacive mechanisms in metal materials are deformation twinning and perfect dislocation slip, which directly compete with each other through dislocation processes operating on the same set of slip systems[48]. The dominant deformation mode in FCC metals under a specific loading orientation can be well predicted by Schmid's laws via calculating and comparing the Schmid factors for leading and trailing partial dislocations[147, 148], given that the first steps for both twinning and slip are the emission of a leading partial dislocation. If the Schmid factor for leading partial is higher than that for trailing partial, the metal will be deformed by twinning. Not only the loading orientation but also the characteristic length scale of metal materials (e.g. gain size, film thickness and sample dimension) influence the deformation behaviors. Yue *et al.*[149] reported the dominant plastic deformation mechanism changed from perfect dislocation slip

to deformation twinning with decreasing the sample size of Cu nanowires, analogous to the size effect observed in Au thin films[150], nanowires[151] and nanowhiskers[117]. The size-dependent competition between the two plasticity mechanisms is attributed to the difference in the nucleation stresses for perfect and partial dislocation, that increase differently with decreasing microstructural feature size[117, 151]. Moreover, the critical size for the transition from slip to twinning is inversely proportional to the stable stacking fault energy of a metal material. In addition, Yin *et al.*[152] recently reported that the cross-sectional shape of Ag nanowire was an additional factor affecting the competition between twinning and dislocation slip via influencing the energy barrier for twinning, which was proportional to the energy change of side surfaces associated with twinning.

In contrast to FCC metals, there is a lack of general established criteria for determining the dominant deformation mode in BCC metals, due to the fact that the plastic deformation of BCC metals is governed by screw dislocations[138, 153, 154, 155, 156, 157]. The analysis of the resolved shear stresses on twinning and slip systems, however, still plays a key part in determining the dominant deformation mechanism, as demonstrated by Wang *et al.*[143] and Wei *et al.*[158] in W nanowires. However, Wang *et al.*[146] recently discovered that W nanowire deformed by twinning when stretched along a <110>-anti-twinning direction (Figure 2.9), which was different from the previous experimental and computational studies that perfect dislocation slip was the dominant deformation mode in BCC metals under <110> tensile loading[159]. Moreover, some MD simulations on the tensile deformation behaviors of W nanowires along different orientations revealed that twinning tendency increased with experimental temperature[160]. In addition, via MD simulations, Li *et al.*[161] found that deformation twinning was dominant in a W nanowire at high temperature of 1500 K. To date, the influence of loading orientation and experimental temperature on the tensile deformation behaviors of BCC nanocrystals remains experimentally unexplored, due

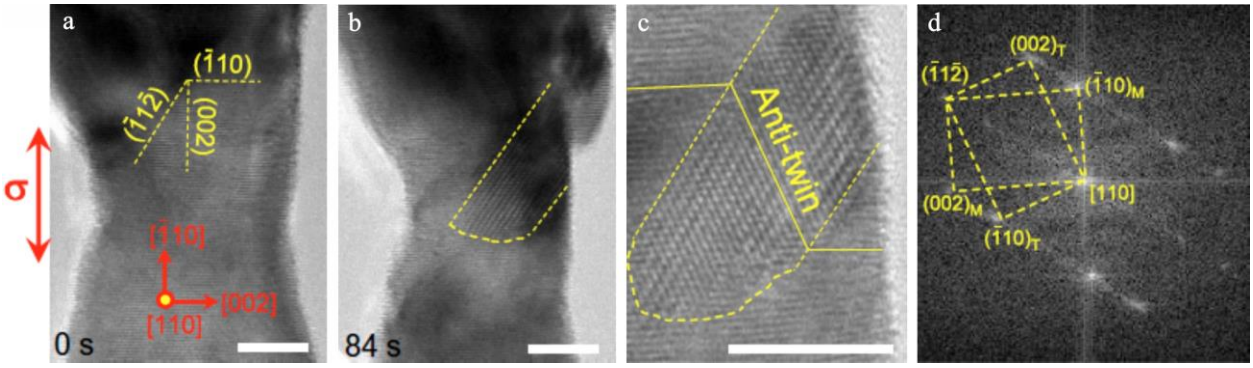

Figure 2.9 Deformation twinning in W nanowire under tensile loading along <110>-direction at room temperature and a strain strate of 10^{-3} s^{-1} [146]. (a) TEM image of a pristine W nanowire with a sample diameter of 16 nm. (b) Formation of anti-twinning in the deformed W nanowire. All the scale bars are 5 nm. (c-d) Magnified HRTEM image (c) and fast Fourier transform image (d) of the anti-twin.

to the technical challenges in conducting tensile test for brittle nanocrystals. The research findings from computational investigations need to be further validated by powerful experimental testing at quasistatic strain rates (10^{-3} s^{-1}).

In the past decades, considerable efforts have been made to investigate the mechanisms of deformation twinning in small-sized FCC metal materials. However, there lies a great ambiguity over the formation mechanisms of FFT in nanostructured metal materials, especially at the atomic scale, due to the fact that the previous studies relied on MD simulations[122, 126, 132, 162, 163] and the postmortem inspection of the twin structure[125, 164]. Considering that introducing FFT into nanostructured metals greatly improves their mechanical properties[165, 166, 167], deep insights into the atomic-scale mechanisms of FFT formation is of vital importance for providing new clues to design high-performance metal materials. Furthermore, although some experimental and computational studies have been conducted to investigate the factors influencing the competition between deformation twinning and perfect dislocation slip in small-sized BCC metals. The effects

of experimental temperature and loading orientation on determining the dominant plastic deformation mechanisms in BCC nanocrystals remain largely unclear.

2.3 TEM-Based In Situ Nanomechanical Testing Method

Due to the increasing technological prominence of metallic nanocrystals[168], their mechanical properties and deformation behaviors have acquired considerable attentions over the past few decades. Benefited from recent advances in experimental technology, some *in situ* testing methods have been proposed via combining nanomechanical testing systems with various characterization platforms, including atomic force microscopy (AFM)[169, 170], scanning electron microscopy (SEM)[171, 172, 173, 174], TEM[175, 176, 177] and X-ray diffraction[178]. Among these advanced experimental techniques, TEM-based *in situ* nanomechanical testing method provides a unique opportunity for directly visualizing the dynamical deformation behaviors of metallic nanocrystals at the atomic scale. Here, some common methods for sample preparation and nanomechanical testing are overviewed.

2.3.1 Sample Preparation Methods For Small-Sized Metal Materials

Small-sized metal materials can either be fabricated from their bulk counterparts (top-down method) or grown to a size (bottom-up method) that can be handled by holders and micromanipulators[179]. The classical top-down sample with a characteristic size of micron or sub-micron diameter can be prepared using focused ion beam (FIB) cutting. FIB cutting, however, introduces significant surface contamination and a number of extrinsic defects near free surface[40,

[41], which modify the initial microstructural feature[180] and probably influence the intrinsic mechanical response of the sample during mechanical test. Bottom-up methods, including physical vapor deposition (PVD)[152, 174] and electrodeposition[179], are usually employed to fabricate samples with characteristic size ranging from microns to nanometers (e.g. metallic nanowhiskers and nanowires). However, systematic defects and impurities may be introduced into the nanoscale metals during the process of crystal growth [181].

2.3.2 TEM-Based In Situ Mechanical Testing Method

The major difficulty in performing TEM-based *in situ* nanomechanical testing is the miniaturization of experimental setups, since the TEM pole-piece gap is quite small (~3 mm)[181, 182]. To meet this extreme operating condition, some effective *in situ* experimental methods have been proposed via incorporating nanoindentation, MEMS (micro-electromechanical system)-based device and AFM into a TEM platform. Nanoindenter-based TEM holders could measure the force (in the order of μN) and displacement of a flat punch tip forced into the nanopillars (Figure 2.5a)[183, 184, 185]. The contact of the tip with the pillar, however, generates strain gradient and disrupts imaging condition during mechanical loading. MEMS-based nanomechanical testing method is developed to investigate the mechanical behaviors of nano-sized metals under a wide range of strain rates from 10^{-5} to 10^{2} s^{-1} [16, 31, 186, 187], as shown in Figure 2.5b. This testing method is able to measure the load with nano-Newton resolution and displacement with nanometer resolution[182]. Most of these MEMS-based testing platforms, however, highly rely on quite complicated experimental setups making their implementations and operations both challenging and time-consuming[172]. Besides, a AFM-TEM sample holder is developed for evaluating the mechanical properties of nanoscale metals (Figure 2.5c)[188]. Clamping of the sample is carried out by pushing

the coated nanowire on a STM probe against the AFM tip surface until strong bonding between the nanowire and AFM tip is formed. The applied force during testing can be calculated via recording the deflection of the AFM cantilever with known spring constant. This testing method, however, fails to capture the HRTEM images of metallic nanocrystals, due to the unsatisfactory sample quality. Han *et al.*[189] design a thermally actuated TEM tensile device (Figure 2.10d), which is capable of investigating the mechanical behaviors of nanostructured metals[175, 190, 191, 192]. The tensile device, loaded onto a TEM heating stage, consists of two bimetallic strips, which are fixed, in opposing positions, on a TEM Cu-ring grid. Due to the difference in thermal expansion coefficients of the two materials in bimetallic strips, the strips are bent in opposite directions to

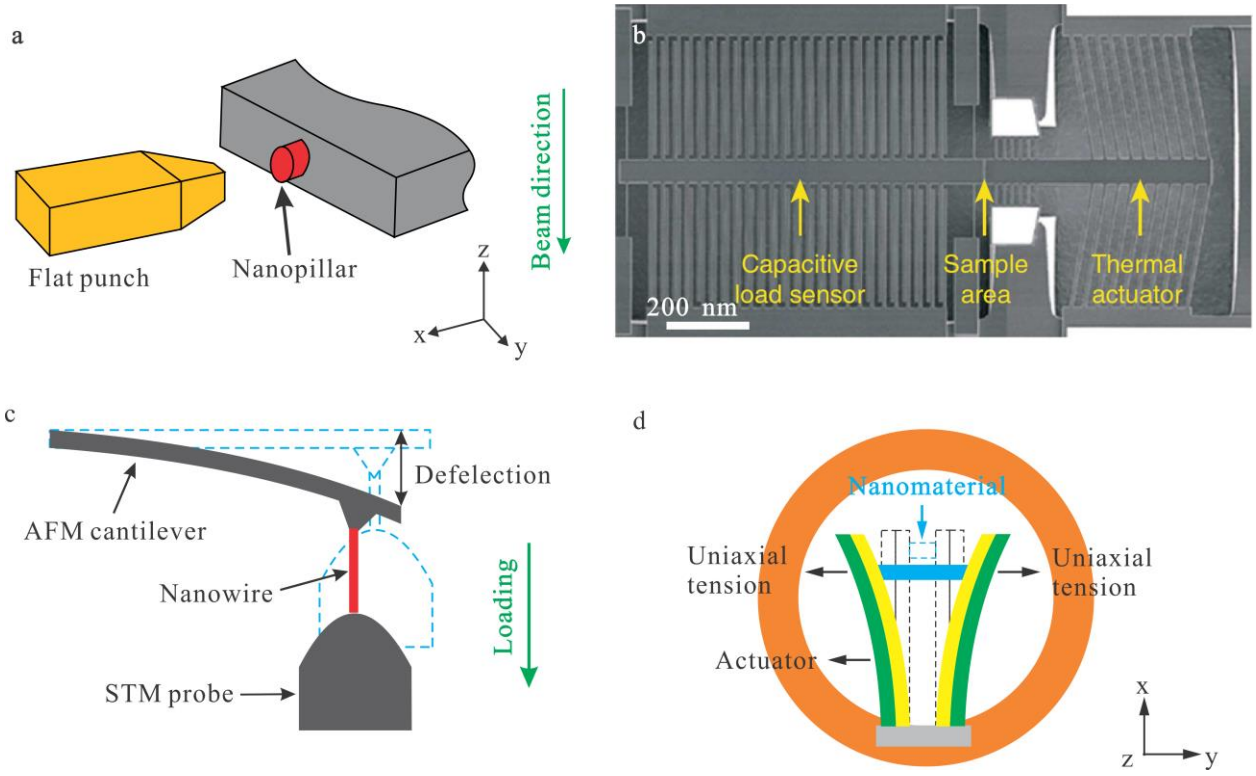

Figure 2.10 TEM-based *in situ* nanomechanical testing methods. (a) Schematic of nanoindenter-based nanomechanical testing. (b) The MEMS stage used for *in situ* TEM nanomechanical testing[193]. (c) Schematic of the AFM-STM mechanical testing platform. (d) Schematic of the thermally actuated TEM tensile device.

provide the tensile pulling force for the samples under heating conditions. However, it is time-consuming to obtain high-quality HRTEM imaging due to the low-quality samples prepared by FIB cutting. Moreover, it is hard to precisely control the strain and strain rate applied on the samples.

From the above summarizations, it can be seen that the current *in situ* TEM testing methods are usually time-consuming and hard to obtain high quality HRTEM images of the deformed nanostructured metals. Moreover, *in situ* atomic-scale nanomechanical testing methods for nanoscale metals at elevated temperature are still lacking, and thus are in urgent need, considering that the actual service conditions for the metallic nanocrystals in electronics are complexed. Newly developed atomic-scale *in situ* experimental mechanics at elevated temperature can open new horizons for achieving a fundamental understanding on the temperature-dependent mechanical behaviors of metallic nanocrystals.

2.4 Motivation And Research Objectives

A comprehensive understanding of the atomic-scale mechanical behaviors of metallic nanocrystals is both scientific and practical significance. Based on the background review in this chapter, substantial research efforts have been devoted to investigating the deformation behaviors of small-sized metal materials. Limited by the current experimental testing techniques, several critical issues concerning the mechanical behaviors of nanoscale metals remain unexplored. Firstly, atomic-scale understanding of the compressive deformation behaviors of nanoscale metals is lacking, especially when diffusional plasticity occurs. Secondly, lack of timely and atomic-resolved observation of the dynamic process of fivefold twin formation in nanoscale metals falls

short in understanding the fundamental physical mechanisms for fivefold twin formation. Thirdly, advanced testing techniques are still lacking to investigate the mechanical behaviors of metallic nanocrystals at elevated temperature. In lieu of the critical issues summarized above and their significances, the time- and temperature-dependent mechanical behaviors of metallic nanocrystals, as well as the formation mechanism for fivefold twin in nanoscale metals, will be investigated using TEM-based *in situ* nanomechanical testing technique. Accordingly, the research objectives in this dissertation are summarized as follows:

1. What are the differences in the compressive deformation behaviors of the metallic nanocrystals with and without surface diffusional events? Are the diffusional events at the free surface of metallic nanocrystals associated with the type of material, the applied strain rate and the sample size? What are the compressive failure behaviors of the metallic nanocrystals with surface atomic diffusion? Do the displacive and diffusive deformation couple with each other during the compressive loading of metallic nanocrystals as that in the tensile test of Ag nanocrystals?

2. What are the atomic-scale formation mechanisms of fivefold twin in nanoscale Au under mechanical loading? Is it possible that fivefold twin can form in a single crystalline Au nanocrystal under mechanical loading? What are the differences in the formation mechanisms for fivefold twin in Au nanocrystals under different loading modes? Is the formation process of fivefold twin reversible under mechanical loading?

3. New experimental testing technique is required to be developed to achieve *in situ* atomic-scale observation of the mechanical behaviors of metallic nanocrystals at elevated temperature. Compare the differences in the mechanical behaviors of nanoscale metals at room and elevated temperatures.

Experimental observations on the mechanical behaviors of metallic nanocrystals will provide deep insights into the atomistic nature of mechanical degradation in metal materials, which is of technological importance for designing mechanically stable and reliable metal materials in a practical application.

3.0 Materials and Experimental Procedures

In this chapter, the materials and experimental approaches in this dissertation will be described. Defect-free single-crystalline silver and platinum nanocrystals are selected to investigate the compressive deformation behaviors mediated by coupled displacive-diffusive mechanisms; gold nanocrystals with different microstructural features, such as single-crystalline gold nanocrystal, gold nanocrystal with a Σ9 grain boundary and gold nanocrystals with multifold twins (two-, three-, four- and five- fold twins), are chosen to reveal the atomic-scale mechanisms of fivefold twin formation; Single-crystalline tungsten nanocrystals are selected as the model system to investigate the atomic-scale mechanical behaviors of metallic nanocrystals at elevated temperature. The testing method integrating the fabrication of metallic nanocrystals, *in situ* nanomechanical testing and TEM observation will be presented.

3.1 Materials

3.1.1 Single-Crystalline Ag and Pt Nanocrystals

Compared to Pt, Ag has a lower activation energy barrier for surface atom diffusion and a much higher surface atomic diffusivity[57, 194, 195]. Due to the large difference in material properties, Ag and Pt were selected as the model system to investigate the compressive deformation behaviors of metallic nanocrystals, mediated by coupled displacive-diffusive and pure displacive mechanisms, respectively. The commercial polycrystalline Ag and Pt rods with the diameter of

0.01 inches and a high purity of 99.999% were obtained from ESPI Metals Inc. The impurity concentrations in Ag and Pt rods are listed in Table 3.1 and 3.2, respectively. Before all the *in situ* compression tests, the metallic nano-tips were generated at the fracture surface of the bulk metal rods using a wire cutter (Figure 3.1). This approach produced metallic nano-tips with clean surfaces, which were ideal for studying surface diffusive plasticity in metallic nanocrystals. In addition, plasma cleaning was conducted on the metallic nanotips to reduce the potential effects of carbon deposition and oxidation on the deformation behaviors of metallic nanocrystals. The Ag and Pt nanocrystals for the *in situ* compression tests were prepared directly inside a TEM using *in situ* nanowelding developed by Wang *et al*.[143] and Zhong *et al*.[37]. The fabrication process for the metallic nanocrystals were conducted inside a FEI Titan TEM equipped with a Nanofactory scanning tunneling microscope (STM) holder. The fractured metal rod with numerous nanotips and a W nanoprobe etched with NaOH solution were mounted on the static and piezo-controller sides of the STM holder, respectively, as shown in Figure 3.2. When the W nanoprobe moved forward and then contacted with the selected nano-tips oriented in the <110> zone axis, the pre-applied voltage of ~1 V could melt the nanotip and the probe, generating bridge-shaped metallic nanocrystals with controllable dimensions and clean surface, which were epitaxially grown from the substrate at the static side and connected to the W nanoprobe (Figure 3.3). The middle segment of the nanocrystal with a smaller diameter served as the gauge section, which concentrated all the plastic deformation during mechanical tests.

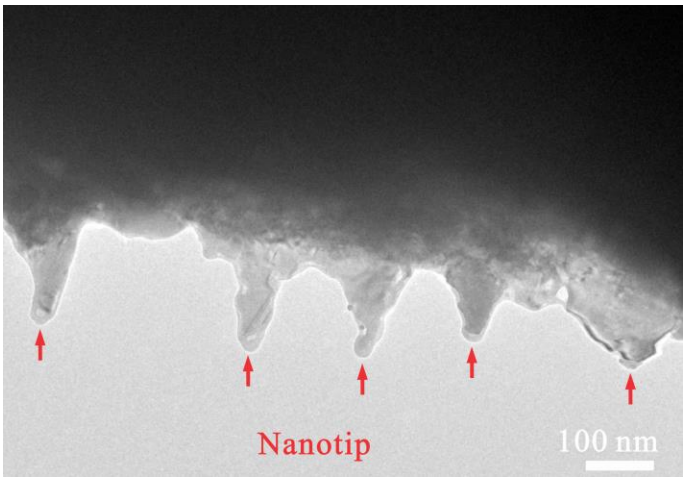

Figure 3.1 Numerous Ag nano-tips at the fracture surface of the bulk polycrystalline Ag rod.

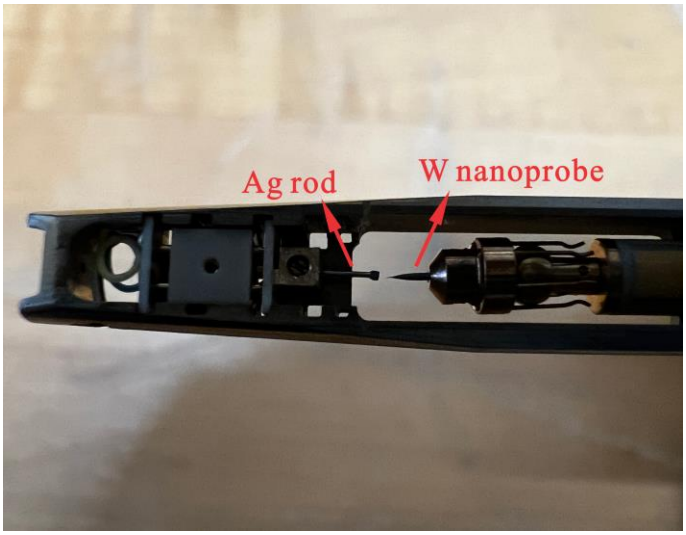

Figure 3.2 A scanning tunneling microscope (STM) holder with the fractured metallic rods and the W nanoprobe loaded onto the static and piezo-controller sides, respectively.

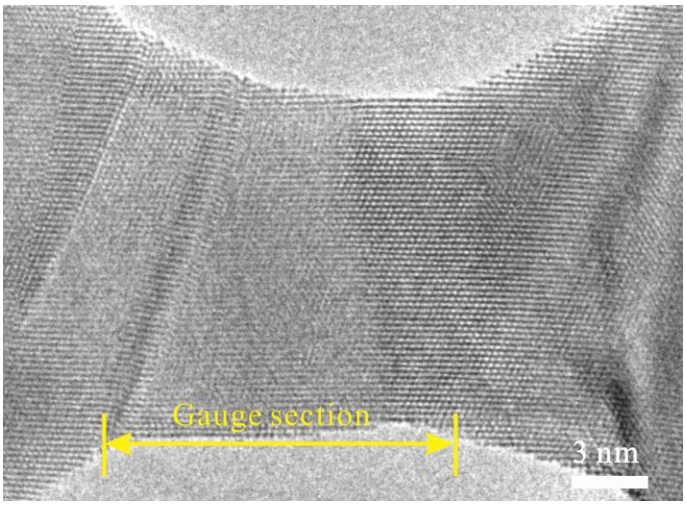

Figure 3.3 An example of the as-fabricated Ag nanocrystal viewed along the <110> zone axis.

Table 3.1 Impurities in Pt rod

Element	Concentration, ppm
Na	<1
Fe	<1
Ir	<2
Al	<2
Ca	8
Ag	3

Table 3.2 Impurities in Ag rod

Element	Concentration, ppm
Cu	<0.5
Bi	<0.5
Pb	<0.5
Ni	<0.5
Fe	<0.5
Pd	<0.5
Te	<0.5

3.1.2 Au Nanocrystals

Compared to Ag, Au is hard to oxidize in air, excluding the possibilities of modifying surface condition and introducing extrinsic surface defects. Au is suitable to study the atomic-scale mechanisms for fivefold twin formation under mechanical loading. The commercial polycrystalline Au rod with the diameter of 0.01 inches and a high purity of 99.999% was obtained from ESPI Metals Inc. The impurity concentrations in the Au rod are listed in Table 3.3. Before the experiments, the bulk Au rod was fractured by a wire cutter to obtain numerous Au nano-tips on the fracture surface. Subsequently, two fractured Au rods were loaded onto the static and the probe sides of the STM holder, respectively. To fabricate a Au nanocrystal, two Au nano-tips oriented in the <110> zone axis were selected to be welded together via applying a voltage of ~ 1V on the two sides of the STM holder. During the process of *in situ* nanowelding, some defects, such as stacking faults[50, 196], twins[51, 197, 198], full dislocations[199], grain boundary[200, 201, 202, 203] and amorphous phase[204], may be introduced in the nanoscale Au. Via carefully controlling the welding process, single-crystalline Au nanocrystal and Au nanocrystal with different microstructural features can be fabricated.

Table 3.3 Impurities in Au rod

Element	Concentration, ppm
Fe	<1
Ca	<1
Ag	5

3.1.3 Single-Crystalline W Nanocrystals

The polycrystalline W rods with the diameter of 0.013 inches and a high purity of 99.98% were obtained from ESPI Metals Inc. The impurity concentrations in the W rod are listed in Table 3.4. To remove organic contamination on the surface, the W rods were soaked in acetone for 24 hours and then dried in air. Before *in situ* mechanical tests, the bulk rod was plasma cleaned and then fractured by a wire cutter to obtain numerous W nano-tips on the fracture surface. Subsequently, the fractured W rod and the W nanoprobe etched with NaOH solution were loaded onto the static and probe sides of the STM holder, respectively. The W nano-tips oriented in the <110> or the <111> axis were selected to be moved forward the nanoprobe via controlling the piezo-controller. When contact was made, the pre-applied voltage of 2–4 V melted the W nano-tip and nanoprobe, and then they were welded together, forming a defect-free single-crystalline W nanocrystal (Figure 3.4).

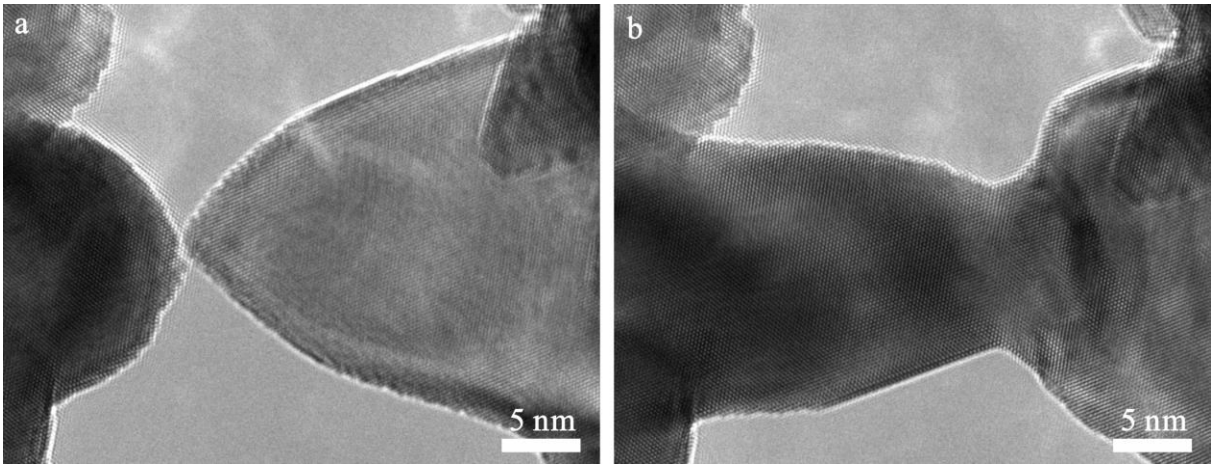

Figure 3.4 The process of *in situ* nanowelding. (a) The W nanoprobe with a pre-applied voltage of 2–4 V was moved to contact with the selected W nano-tip. (b). A W nanocrystal was fabricated when the contact between the W nano-tip and probe was made.

Table 3.4 Impurities in W rod

Element	Concentration, ppm
Cr	<20
Fe	<50
Ni	<50
Cu	<10
K	<30

3.2 Experimental Procedures

3.2.1 In Situ Experimental Setup

All the *in situ* nanomechanical tests in this dissertation were carried out inside a FEI Titan TEM equipped with a Nanofactory scanning tunneling microscope (STM) holder (Figure 3.5). Before sample preparation, the crystallographic orientation of the metallic nanotips on the static side of the STM holder can be tuned within a large range from -15° to +15°. After sample preparation via nanowelding, *in situ* nanomechanical test for metallic nanocrystals can be performed via controlling the movement of the STM probe on the piezo-controller. Tensile and compressive tests can be performed via controlling the backward and forward movements of the W nanoprobe at a constant rate, respectively. Likewise, shear or bending tests can be conducted via controlling the leftward or rightward movements of the STM probe at a constant state. The applied strain rates during mechanical tests were estimated based on the movement speed of the W probe on the piezo-manipulator and the gauge length of the tested nanocrystal. Moreover, all

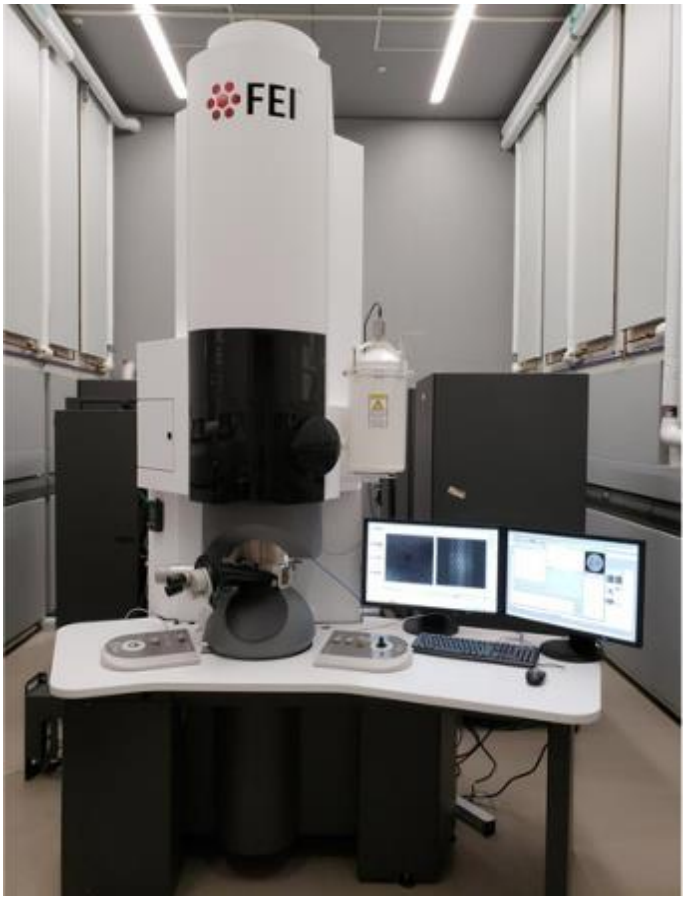

Figure 3.5 FEI Titan 80-300 TEM in Petersen Institute of Nanoscience and Engineering at University of Pittsburgh.

the *in situ* experiments were performed at 200 kV and recorded in real-time by a charge-coupled device (CCD) camera at the rate of 0.25 s/frame.

3.2.2 Identification Of Deformation Mechanisms

During *in situ* TEM nanomechanical tests, the occurrence of displacive and diffusive deformations can be visualized and identified, based on the timely- and atomic-resolved observation of all the atomic columns and the lattice irregularity in metallic nanocrystals during

mechanical loading. As shown in Figure 3.6a, the perfect edge dislocation is marked out by an inverted “T”, and its Burgers vector can be measured based on the Burgers circuit. In addition to the full dislocation, the SF, resulting from the nucleation and propagation of a leading partial dislocation, can be identified based on the lattice pattern. Owing to the formation of a SF, the local stacking sequence inside the FCC nanocrystal changes from the perfect FCC lattice (CABC) to a localized hexagonal close-packed (HCP) structure (CACA), as shown in Figure 3.6b. Figure 3.6c shows an example of a deformation twin in FCC nanocrystals. The crystal lattice on the two sides of the TB has a mirror symmetric relationship. The above discussions demonstrate that the defect type and the associated evolution during the process of displacive deformation in the FCC metallic nanocrystals can be visualized and identified, based on the analysis on HRTEM images. Similar microstructural analysis at the atomic scale can also be applied to BCC nanocrystals when viewed along <100>, <110> and <111> zone axis. Moreover, the occurrence of diffusive deformation in metallic nanocrystals can also be visualized and identified based on the observation of the atomic columns at free surface, as shown in Figure 3.7. After atomic diffusion at the free surface of nanocrystal, the atomic columns, marked out by the yellow circles, diffuse to the end of the nanocrystal during mechanical test[42, 43, 96], resulting in the experimental observation that the atomic-scale step at free surface migrates to the end of the nanocrystal.

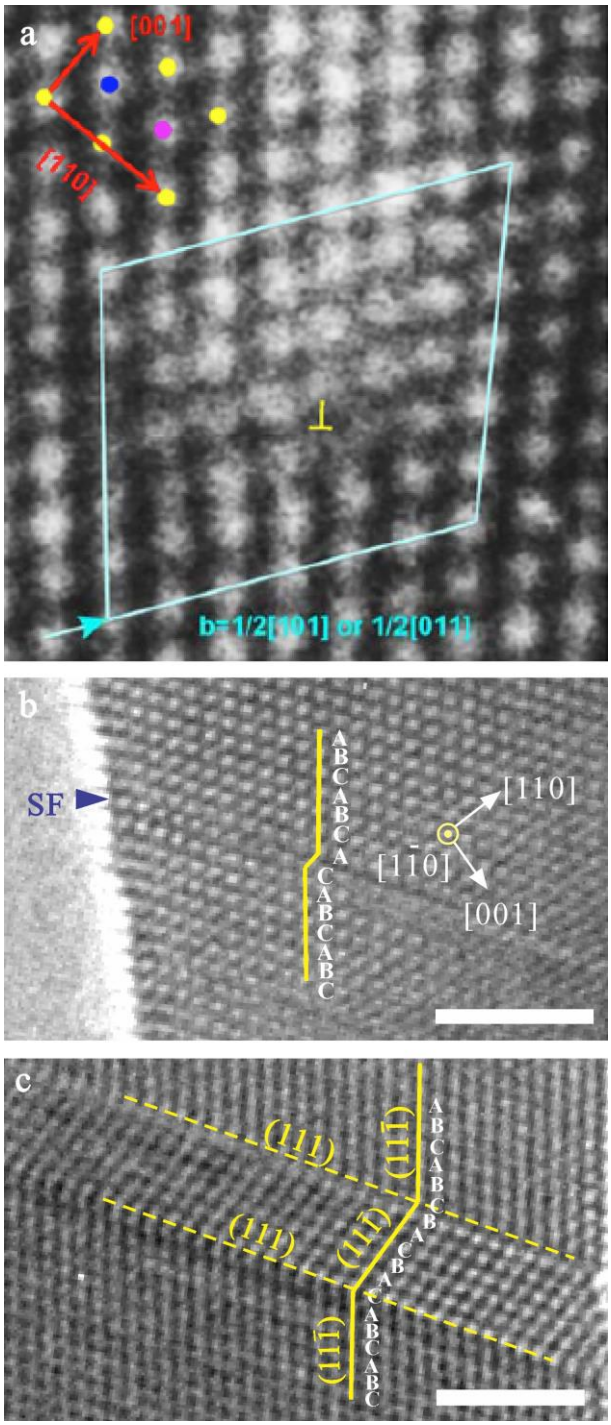

Figure 3.6 HRTEM images show various types of defects in the deformed FCC nanocrystals. (a) Lattice pattern of a perfect edge dislocation[58]. An extra lattice plane is observed in the upper part of the crystal. (b) Formaiton of a stacking fault caused by a partial dislocaiton slip. (c) Formation of a deformation twin caused by a series of partial dislocaiton slip. Scale bars are 2 nm.

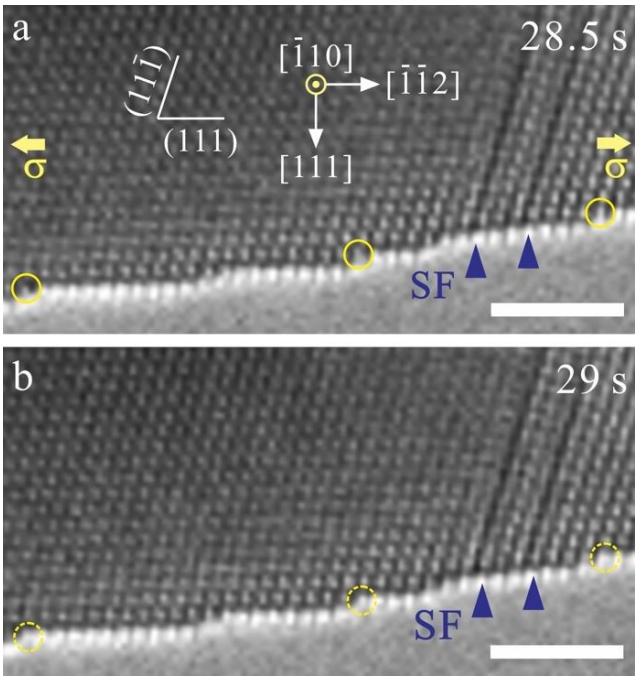

Figure 3.7 *In situ* observation of surface atom diffusion in a Ag nanocrystal . (a-b) Sequential HRTEM images showing the atomic lattice pattern before (a) and after (b) surface atom diffusion. All the scale bars are 2 nm. The yellow circles mark out where surface diffusion occurs.

3.3 Simulation Methods

MD simulations were employed to further understand the atomic-scale mechanisms of fivefold twin formation in Au nanocrystals under mechanical loading. This work was performed by my collaborators, Professor Chuang Deng at University of Manitoba and Professor Christopher R. Weinberger at Colorado State University. All the computational simulations were performed by using Large-scale Atomic/Molecular Massively Parallel Simulator (LAMMPS) package[205] with an embedded-atom method potential for Au[206]. This potential has been well documented to produce consistent simulation results with experimental observations in Au nanowires under various loading conditions[207]. Prior to the mechanical deformation, the energy of the models was

minimized by the conjugate gradient method, and then relaxed at 300 K for 25 ps under a canonical (NVT) ensemble. Atomic structures of the Au nanocrystals during mechanical loading were visualized, using common neighbor analysis (CNA) for the defect structure in OVITO[208]. The atomic stress in the Au nanocrystal can be analyzed by using the Virial theorem as discussed by Cheung and Yip[209].

In total, four types of different models have been constructed for atomistic modeling and simulation by using Atomsk[210]. The first model (Model 1 in Figure 5.4) was a square <112>-oriented Au nanowire with the width and length being ~ 5 nm and 16 nm, respectively. The second model (Model 2 in Figure 5.9) was a square Au nanowire with dimensions being ~11 nm and 20 nm along the width and length, respectively, which contained a triple junction in the middle. The GB between the two grains on the right side was a coherent twin boundary, while the two GBs between the left grain and the two grains on the right were both asymmetric <110>-tilt {001}/{112} GB with the misorientation angle of 35.26°, which were close to the 38.94° for the Σ9 GB. The third model (Model 3 in Figure 5.10) was a bi-crystalline model in Au containing an asymmetric <110>-tilt Σ9 {111}/{115} GB with the dimensions being ~ 30 nm, 2.9 nm, and 10 nm along the x, y, and z directions, respectively. The Model 1 was subject to bending test, which was achieved by rotating a thin slab with thickness ~1nm at both the top (clockwise) and bottom (anti-clockwise) of the nanocrystal around its respective center of mass along the <110> direction (i.e., the y-axis) at a constant speed of 0.05°/ps. For the Models 2 and 3, compression was applied along the x-axis by moving a thin slab with thickness ~1 nm at both the top and bottom at a constant speed of 1 m/s towards each other. Periodic boundary condition was applied along the <110>-tilt direction (i.e., the y-axis) in Model 2 during both the relaxation and mechanical loading, while free

boundary conditions were applied for all other cases. The time step was 5 femto-second and the Nose/Hoover thermostat was used to control the temperature[211, 212].

The fourth model was a bi-twinned Au nanocrystal with axis along a <112> direction constructed by applying the twin symmetry across a {111} plane that lied along the axis of the nanocrystal (Figure 5.11c-f). The diameter of the nanocrystal was around 4 nm, similar in size to those observed in experiments. In order to mitigate surface and or facet effects, the cross-section of the were chosen to be circular. However, both variable diameter and other cross-sections were also tested. For constant cross-section nanocrystal, periodic boundary conditions were applied along the length of the nanocrystal, while the lateral surfaces of the wire were exposed to vacuum. The nanocrystals were then run for 1 million timesteps, with a time step of 1 femto-second, at a temperature of 300K using a Nove'-Hoover thermostat. The stress along the axis of the nanowire was controlled to be zero using a Parinello-Rahman barostat. After equilibration, the nanocrystals were then deformed using a constant strain rate simulation (non-equilibrium molecular dynamics) by integrating the SLLOD equations of motion with the temperature controlled by a Nose-Hoover thermostat.

4.0 Atomistic Processes Of Diffusion-Mediated Unusual Compression Fracture In Metallic Nanocrystals

(*Portions of this chapter have been reproduced with permission from Materials Research Letters, Volume 10, Issue 12, Pages 805-812. Copyright 2022 by Taylor & Francis Group.*)

In this chapter, the atomic-scale compressive deformation behaviors of silver and platinum nanocrystals will be studied. Previous studies indicated that either pure displacive or pure diffusive mechanisms resulted in the thickening behavior of nanoscale metals during compression. However, it is not fully understood how a coupled displacive-diffusive mechanism would mediate the compressive deformation of metallic nanocrystals, especially at the atomic scale. Here, by conducting transmission electron microcopy-based *in situ* atomic-scale compression tests, it is found that, instead of local thickening commonly reported thus far, abnormal thinning events consecutively occur in silver nanocrystals, where preexisting dislocations and crystal slip serve as stimuli to activate surface atom diffusion. As the width of silver nanocrystal reduces to a critical size, tensile-fracture-like failure occurs, caused by surface atom diffusion. Different from the silver nanocrystals, pure displacive mechanism is dominant in platinum nanocrystals, resulting in continuous thickening during compression. These findings not only advance the current understanding of compressive deformation behaviors in metallic nanowires, but also shed light on atomic-scale coupled diffusive–displacive deformation mechanisms, providing new clues to design mechanically reliable nanoscale metals for electrical devices.

4.1 Introduction

Nanoscale metals with superior electrical and mechanical properties are promising building blocks for a spectrum of applications, such as nanoelectromechanical systems (NEMS)[213], wearable devices[214, 215] and stretchable and flexible electronics[11, 19, 20]. In a practical application of the nanoscale-metal-based devices, mechanical degradation and failure frequently occur in the nanoscale metals, deteriorating their electrical performances[53, 97, 216]. Profound insights into the atomic-scale deformation mechanisms in nanoscale metals are of upmost importance for understanding their deformation behaviors and realizing their desired mechanical properties to guarantee the mechanical reliability and operation stability of microelectronic assemblies in industrial settings[35, 217].

The minuscule volume and substantial surface-to-volume ratio render the nanoscale metals with unusual mechanical behaviors different from their bulk counterparts[40, 48, 53, 61, 218], which has attracted enormous research interests in the field of materials science. As the characteristic size decreases to a few nanometers, diffusional deformation is expected to be activated at room temperature, and it even dominates over displacive deformation as the only carrier of plasticity in nanoscale metals[55, 65, 80, 81]. Moreover, compared to grain boundaries (GBs) in bulk nanocrystalline (NC) metal materials, the free surface in nanoscale metals, having higher free volume, could serve as a highway for mass transport[54, 217, 219]. Recent experiments on sub-10 nm Ag nanoparticles[88] found that deformation was mediated by surface atomic diffusion without observable displacive plasticity, resulting in liquid-like pseudoelastic behavior during cyclic loading. Furthermore, some *in situ* TEM tensile tests of Cu, Ag and Au nanowires also demonstrated that atom diffusion at free surface mediated crystalline-liquid-drop-like retraction behaviors in the fractured nanowires[35, 37, 88, 89, 90, 91]. Not only competition but also cooperation between surface diffusional creep and crystal

slip exist in the Ag nanocrystals under tensile loading[37, 95]. Given that the previous studies focused on investigating the influence of surface diffusion on dislocation activities in metallic nanocrystals during tensile deformation, it naturally raises the question of how the interplay between diffusive and displacive mechanisms mediates the compressive deformation of nanoscale metals. Furthermore, local thickening, resulting from dislocation-slip-mediated slip band[40, 140, 143] or interface diffusion[39], has been frequently observed in various nanostructured metals during compression. Compressive deformation behavior in nanoscale metals, mediated by coupled displacive-diffusive mechanisms, remains unexplored, especially at the atomic scale[97].

Here Ag and Pt nanocrystals are adopted as the model system to investigate the compressive deformation behaviors of FCC metallic nanocrystals. By performing *in situ* TEM-based compression tests, consecutive thinning events occurring in the Ag nanocrystals are observed, which are attributed to surface atom diffusion activated by preexisting dislocations and crystal slip. When the size of the Ag nanocrystal reduces to a critical value, tensile-fracture-like failure occurs. The consecutively thinning and the ultimate compression fracture in the Ag nanocrystal upon compression have yet to be reported in the previous studies on metallic nanocrystals. By contrast, pure displacive-mechanism-dominated plasticity is observed in Pt nanocrystal during compression, leading to the thickening behaviors.

4.2 Experimental Procedures

The detailed experimental procedures are described in Chapter 3.1.1. *In situ* compression tests at room temperature were conducted inside a FEI Titan TEM equipped with a Nanofactory STM holder. The strain rates of 10^{-3} s^{-1} and 0.06 s^{-1} during compression were controlled by the

movement speed of the W nanoprobe on the piezo-controller side. Moreover, all the tests were operated at 200 kV with low dose conditions (electron beam intensity < $10^5 A \cdot m^{-2}$) in a short time (less than 3 min) to minimize the potential beam effects on deformation behaviors[220, 221]. The temperature rise induced by electron beam illumination[222] in Ag nanocrystals was negligible in this study (less than 1 K[95, 220]), as well as the knock-on effect[95]. Since the activation energy for surface diffusion is much lower than the sublimation energy of Ag[194, 223, 224, 225], the rate of curvature- and stress-driven surface diffusion is much higher than the mass loss rate induced by electron beam. In addition, surface diffusion (self-healing) could fill up the vacancies induced by knock-out effect[90, 226]. In this study, though surface diffusion can be influenced by electron beam, the electron-induced sputtering was not a primary factor affecting the diffusional behaviors of Ag nanocrystals.

4.3 Experimental Results

4.3.1 Preexisting-Dislocation-Facilitated Thinning In Ag Nanocrystal

Atomic-scale thinning events in the Ag nanocrystal with preexisting dislocations are captured by *in situ* HRTEM compression test (Figure 4.1). As shown in Figure 4.1a, a 4.3-nm-diameter Ag nanocrystal is compressed at room temperature under a strain rate of 10^{-3} s^{-1}. The viewing direction of the Ag nanocrystal is along $[\bar{1}10]$ zone axis, and the loading direction is along $[\bar{1}\bar{1}2]$, as labeled by a double-headed black arrow "σ". Two dislocations exist in the as-fabricated Ag nanocrystal before the compression test, as shown in Figure 4.1a. Dislocation, a line defect in a crystal lattice, causes an abrupt change in the arrangement of atoms and introduces elastic lattice

strain near the dislocation core[66, 227]. The elastic strain field of the preexisting dislocation close to the nanocrystal surface turns the flat surface into the irregular one (Figure 4.1a), altering the coordinated environment of the local surface atoms. Compared to the atoms at other surface sites, the atoms at the irregular surface sustain a higher chemical potential, arising from the coordinated environment change and the dislocation strain field, which favors diffusional mass transport at free surface[39]. With the increase of compressive strain, two surface steps with a height of one atomic layer, marked as "step 1" and "step 2", are observed to form at the surface of the Ag nanocrystal after the diffusion of individual atoms at the irregular surface, as shown in Figure 4.1b. With further loading, the surface steps "step 1" and "step 2" continuously migrate to the nanocrystal end

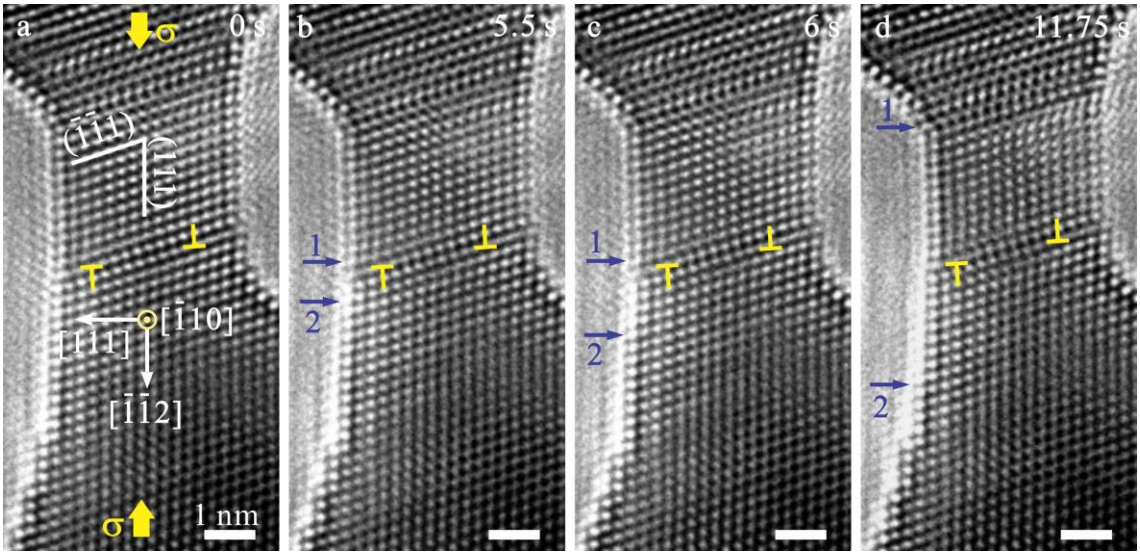

Figure 4.1 Sequential TEM images showing surface atom diffusion during the compression test of a Ag nanocrystal with preexisting dislocations. (a) TEM image of a 4.3-nm-diameter Ag nanocrystal with preexisting dislocations (marked by "T") as viewed along [$\bar{1}$10]-direction and loaded along [$\bar{1}\bar{1}$2]-direction at room temperature under a strain rate of 10^{-3} s^{-1}. (b) Formation of two surface steps (step 1 and step 2) on the {111} surface of the Ag nanocrystal in the vicinity of the preexisting dislocations. (c-d) Sequential TEM images showing the continuous movement of the surface steps towards the end of the nanocrystal. The movements of the surface steps are tracked by the arrows. All the scale bars are 1 nm.

with no displacive plasticity detected, causing that the nanocrystal width decreases by one atomic layer (Figure 4.1c-d).

4.3.2 Slip-Activated Surface Atom Diffusion In Ag Nanocrystal

In addition to the preexisting dislocations, crystal slip could also serve as a stimulus to activate surface atom diffusion, resulting in thinning in Ag nanocrystal upon compressive loading (Figure 4.2a-e). As show in Figure 4.2a-b, under <112>-compression, a 30° partial dislocation with the Burgers vector of $1/6[2\bar{1}1]$ or $1/6[\bar{1}21]$ nucleates from the free surface, and then glides through the nanocrystal, leaving behind a stacking fault (SF) and a surface step with a height of one-third of one atomic layer at the SF site (Figure 4.2b and 4.2j). Furthermore, the partial dislocation slip also leads to local lattice reorientation, which changes the surface sidewall from {111} to {100} planes, increasing the surface energy at the SF site[228]. Accordingly, the coordination number of the surface atoms decreases from 9 at {111} flat surface plane to 8 at the surface step with a height of one-third of one atomic layer on {100} plane. Compared to the other surface atoms, the atoms at the surface step with a height of one-third of one atomic layer are of a lower coordination number and suffer from a higher chemical potential arising from curvature, applied stress, surface energy change and SF energy (see Section 4.4.1). The chemical potential gradient along the Ag nanocrystal favors surface atom diffusion from the SF site towards the end of the nanocrystal[95]. After the diffusional events at the SF site, two steps with a height of one atomic layer form at the surface site nearby the SF (Figure 4.2c and 4.2k). With further compressive loading, the atomic-scale surface steps migrate upward and downward along the {111} sidewall, reducing the width of the Ag nanocrystal by one atomic layer (Figure 4.2d-e and 4.2l).

Akin to the SF, twin boundary (TB), formed through a series of 30° partial dislocation slip on successive {111} planes, could also be a preferential site for initiating surface atom diffusion, causing thinning in Ag nanocrystal under <112>-compression (Figure 4.2f-i). As shown in Figure 4.2f and 4.2m, the step height at the TB, viewed along the $[\bar{1}10]$ direction, is one-third of one atomic layer, same as the step height induced by an individual partial dislocation slip. The surface atoms at the TB, having a lower coordination number, sustain a higher chemical potential than the surface atoms elsewhere. The rapid surface diffusion of Ag atoms at the TB, driven by curvature, applied stress, surface energy and TB energy (see Section 4.4.1), results in the formation of an atomic-scale surface step with a height of one atomic layer (Figure 4.2g and 4.2n). Subsequently, the one-atomic-layer surface-step continuously migrates towards the end of the nanocrystal, decreasing the Ag nanocrystal's width by one atomic layer (Figure 4.2h-i and 4.2o). It should be noted that partial dislocation slip can only result in local lattice reorientation and the formation of a surface step with a height of one-third of one atomic layer at the SF/TB site, without changing the number of atomic layers of the nanocrystal's width. The occurrence of the SF/TB does not necessarily lead to surface diffusion, but the SF/TB sites act as the preferential sites for initiating new diffusional events at free surface.

Figure 4.3 shows that not only the partial dislocation activities, but also full dislocation slip could activate surface atomic diffusion, causing thinning in Ag nanocrystal during compressive loading. As shown in Figure 4.3a, a pristine 5.0-nm-diameter Ag nanocrystal is compressed along <112>-direction at room temperature under a strain rate of 10^{-3} s^{-1}. Figure 4.3a-b show that one full dislocation slip results in the formation of two one-atomic-layer surface steps on both sides of the Ag nanocrystal, increasing the width of the Ag nanocrystal from 19 to 20 atomic layers. Given that 1/2[110] slip on the inclined $(\bar{1}11)$ or $(1\bar{1}1)$ plane could not be directly observed along $[\bar{1}10]$-

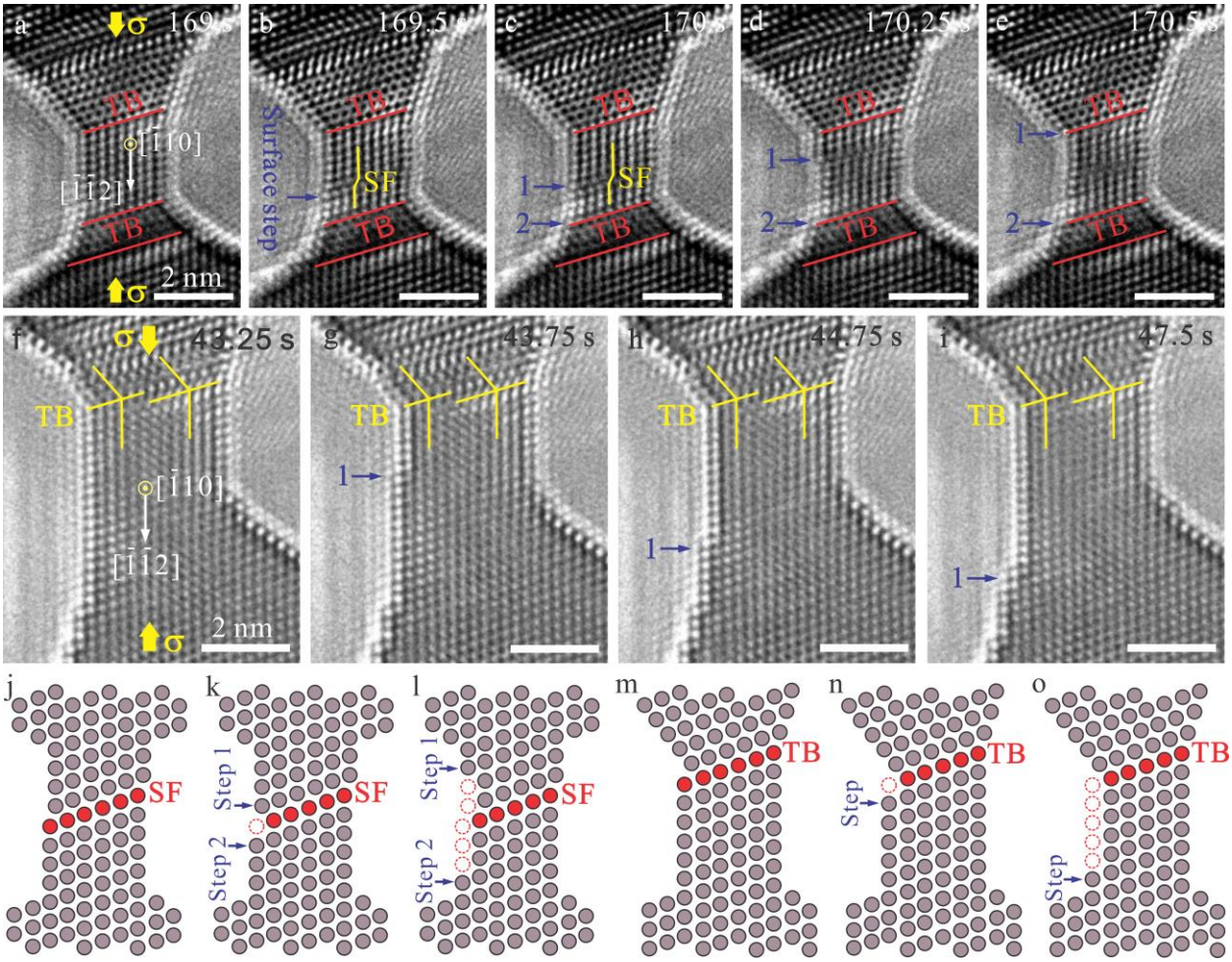

Figure 4.2 ***In*** **situ TEM observation of partial-dislocation-slip-activated surface atom diffusion in a Ag nanocrystal. (a) A deformed Ag nanocrystal with an original diameter of 4.3 nm under [$\bar{1}\bar{1}$2] compression loading. Red lines represent twin boundaries. (b) Nucleation and propagation of a partial dislocation, leaving behind a stacking fault and a 1/3-atomic-layer surface step at the stacking fault site. (c) Formation of two surface steps (steps 1 and 2) on the {111} surface of the nanocrystal near the stacking fault site. (d-e) Sequential TEM images showing the continuous migration of surface steps towards the nanocrystal's end. (f) A deformed 4.3-nm Ag nanocrystal loaded along [$\bar{1}\bar{1}$2] direction. A surface step with a height of one-third of one atomic layer exists at the twin boundary. Yellow lines represent twin boundaries, introduced by a series of partial dislocation slip. (g) Formation of a one-atomic-layer step at the nanocrystal surface. (h-i) Continuous step migration towards the nanocrystal end. All the scale bars are 2 nm. (j-l) Schematic illustration of partial-dislocation-slip-activated surface atom diffusion. (m-o) Schematic illustration of surface atom diffusion at twin boundary. The red circles with dashed line represent the disappeared atom columns after surface diffusion.**

viewing direction, the slip event is further confirmed by quantitatively monitoring the change in gauge length between the two boundaries of the gauge section[150, 151] (the white and yellow dashed lines in Figure 4.3a-b[28, 42]). The full dislocation slip results in an abrupt length change of 0.17 nm (Figure 4.3b), which is in good agreement of the projection of a 1/2[110] slip on the [11$\bar{2}$] loading direction. With further compressive loading, the two as-formed surface steps migrate towards the ends of the nanocrystal continuously (Figure 4.3c-d), giving rise to a self-healing behavior, as

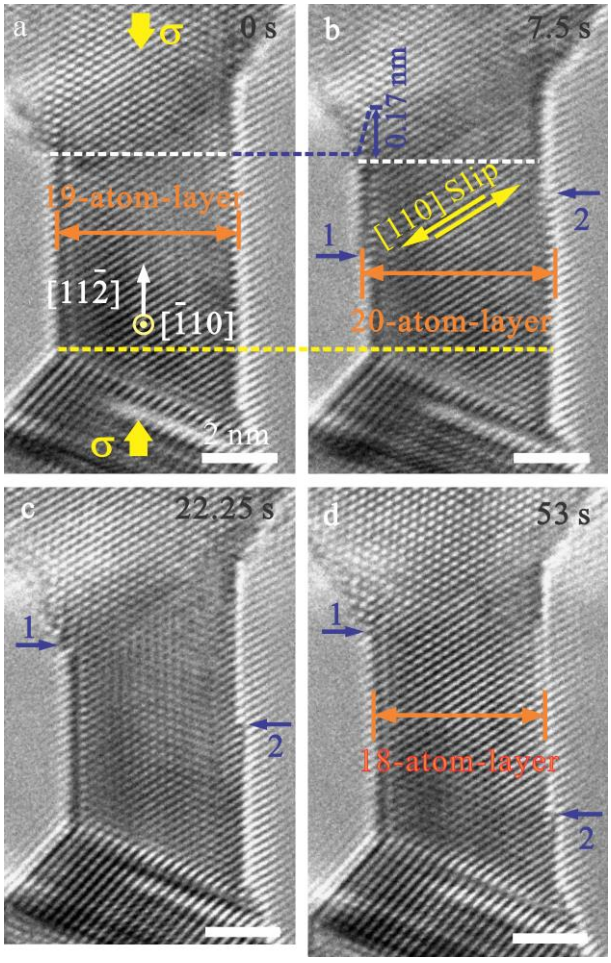

Figure 4.3 *In situ* TEM images showing full-dislocation-slip-induced surface atom diffusion. (a) TEM image of a 5.0-nm-diameter Ag nanocrystal under [11$\bar{2}$] compression at a strain rate of 10^{-3} s^{-1}. (b) Formation of two surface steps (steps 1 and 2) induced by a full dislocation slip. (c-d) Migration of surface steps on the {111} sidewall resulting in the reduction of the nanocrystal's width. All the scale bars are 2 nm.

reported by Zhong *et al.*[37] in the tensile tests of Ag nanocrystals. The continuous flow of surface steps ultimately decreases the width of the Ag nanocrystal by two atomic layers. Consequently, each diffusional events at free surface, activated by full dislocation slip, reduces the nanocrystal's width by one atomic layer. The experimental observation of the continuous movement of the one-atomic-layer surface step upon compression is theoretically attributed to the stress- and curvature-driven surface atom diffusion (see Section 4.4.1)[37, 39, 42]. The atoms at the step edge sequentially hop on {111} planes along <112> direction and diffuse towards the ends of the nanocrystal to reduce the overall energy of the system, resulting in the continuous surface ledge flow.

4.3.3 Surface-Diffusion-Induced Unusual Compression Fracture In Ag Nanocrystal

During the compression of the 4.3-nm-diameter Ag nanocrystal, a synergy of consecutively activated multiple thinning events discovered above gives rise to a continuous decrease in the width of the Ag nanocrystal, as shown in Figure 4.4a-b. With decreasing width, the chemical potentials of the surface atoms increase, driving surface mass transport more quickly[37, 95]. As the diameter reduces to 1.71 nm (Figure 4.4b), curvature- and stress-driven surface atom diffusion leads to the abnormal compression fracture of the Ag nanocrystal, which is akin to the failure process in the tensile tests of Ag nanocrystals[37]. Accompanied with the tensile-fracture-like failure, two tapered nanotips with the sizes being 0.51 nm and 0.96 nm form, as shown in Figure 4.4c. With the elapse of time, the curvature radii of the 0.51- and 0.96-nm-sized nanotips increase to 1.49 nm and 3.81 nm, respectively, and meanwhile the lengths of both nanotips decrease (Figure 4.4c-e), exhibiting a liquid-drop-like retraction behavior without dislocation activities and lattice structure change. The observed retraction behavior is driven by the high surface pressure of the fractured nanocrystal[35], which can be expressed as[35, 61, 86]

$$P=\frac{2\gamma}{R}, \tag{4.1}$$

where R is the curvature radius of the fracture tip and γ is the surface energy. Taking the surface energy of Ag as 1.25 J/m^2 [35], the surface pressure for the fractured Ag nanocrystal with a curvature radius of 0.51 nm is 4.90 GPa, comparable to the ultimate strength for nanoscale Ag in the range of 0.87 GPa to 4.84 GPa[171, 229]. Such high surface pressure is sufficient to break the surface atomic bonds, and thus activates atom transport along the free surface, resulting in the liquid-like retraction behavior in the fractured Ag nanocrystals.

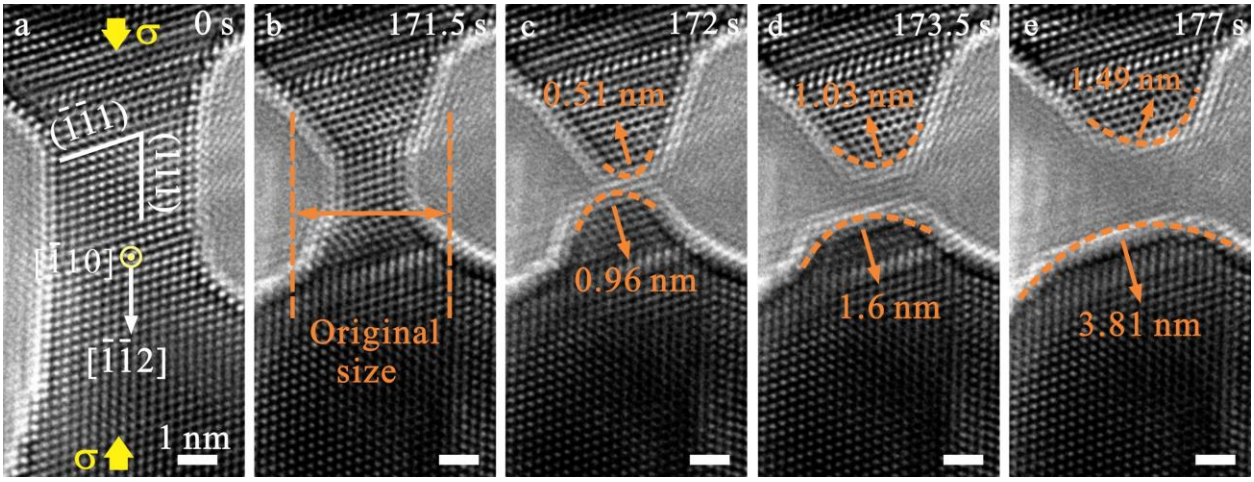

Figure 4.4 Atomic-scale processes of diffusion-induced compression fracture in a Ag nanocrystal. (a-b) Decrease in the width of the nanocrystal resulting from surface atom diffusion activated by preexisting dislocations and crystal slip. The original and ultimate diameters of the Ag nanocrystal are 4.3 nm and 1.71 nm, respectively. (c) Surface-diffusion-induced unusual compression fracture of the Ag nanocrystal, forming two tapered nanotips with the curvature radii of 0.51 nm and 0.96 nm, respectively. (d-e) A series of TEM images showing liquid-drop-like retraction behavior in the fracture Ag nanocrystal. With the elapse of time, the curvature radii of the 0.51- and 0.96-nm-sized nanotips increase to 1.49 nm and 3.81 nm, respectively. All the scale bars are 1 nm.

4.3.4 The Universality Of The Occurrence Of Abnormal Thinning And Compression Fracture In Ag Nanocrystals During Compression

Very recently, Zhong *et al*.[37] reported that the diffusion stability limit for Ag nanocrystal was estimated to be 15 nm, above which surface diffusion was quite limited. To demonstrate the universality of the abnormal thinning and compression fracture observed in the sub-15-nm-sized Ag nanocrystals during compression, a 16.2-nm-diameter Ag nanocrystal is compressed along <112>-direction at room temperature under a strain rate of 10^{-3} s^{-1}. When the elastic compressive strain inside the Ag nanocrystal reaches to a yielding point, a full dislocation nucleates from the free surface and then glides through the nanocrystal, leaving behind surface steps with a heigh of one atomic layer (Figure 4.5a-b). The migration of the surface step toward the end of the Ag nanocrystal leads to the reduction of the nanocrystal's width from 57 atomic layers to 56 atomic layers (Figure 4.5c). With further compressive loading, each full dislocation slip and the subsequent migration of surface step result in the decrease of the nanocrystal's width by one atomic layer, as shown in Figure 4.5d-i. Consequently, slip-activated surface atom diffusion gives rise to consecutive thinning events, leading to the continuous decrease in the nanocrystal's width from 16.2 nm to 2.65 nm (Figures 4.5 and 4.6a-d). When the nanocrystal's width decreases to the critical size of 2.65 nm, the breaking of atomic bonds and the diffusion of surface atoms ultimately lead to the tensile-fracture-like failure (Figure 4.6e), as observed in the sub-15-nm-sized Ag nanocrystals. Subsequently, liquid-drop-like retraction behavior, driven by surface pressure, occurs in the fractured nanocrystal, leaving behind two flat and round nanotips (Figure 4.6f-h). Moreover, in all the Ag nanocrystals with an aspect ratio ranging from 0.68 (Figure 4.1) to 2.1 (Figure 4.7) and tested by *in situ* TEM under the strain rate of 10^{-3} s^{-1}, unusual thinning and compression fracture, mediated by surface atom diffusion, occur.

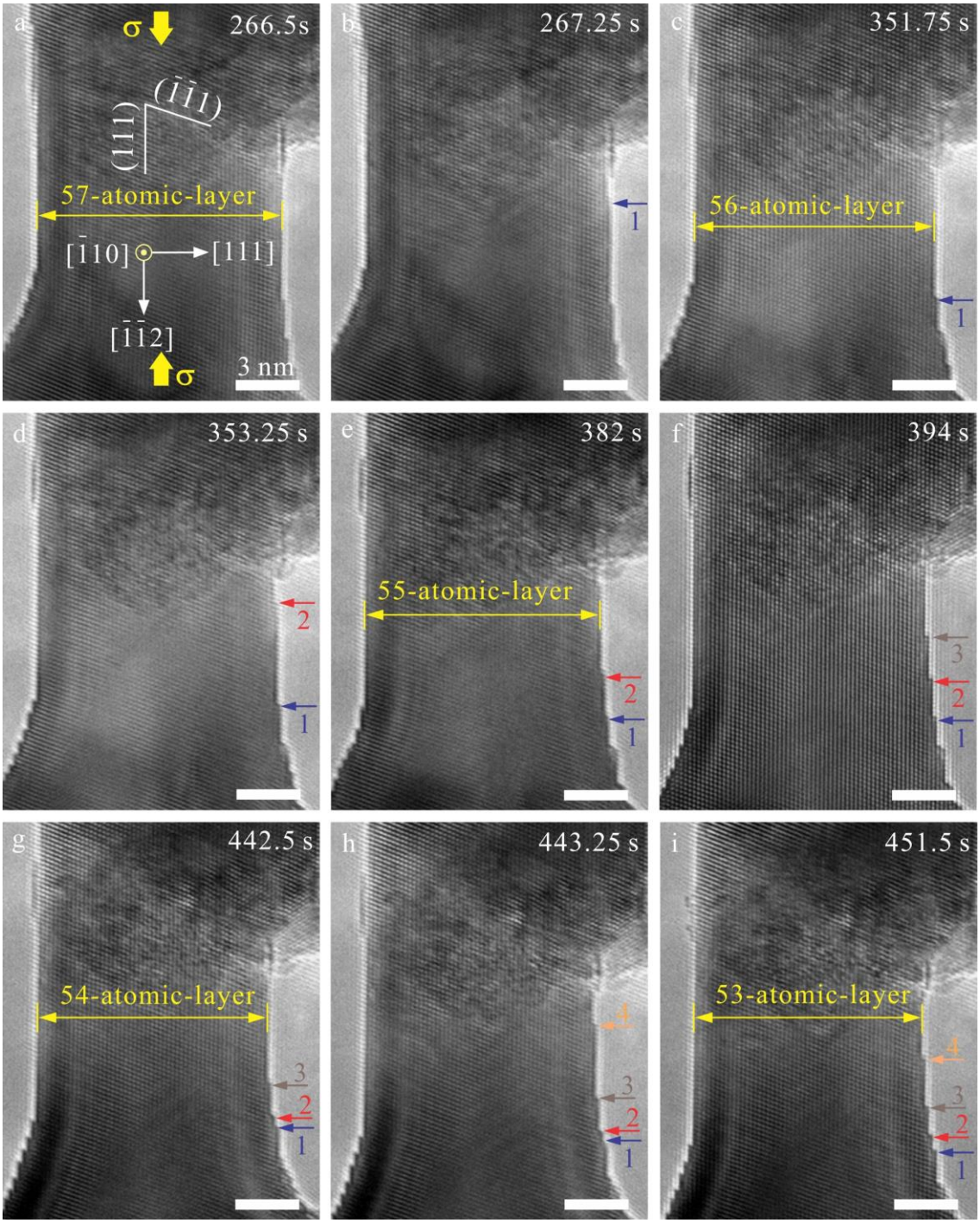

Figure 4.5 Slip-activated surface atom diffusion in a Ag nanocrystal during compression. (a-i) A series of TEM images of the deformed 16.2-nm-diameter Ag nanocrystal under [$\bar{1}\bar{1}$2]-compression before (a, c, e, g) and after (b, d, f, h) full dislocation slip. Each full dislocation activity reduces the nanocrystal's width by one atomic layer (c, e, g, i). All the scale bars are 3 nm. Each surface step migration is tracked by an arrow of a specific color.

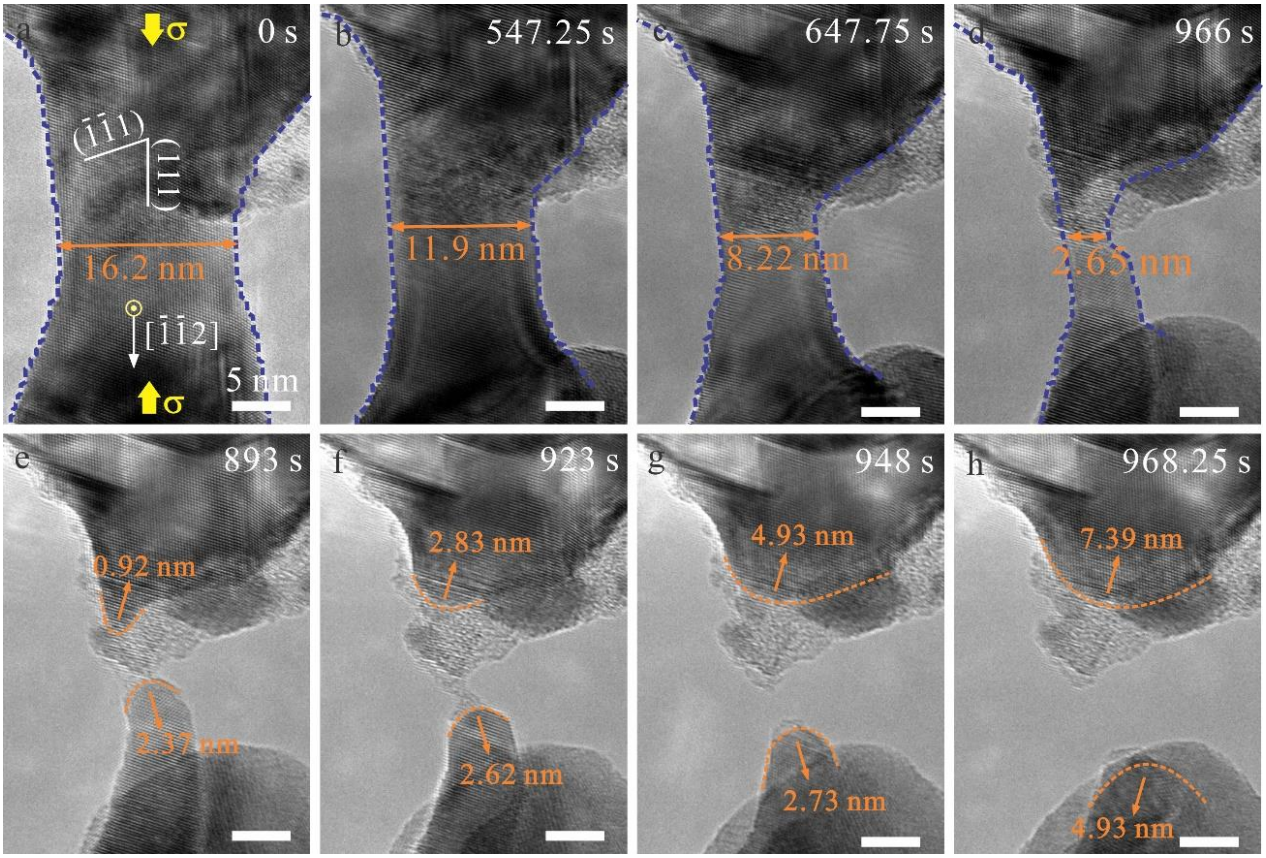

Figure 4.6 ***In situ*** **atomic-scale compression test of a Ag nanocrystal. (a) TEM image of a pristine 16.2-nm-diameter Ag nanocrystal under <112> compression at room temperature under a strain rate of 10^{-3} s^{-1}. (b-d) Consecutive thinning in Ag nanocrystal caused by dislocation-slip-activated surface atom diffusion. (e) Surface-diffusion-induced unusual compression fracture, forming two tapered Ag nanotips. (f-h) Sequential TEM images showing liquid-like retracting behavior in the fractured Ag nanocrystals. The curvature radii and lengths of the nanotips increase and decrease, respectively. All the scale bars are 5 nm.**

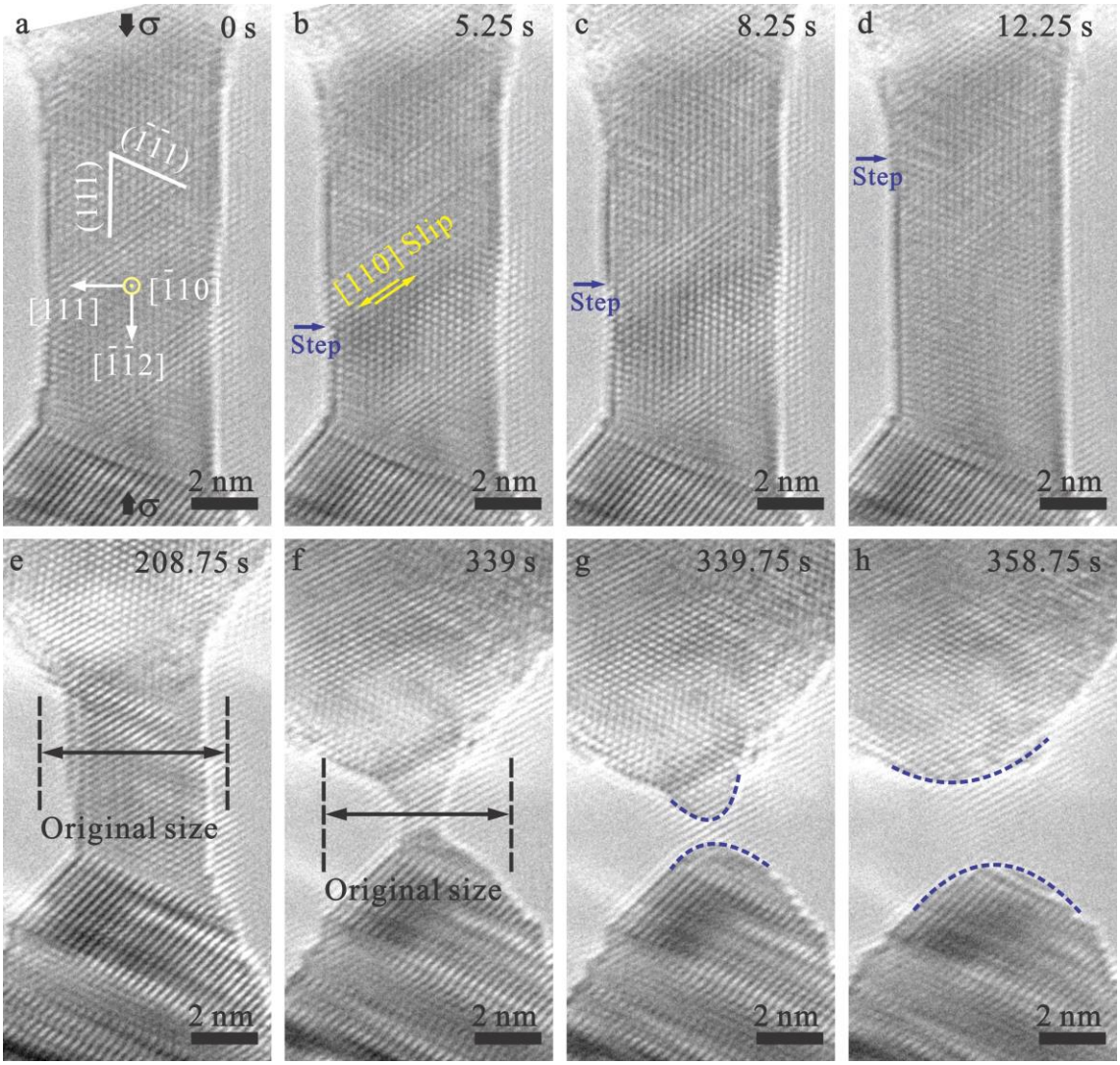

Figure 4.7 *In situ* TEM compression test of 5.2-nm-diameter Ag nanocrystal at room temperature under the strain rate of 10^{-3} s^{-1}. (a) TEM image of the as-fabricated Ag nanocrystal with the aspect ratio of 2.1 under <112> compression. (b-d) Surface atom diffusion in Ag nanocrystal activated by full dislocation slip. The migration of the surface step is tracked by an arrow. (e-f) Continuous decrease in the nanocrystal's width caused by slip-activated surface diffusion. (g) Surface-diffusion-induced compression fracture, forming two tapered nanotips. (h) Liquid-like retracting behavior in the fractured Ag nanocrystal. All the scale bars are 2 nm.

4.3.5 Compression-Induced Thickening In Ag Nanocrystal At A High Strain Rate

To further probe the compressive deformation behaviors in Ag nanocrystals, *in situ* compression test of a pristine 6.1-nm-diameter Ag nanocrystal at room temperature under a high stain rate of 0.06 s^{-1} is performed along <112>-direction (Figure 4.8). As shown in Figure 4.8a, the as-fabricated Ag nanocrystal before mechanical test is defect free. Under compressive loading, a series of partial dislocations slip occur on the neighboring {111} planes in a layer-by-layer fashion, resulting in the formation of a deformation twin (Figure 4.8b-c). Upon compression, nearly no diffusional events are observed at the nanocrystal surface. Different from the abnormal thinning and compression fracture in the Ag nanocrystal at a strain rate of 10^{-3} s^{-1}, consecutive thickening, mediated by dislocation slip, is observed in the Ag nanocrystal at a high strain rate of 0.06 s^{-1}, which is attributed to the strain-rate sensitive nature of diffusional mechanisms[37, 42, 65]. Quite limited surface atom diffusion occurs at a high strain rate, which is incapable of eliminating the surface steps formed by dislocation slip. Consequently, dislocation slip continuously generate nearly immobile surface steps, resulting in thickening upon compressive loading. Hence, the occurrence of unusual thinning and fracture during the compression of the Ag nanocrystal, resulting from coupled displacive-diffusive deformation, requires that the crystal thinning rate arising from surface atom diffusion be larger than the thickening rate from crystal slip. For a Ag nanocrystal tested at room temperature, there is a critical strain rate, below and above which thinning and thickening, mediated by coupled displacive-diffusive deformation, could occur in the nanocrystal, respectively. In addition to the applied strain rate, the sample dimensions (diameter, length and aspect ratio) and the type of materials (surface mobility and surface energy) also affect the competition between crystal slip thickening and diffusion thinning in metallic nanocrystal during compression[35, 37, 39, 65].

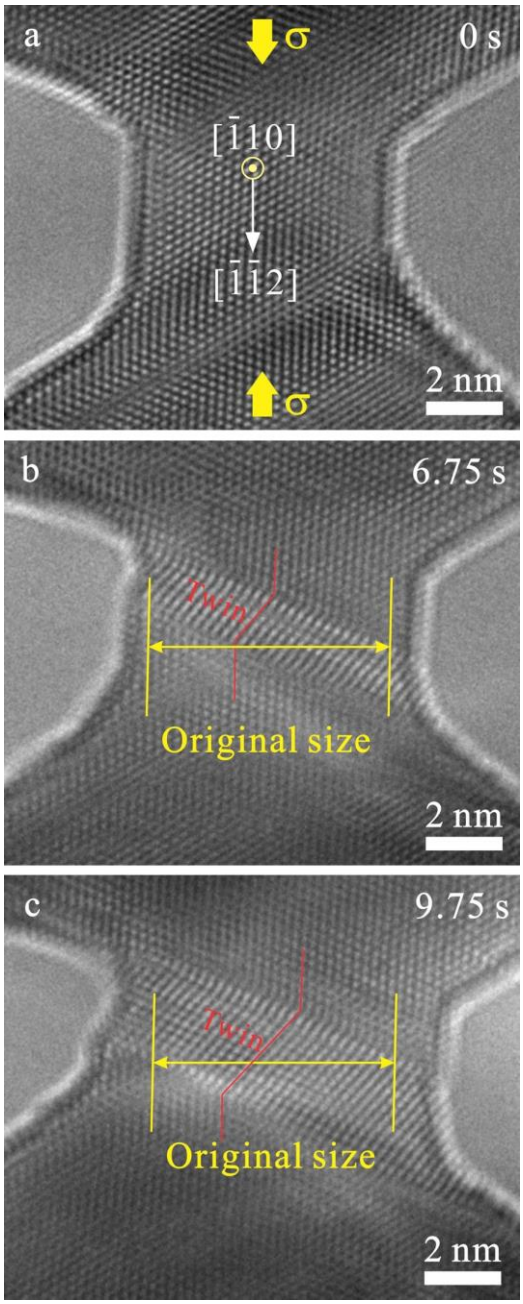

Figure 4.8 Compression-induced thickening in a Ag nanocrystal loaded at a high strain rate of 0.06 s^{-1}. (a) TEM image of a pristine 6.1-nm-diameter Ag nanocrystal under <112> compression loading at room temperature. (b-c) Sequential TEM images showing consecutive thickening in the Ag nanocrystal, mediated by deformation twinning. All the scale bars are 2 nm.

4.3.6 Pure-Displacive-Plasticity-Induced Thickening During The Compression Of Pt Nanocrystals

In contrast to the surface-diffusion-mediated thinning and compression fracture in the Ag nanocrystals, consecutive thickening, mediated by pure displacive deformation, is observed in Pt nanocrystal. Figure 4.9 shows the atomic-scale processes of a 2.0-nm-diameter Pt nanocrystal under <112>-compression at room temperature and a strain rate of 10^{-3} s^{-1}. Before mechanical loading, no lattice defects exist in the Pt nanocrystal, as shown in Figure 4.9a. As the lattice stress inside the Pt nanocrystal reaches to a yielding point (Figure 4.9b), full dislocation slip occurs, causing that the height of step 1 and the width of the nanocrystal increase by one atomic layer, respectively (Figure 4.9c). With further compressive loading, pure displacive deformation is the dominant mechanism with each full dislocation slip increasing the width of the Pt nanocrystal by one atomic layer (Figure 4.9d-g). During compression, the height change of the surface steps (steps 1 and 2) are caused by full dislocation slip instead of surface atom diffusion, and step migration is not observed. Eventually, a series of full dislocation slip increase the width of the Pt nanocrystal from 2.0 nm to 4.0 nm (Figure 4.9h), which is consistent with the dislocation-slip-mediated thickening behaviors reported in Au[230, 231], molybdenum (Mo)[230, 231, 232, 233, 234], tungsten (W)[232, 234], tantalum (Ta)[232, 234], niobium (Nb)[232, 234] and nickel (Ni)[40, 235] sub-micrometer pillars upon compression. The dramatic differences in compressive deformation behaviors between the Ag and Pt nanocrystals are attributed to the difference in the activation energy barrier and surface mobility for self-diffusion. The activation energy barriers for surface atom diffusion in Ag and Pt are 0.064 eV and 0.171 eV, respectively and the surface mobilities for Ag and Pt are 1.4×10^{4} $m^{2}\cdot J^{-1}\cdot s^{-1}$ and 4.3 $m^{2}\cdot J^{-1}\cdot s^{-1}$, respectively[37, 42]. Compared to Ag, higher activation energy barrier and lower

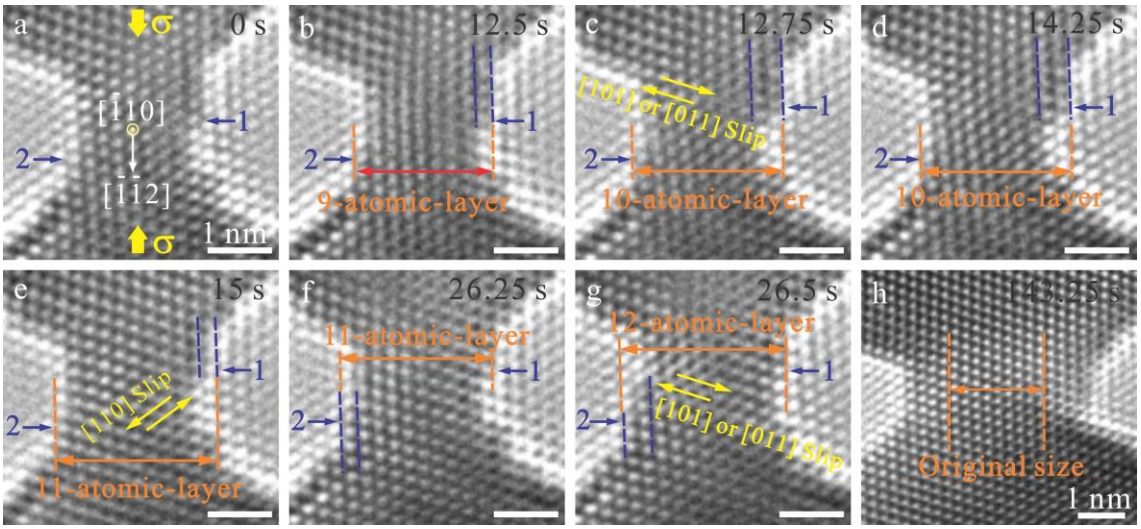

Figure 4.9 Consecutive thickening mediated by pure displacive deformation in Pt nanocrystal during compression. (a) TEM image of a pristine 2.0-nm-diameter Pt nanocrystal under <112> compression at room temperature under a strain rate of 10^{-3} s^{-1}. (b-g) A series of TEM images of the Pt nanocrystal before (b, d, f) and after (c, e, g) dislocation slip. Each full dislocation slip increases the width of the Pt nanocrystal by one atomic layer (c, e, g). Surface atom diffusion is not observed during compression, and the surface steps remain immobile. (h) The nanocrystal's width ultimately increases to 4.0 nm, resulted from consecutive full dislocation slip. All the scale bars are 1 nm.

surface mobility for self-diffusion in Pt cause that surface atom diffusion in the Pt nanocrystal is quite limited[37, 42], which is incapable to eliminate the surface steps formed by dislocation slip.

4.4 Discussion

4.4.1 Thermodynamic Consideration For Surface Atom Diffusion In Ag Nanocrystal

According to the previous theories on surface atom diffusion, the chemical potential change for a surface atom migrating on {111} surface sidewall from the middle segment towards the end of a nanocrystal can be expressed as[33, 36, 117, 145]

$$\Delta E = -\left(\frac{\gamma_{111}}{\rho D} + \frac{\gamma_{110}}{\rho R}\right), \tag{4.2}$$

where D and R are the diameter and thickness of the middle segment of the nanocrystal, respectively, γ_{111} and γ_{110} are the surface energies of {111} and {110} planes, respectively and ρ is the bulk density. The energy change caused by the applied stress is given by

$$\Delta E = -\frac{E\varepsilon^2}{2\rho}, \tag{4.3}$$

where E is the Young's modulus along the compression loading direction and ε is the elastic strain during compression. Thus, the chemical potential change for a surface atom migrating from the middle segment to the end of the nanocrystal can be obtained by combining equations (4.2) and (4.3):

$$\Delta E = -\left(\frac{\gamma_{111}}{\rho D} + \frac{\gamma_{110}}{\rho R} + \frac{E\varepsilon^2}{2\rho}\right) \tag{4.4}$$

Based on equation (4.4), the experimental observation of the continuous movement of the one-atomic-layer surface step towards the ends of the Ag nanocrystal upon compression is attributed to stress- and curvature-driven surface atom diffusion (Figure 4.10). The atoms present on the step edge sequentially migrate towards the nanocrystal end, reducing the overall system energy. The diffusional pathway for the surface atoms present at the step edge should follow the

pathway for surface atom diffusion proposed by Wang *et al*.[42] and Zhong *et al*.[37], where the atoms at the step edge on {111} planes sequentially hop along <112> direction.

Given that partial dislocation slip can introduce a SF and results in local lattice reorientation changing the surface sidewall from {111} to {100} planes, the total energy change for a surface atom migrating from the SF site to the end of the nanocrystal can be expressed as[95, 236]

$$\Delta E = -\left(\frac{\gamma_{100}}{\rho D} + \frac{\gamma_{110}}{\rho R} + \frac{E\varepsilon^2}{2\rho} + \frac{\gamma_{SF}}{2\rho_{111}}\right), \tag{4.5}$$

where γ_{100} is the surface energy of the {100} plane, γ_{SF} is the stacking fault energy and ρ_{111} is the area density of the {111} plane. Hence, in addition to the applied stress and the curvature, stacking fault energy and the increase in surface energy also contribute to the driving force for surface atom diffusion at the SF site. Similarly, the potential drop for a surface atom migrating from the TB to the end of the nanocrystal is given by

$$\Delta E = -\left(\frac{\gamma_{100}}{\rho D} + \frac{\gamma_{110}}{\rho R} + \frac{E\varepsilon^2}{2\rho} + \frac{\gamma_{TB}}{2\rho_{111}}\right), \tag{4.6}$$

where γ_{TB} is the twin boundary energy. Based on equations (4.5) and (4.6), compared to the atoms at other surface sites, the surface atoms at the SF/TB sites sustain a higher energy, which results from local lattice reorientation and an additional SF/TB energy introduced by partial dislocation slip. The SF/TB site could be preferential sites for initiating surface atom diffusion based on the thermodynamic consideration. Though the atomic-scale observations in this work fall short in capturing the diffusional events of the surface atoms at the SF site, TB and the irregular surface nearby the preexisting dislocations, their diffusional pathway should be similar to that for atomic diffusion at the surface step with a height of one atomic layer.

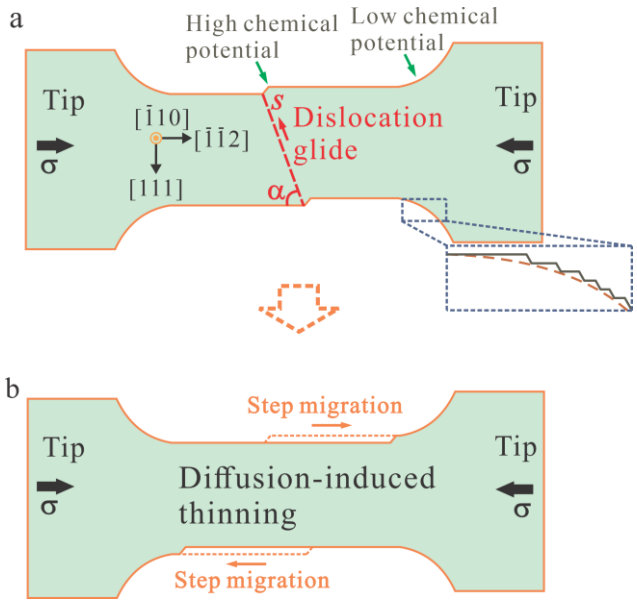

Figure 4.10 Schematics showing coupled-displacive-diffusive-plasticity-induced thinning in a Ag nanocrystal during compression. (a) Formation of two surface steps with high chemical potential after crystal slip. (b) Surface-atom-diffusion-assisted migration of atomic step towards the end of the Ag nanocrystal.

4.4.2 The Rates Of Thickening By Dislocation Slip And Thinning By Surface Atom Diffusion

The occurrence of unusual thinning in Ag nanocrystal under compression depends on the competition between the thinning by surface atom diffusion and the thickening by crystal slip. The thickening rate ($\frac{\Delta D}{\Delta t}$) arising from crystal slip (Figure 4.10a) can be obtained by[37, 237]

$$\frac{\Delta D}{\Delta t}=\frac{\Delta s}{\Delta t}\sin\alpha=\frac{L\sin\alpha}{\cos\alpha-(\varepsilon_0\frac{L}{D})\sin\alpha}\dot{\varepsilon}, \tag{4.7}$$

where $\dot{\varepsilon}$ is the applied strain rate, α is the angle between the slip direction and the loading direction, ε_0 is elastic strain limit, L and D are the length and diameter of the metallic nanocrystal, respectively. The thickening rate by crystal slip in Ag nanocrystal under <112>-compression is

related to the applied strain rate and the sample dimensions (diameter, length and aspect ratio). The thinning rate ($\frac{\Delta D}{\Delta t}$) by surface atom diffusion in the nanocrystal with a square cross-sectional shape (Figure 4.10b) can be expressed as[37, 238]

$$\frac{\Delta D}{\Delta t} = -\frac{8\delta_s \mu_s \Delta E}{L^2} = \frac{8\delta_s \mu_s}{L^2 \rho}\left(\frac{\gamma_{111}}{D} + \frac{\gamma_{110}}{D} + \frac{E\varepsilon_0^2}{2}\right), \quad (4.8)$$

where δ_s is the thickness of the migrating atoms at surface, μ_s is surface mobility, γ_{111} and γ_{110} are the surface energies of {111} and {110} planes, respectively, ρ is the bulk density, E is the Young's modulus along the compression direction, ε_0 is the elastic strain limit, L and D are the length and diameter of the metallic nanocrystal, respectively. The thinning rate by surface atom diffusion is related to the sample dimensions and the type of materials. According to the above analysis, whether thinning or thickening occur in the Ag nanocrystal under <112>-compression at room temperature is related to the applied strain rate and the sample dimensions. Based on equations (4.7) and (4.8) and the parameters for Ag nanocrystal listed in Table 4.1, the rates of thickening by crystal slip and thinning by surface diffusion for the 5-nm-diameter Ag nanocrystal with L =5.17 nm, L/D=1.14 and α=54.5° during the compression test at the strain rate of 10^{-3} s^{-1} (Figure 4.3) are estimated to be 7.5×10^{-3} nm·s^{-1} and 13.75 nm·s^{-1}, respectively. Compared to the thickening rate, the thinning rate is much larger, suggesting that thinning occurs in the Ag nanocrystal, which is consistent with the experimental observation (Figure 4.3). Likewise, for the 16.2-nm-diameter Ag nanocrystal (L=9.5 nm, L/D=0.59 and α=54.5°) loaded at the strain rate of 10^{-3} s^{-1} (Figure 4.5), the dislocation slip thickening and the diffusion thinning rates are calculated to be 1.4×10^{-2} nm·s^{-1} and 1.39 nm·s^{-1}, respectively, indicating the occurrence of thinning in Ag nanocrystal, which has been corroborated by the experimental results (Figure 4.5 and 4.6). The quantitative analysis on the rates of thickening by dislocation slip (1.7×10^{-2} nm·s^{-1}) and thinning

Table 4.1 Parameters used in the calculation of the thickening rate by crystal slip and the thinning rate by surfact atom diffusion.

Ag nanocrystal	
Young's modulus E (GPa)	83.61 [28]
Elastic strain limit ε_0	0.034 [37]
The thickness of the migrating surface atoms δ_s (nm)	0.33 [37]
Bulk density ρ (m^3)	5.82×10^{28} [37]
Surface mobility μ_s ($m^2 \cdot J^{-1} \cdot s^{-1}$)	1.4×10^{4} [37]
Surface energy γ_{111} ($J \cdot m^{-2}$)	1.17 [239]
Surface energy γ_{110} ($J \cdot m^{-2}$)	1.24 [239]

by surface diffusion (2.73 $nm \cdot s^{-1}$) is also applicable to the 5.2-nm-diameter Ag nanocrystal (L=10.92 nm, L/D=2.1 and α=54.5°) loaded at the strain rate of 10^{-3} s^{-1}, where thinning caused by coupled displacive-diffusive deformation is observed (Figure 4.7).

4.4.3 The Conditions For The Occurrence Of Thinning And Compression Fracture In Nanoscale Metals

Different from the prior study that dislocation-free diffusional deformation mediated liquid-like thickening during the compression of a sub-10-nm Ag nanoparticle[39], this work reveals that coupled displacive-diffusive deformation induces thinning and tensile-fracture-like failure during the compression of the Ag nanocrystal, which may be attributed to the different sample shapes and experimental conditions. Given that the surface-to-volume ratio of nanostructured metals is size- and shape-dependent, surface atom diffusion in nanoparticle is stronger than that in nanocrystal with the same size[53, 240, 241]. Furthermore, the compression test of the Ag nanoparticle was conducted through the movement of Ag-nanoparticle-decorated W tip toward ZrO_2 surface,

during which Ag-W and Ag-ZrO_2 interfaces could act as a highway for diffusional events upon loading (Figure 4.11). Coble-like diffusional processes at heterogeneous interfaces and free surfaces were sufficient to accommodate the applied strain on the nanoparticle, causing continuous liquid-like-thickening (Figure 4.11). In contrast, no GBs or heterogeneous interfaces exist between the Ag nanocrystal and the substrate in this study. Given that the contribution of bulk diffusion to strain is quite limited at room temperature[95], additional displacive mechanisms should be activated in the Ag nanocrystal to accommodate deformation, generating atomic-scale steps at free surfaces, as shown in Figure 4.10a. Due to curvature- and stress-driven diffusional flow of surface atoms, the atoms at surface step edge with high chemical potential migrate towards the two ends of the nanocrystal with low chemical potential, causing consecutive thinning and the ultimate compression fracture in Ag nanocrystals (Figure 4.11b).

The findings in this work indicate that surface atom diffusion plays a critical role in the compression-induced thinning and fracture in the Ag nanocrystals, in contrast to the recent observations in FCC and BCC sub-micro pillars fabricated by focused ion beam (FIB) cutting, in which thickening behaviors, resulting from dislocation slip, were observed during compression[40, 230, 231, 232, 233, 234, 235]. Such difference in the compressive deformation behaviors between the

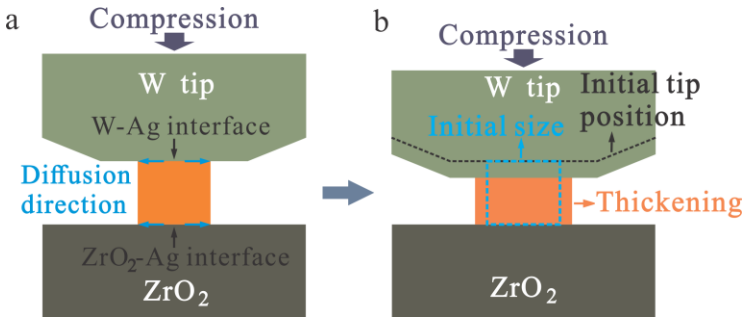

Figure 4.11 Schematics showing the process of the liquid-like thickening during the compression of a sub-10-nm Ag nanoparticle.

metallic nanocrystals and the sub-micro pillars may come from the following reasons: (1) The sample diameters of the nanocrystals adopted in this work (4.3 nm, 5.0 nm and 16.2 nm) are much smaller than those for the submicron-sized pillars. Given that the competition between the displacive and diffusive deformations is size-dependent[55, 65, 80], weak or even no surface atom diffusion may occur in the submicron pillars. (2) Compared to the Au, Mo, W, Ta, Nb and Ni sub-micro pillars, the melting point for the Ag nanocrystal is lower. Surface atom diffusion, depending on the ratio of experimental temperature and melting point of materials[35, 65], is stronger in low-melting-point metals tested at room temperature, compared to the high-melting-point ones. In addition, with the reduction in the sample size, the melting point decreases and the diffusion coefficient increases[242]. Hence, surface atom diffusion could be observed in the Ag nanocrystals rather than the other various metallic sub-micro pillars. For the metallic nanocrystals with a melting point higher than that of Pt nanocrystal (e.g. W, Mo, Ta and Nb), crystal-slip-mediated thickening is expected to occur under room-temperature compression, since surface atom diffusion is quite limited. In contrast, for the metallic nanocrystals with a low melting point (e.g. Sn, Ag, Au and Cu), slip-activated surface atom diffusion or pure diffusive deformation is expected to occur, causing thinning in the nanocrystals under room-temperature compression. (3) *In situ* nanowelding is employed in this study to fabricate Ag nanocrystals with clean surface, which are ideal for studying surface diffusive plasticity[37, 96], By contrast, surface oxidation/contamination layer, introduced by FIB cutting, probably suppresses mass transport along the free surface of the submicron pillars in the previous studies[53].

To date, the consecutively occurring thinning and the ultimate tensile-fracture-like failure during the compression of Ag nanocrystal presented in this study have never been reported before, due to the technical difficulties in fabricating nanoscale metals with clean surface. Together with

the previous studies[230, 231, 232, 233, 234, 235], this work provides a comprehensive understanding of the atomic-scale compressive deformation behaviors in small-sized metals. The coupled displacive-diffusive deformation studied here may be relevant to the similar interplay between intragranular crystal slip and diffusional events at GBs in bulk nanocrystalline metals with small feature size and low melting point, given that free surface and GBs both play similar roles in mediating displacive and diffusive plasticity[37].

4.5 Conclusion

In conclusion, *in situ* HRTEM compression experiments have revealed that preexisting dislocation and crystal slip serve as stimuli to activate surface atom diffusion, resulting in abnormal thinning in Ag nanocrystals during compression. As the width of the Ag nanocrystal decreases to a critical size, unusual tensile-fracture-like failure occurs, which results from atomic bond breaking and the diffusion of surface atoms. The occurrence of thinning and compression fracture in the metallic nanocrystals is related to the applied strain rate, the sample dimensions and the types of materials. Different from the coupled displacive-diffusive deformation in the Ag nanocrystals, pure displacive deformation leads to continuous thickening in Pt nanocrystals during compression. This study advances the current understanding of compressive deformation behaviors in small volume metals, which will enable the realization of their practical applications in high-performance electrical devices.

5.0 In Situ Atomic-Scale Observation Of Fivefold Twin Formation In Nanoscale Crystal Under Mechanical Loading

(*Portions of this chapter have been reproduced with permission from Nano Letters, Volume 23, Issue 2, Pages 514-522. Copyright 2023 by American Chemical Society.*)

In this chapter, the atomic-scale formation process of fivefold twin in gold nanocrystal under mechanical loading will be studied. As a special twinning structure, fivefold twin is usually observed in nanostructured metals after mechanical tests and/or annealing treatment. However, the formation mechanism of fivefold twin has not been fully elaborated, due to lack of direct atomic-scale observation of their dynamic formation process. Here, by using *in situ* high-resolution transmission electron microscopy combined with molecular dynamic simulations, it finds at the atomic scale that sequential twinning slip in varying slip systems and the decomposition of high energy grain boundary at the node of a multifold twin account for the fivefold twin formation in a nanoscale gold single crystal under bending as well as the reversible formation and dissolution of fivefold twin in the gold nanocrystal with preexisting twin under tension and shearing. Moreover, the complex stress state in the neck area results in the breakdown of Schmid law, causing the formation of fivefold twin in a gold nanocrystal with a twin boundary parallel to the loading direction. These findings enrich the current understanding of the formation process of high-order twin structures in metal materials.

5.1 Introduction

Twin boundaries (TBs) with low mobility and boundary energy could be used for tuning the mechanical properties of nanostructured metals[243, 244], which have drawn great interest in the field of interface engineering[52, 245]. As a special twinning morphology, fivefold twin (FFT) with five coherent TBs concurrently meeting at their common rotation axis along [110] has been widely observed in metallic nanowires[51, 197, 198], nanoparticles[246, 247], thin films[248] and nanocrystalline materials[102, 109, 125]. Compared to their twin-free counterparts, the nanostructured metals with FFT usually exhibit substantially improved mechanical properties[165, 166, 167, 171, 249, 250, 251]. It has been reported that the Young's modulus of chemically synthesized fivefold twinned silver (Ag) nanowires increased from 83 GPa to 176 GPa[167, 171], and the yield strength increased from 0.71 GPa to 2.64 GPa[171]. Controlling the introduction of FFT into nanostructured metals is of vital importance for fabricating high-performance materials, which requires the knowledge of the underlying formation mechanisms of FFT.

To date, some formation mechanisms of FFT have been proposed. For instance, Liao *et al.*[109, 123], An *et al.*[124] and Zhu *et al.*[125] reported that high external stress, orientation change in applied stress (ball milling and high-pressure torsion) and low experimental temperature were required to activate partial dislocation slip from grain boundaries (GBs) and TBs on different twinning systems, causing FFT formation in nanocrystalline metal materials. Furthermore, Huang *et al.*[129], Cao *et al.*[130] and Bringa *et al.*[131] demonstrated that FFT formed in nanocrystalline metals during annealing treatment at high temperature under zero external stress, where the splitting and migration of a GB segment[129, 132], grain rotation[130], stacking fault (SF) motion and overlapping[130] and successive partial emission driven by high internal stresses at TBs and GBs[131] were the dominant mechanisms. However, the formation mechanisms of FFT proposed in the previous

studies were all deduced from the postmortem TEM observations, which fell short in obtaining direct time-resolved atomic-scale observation. Complementary to the experimental observation, molecular dynamics (MD) simulations[126, 127] demonstrated that the size nonuniformity and the different orientations of the constituent grains in nanocrystalline metals induced complex stress state in the grain interior under uniaxial tension, facilitating the operation of different twinning systems and the consequent formation of FFT. Given that the FFT observed in the prior studies were often related to the complex GB structures of the deformed nanocrystalline metals and the complex stress states under extreme loading modes[109, 125, 126, 131], it naturally raises the question of whether FFT could be formed in a single crystal under simple loading modes, such as uniaxial tension and bending. In addition, all the previous studies focused on investigating the mechanisms of FFT formation. The dynamic process of FFT dissolution and their atomic-scale mechanisms remains unexplored, due to the significant experimental challenge.

Here, gold (Au) nanocrystals are used as the model system to investigate the atomic-scale formation process of FFT via conducting *in situ* nanomechanical tests under high resolution transmission electron microscopy (HRTEM) combined with atomistic simulations. The results demonstrate that sequential twinning on several slip systems and the decomposition of grain boundary (GB) at the node of a multifold twin play a critical role in FFT formation in the Au single crystal under bending and the reversible formation and dissolution of FFT in the Au nanocrystal with preexisting twin under tension and shearing. Moreover, the complex stress state in the neck area results in FFT formation in a gold nanocrystal with a twin boundary parallel to the loading direction, different from the prediction of Schmid law. These findings provide deep insights into FFT formation under mechanical loading, which are of importance for microstructure control to improve the mechanical properties of metal materials.

5.2 Experimental Procedures

The Au nanocrystals with different microstructural features were fabricated using *in situ* nanowelding, as described in Chapter 3.1.2. *In situ* compression tests at room temperature were conducted inside a FEI Titan TEM equipped with a Nanofactory STM holder. The strain rates of 10^{-3} s^{-1} during tensile tests were controlled by the movement speed of the W nanoprobe on the piezo-controller side. *In situ* bending and shear tests were conducted via controlling the leftward/rightward movement of W nanoprobe at a constant rate of ~0.01 nm/s^{-1}. Moreover, all the tests were operated at 200 kV with low dose conditions (electron beam intensity < $10^5 A \cdot m^{-2}$) in a short time (less than 3 min) to minimize the potential beam effects on the deformation behavior of metallic nanocrystal[220, 221]. MD simulations were further conducted to reveal the atomic-scale mechanism of FFT formation in Au nanocrystals under different loading modes. MD simulation method can be found in Chapter 3.3.

5.3 Experimental Results

5.3.1 FFT Formation In A Nanoscale Au Single Crystal Upon Bending

Figure 5.1 shows the atomic-scale process of FFT formation in a single-crystalline Au nanocrystal during bending. The nanoscale Au single crystal is prepared inside TEM by nanowelding. As shown in Figure 5.1a, the nanocrystal is loaded along [111] direction with a displacement rate of ~10^{-2} nm/s and viewed along [$\bar{1}$10] zone axis, which allows direct observation of perfect and partial dislocations. Prior to *in situ* bending test, the as-fabricated Au nanocrystal

has negligible strain (Figure 5.2a and 5.2c). Upon bending, the maximum tensile and compressive strains in the nanocrystal before yielding are up to ~4% (Figure 5.2b and 5.2d), which are comparable to the elastic strain limit of 2.1%–5.3% for Au nanocrystal[170]. Further bending deformation gives rise to surface nucleation and glide of partial dislocations on the (111) and $(\bar{1}\bar{1}1)$ slip planes, leaving behind stacking faults (SFs), as marked with the red arrows in Figures 5.1b-c and Figures 5.3a-b. Some of the partial dislocations are found to meet at the center of the nanocrystal where the lengthwise stress is zero. The nucleation of additional partial dislocations, primarily on $(\bar{1}\bar{1}1)$, leads to the formation of a low angle GB[252] (the dashed line in Figure 5.1c). With further bending, partial dislocation activities on the other slip planes occur (Figures 5.1d-e and Figure 5.3c). The GB angle also increases from 12° to 16°, a direct result of the lattice reorientation caused by partial dislocation slip[130]. As the bending deformation increases, additional partial dislocations nucleate between the SFs, producing a fourfold twin (the red lines in Figures 5.1f-h and Figure 5.3d)[109] and a 20° GB (Figure 5.1h). Subsequently, the GB reorganizes itself into a coherent TB by absorbing and emitting partial dislocations, and the TBs migrate, reducing the high elastic energy associated with the incompatibility of the separated TBs in the newly formed FFT (Figure 5.1i and Figure 5.3e-g)[124]. Different from the experimental observation of FFT formation in nanoscale Au single crystal under bending, the formation of single deformation twin and the occurrence of perfect dislocation slip were often observed in the single-crystalline Au and Ag nanowires under <110> uniaxial tensile loading[113, 114, 152]. Such different twinning behavior is attributed to the complex stress state induced by bending (Figure 5.2b and 5.2d), which favors the operation of different twinning systems.

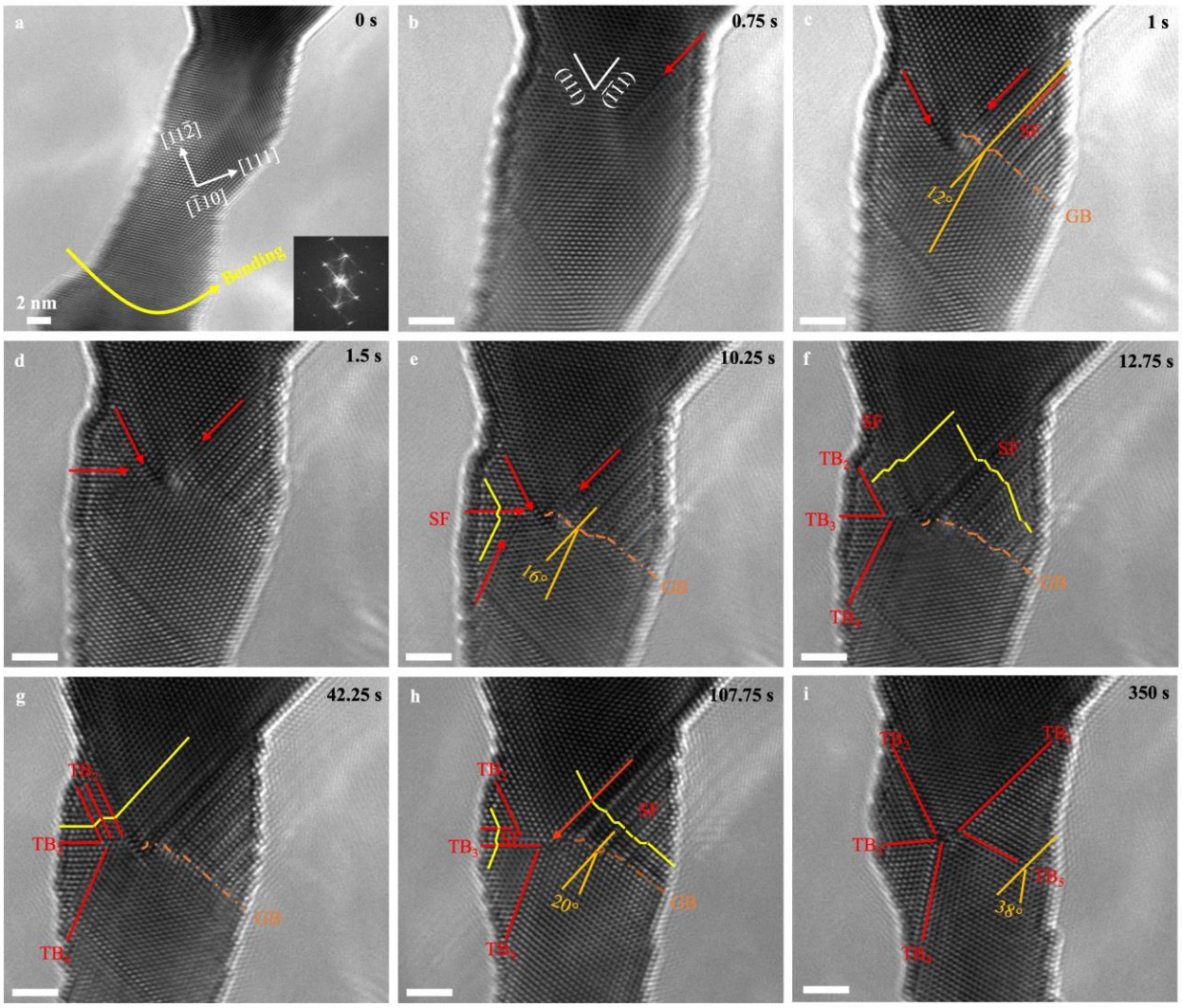

Figure 5.1 Bending-induced formation of fivefold twin in a single-crystalline Au nanocrystal. (a) TEM image of a single-crystalline Au nanocrystal prepared via *in situ* nanowelding. (b-e) Successive emission of partial dislocations on four different twinning systems in the Au nanocrystal. A 12° grain boundary forms in the Au nanocrystal, and the GB angle increases from 12° to 16° upon bending, mediated by partial dislocation slip. (f) Transformation of the stacking fault bundles into the twin variants of the threefold twin. (g) Twin boundary migration mediated by partial dislocation slip. (h) Formation of a fourfold twin with a 20° grain boundary at the central node. (i) Formation of a fivefold twin through lattice reorientation. All the scale bars are 2 nm.

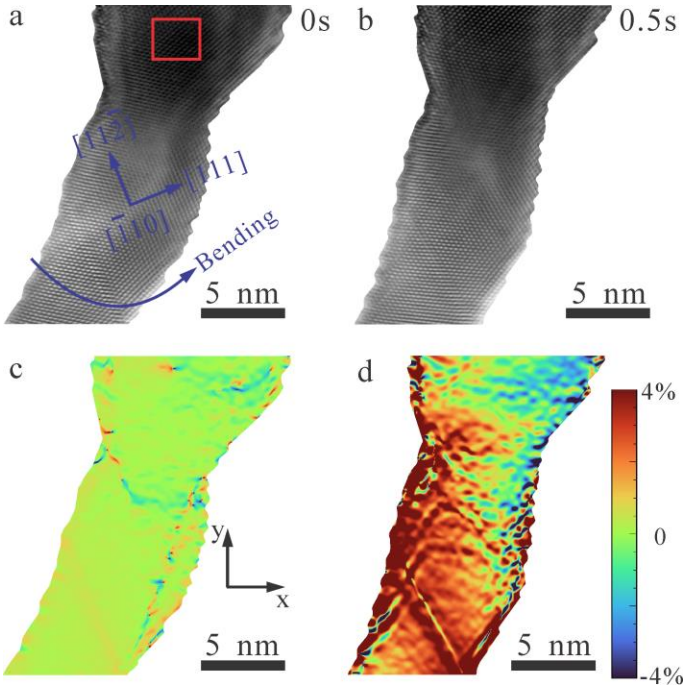

Figure 5.2 Strain analysis on the Au nanocrystal during bending. (a-b) TEM images of the Au nanocrystal before (a) and after (b) bending deformation. (c-d) Quantitative strain mappings of the Au nanocrystal before (c) and after (d) bending deformation, by geometrical phase analysis. The unstrained lattice in the red framed region in (a) serves as a reference for the geometrical phase analysis (see ref.[253] for more details). The color variation from dark blue to dark red indicates the variation of stain values from -4% to 4%.

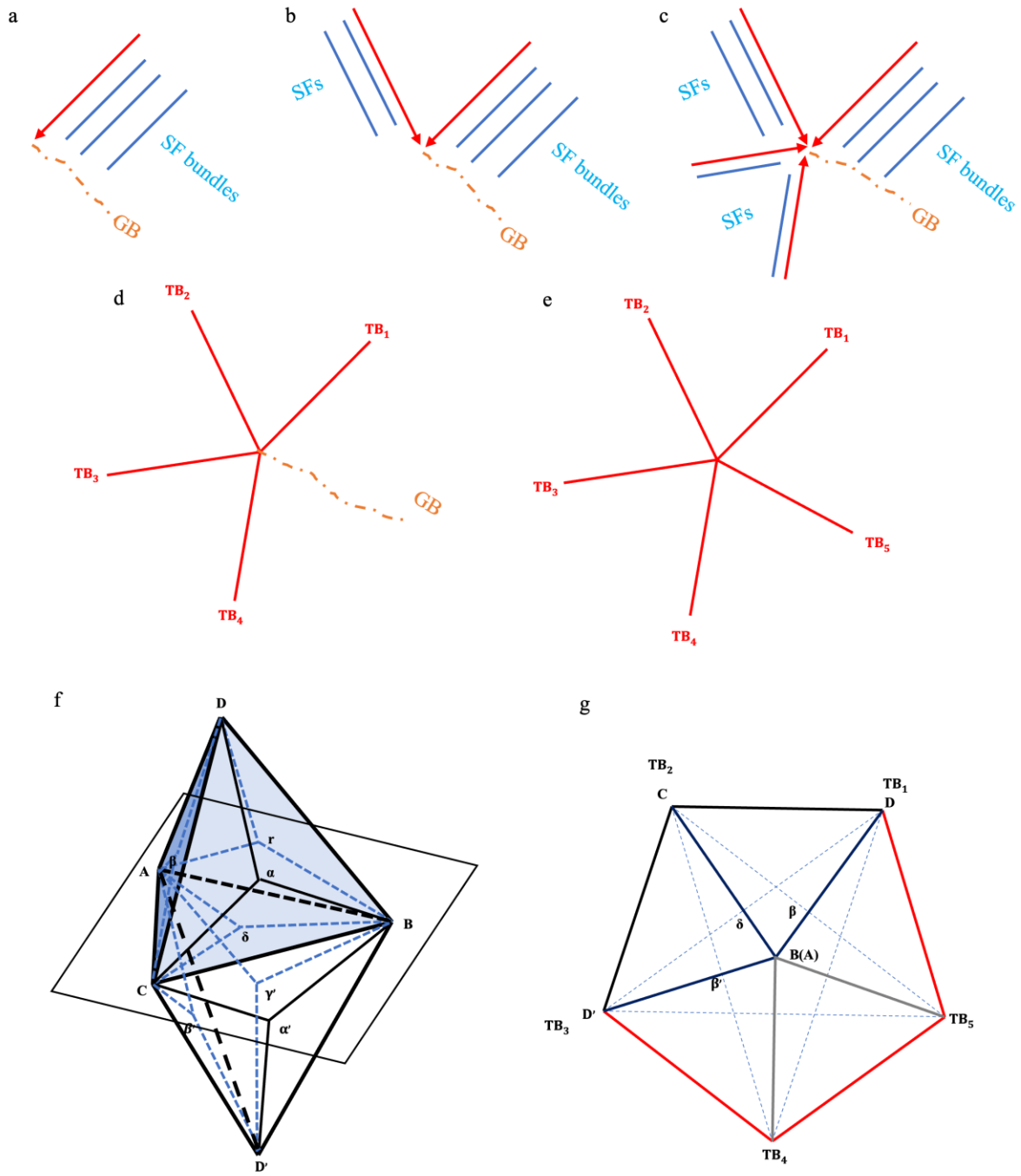

Figure 5.3 Schematics showing bending-induced fivefold twin formation in a single-crystalline Au nanocrystal. (a-c) Successive emission of partial dislocations on four different twinning systems upon bending, resulting in the formation of stacking fault bundles and a grain boundary (GB). (d) Fourfold twin with a GB at the central node. (e) Transformation from GB into twin boundary resulting in the formation of a fivefold twin. (f-g) Thompson tetrahedrons used for illustrating the newly formed fivefold twin.

To understand the atomic-scale formation process of FFT under bending, MD simulations of nanoscale Au single crystal were performed (Figure 5.4). The applied bending force on the nanocrystal is along [110]-direction (CD' in Figure 5.3f-g). The bending deformation induces compressive and tensile stress at the two opposite sides of the Au nanocrystal, respectively (Figure 5.5a). Given that the leading partial has a higher Schmid factor when <001>-oriented nanocrystal is under compression rather than tension, partial dislocation slip is favored in the compressive side of the nanocrystal[48, 254]. Under the compressive stress of ~8.6 GPa, plenty of partial dislocations are observed to nucleate from the compressive side of the free surface, glide on the $(1\bar{1}\bar{1})$ planes, and then terminate around the neutral plane with zero lengthwise stress (Figure 5.5b), resulting in the formation of a TB (T1 in Figure 5.4b and ABD in Figure 5.3f-g) and a GB (Figure 5.4a-b). Meanwhile, a severely distorted area, comprised of the atomic columns colored in grey and red in Figure 5.4b, forms at the tensile side of the nanocrystal to accommodate the imposed bending deformation (Figure 5.5b). With increasing strain, a part of the high-energy distorted area under the tensile stress of ~5.9 GPa (Figure 5.5b-c) relaxes into a twin with TB on $(\bar{1}\bar{1}1)$ plane (T3 in Figure 5.4c and ABD' in Figure 5.3f-g) through atom readjustment, lowering the overall system energy[122]. The unrelaxed region of the disordered area is indicated by the grey and red atomic columns in Figure 5.4c. Subsequently, the GB evolves into a TB on (111) plane (T2 in Figure 5.4d and ABC in Figure 5.3f-g), due to lattice reorientation mediated by partial dislocation emission and absorption at the GB with the local stress as high as ~8.6 GPa (Figure 5.5b-d). Accompanied with the formation of a threefold twin, a Σ27 GB appears at the node of the newly formed threefold twin, and subsequently it decomposes into two TBs during further deformation[246] (T4 and T5 in Figure 5.4e-f and Figure 5.5e-f), leading to FFT formation (Figure 5.3f-g).

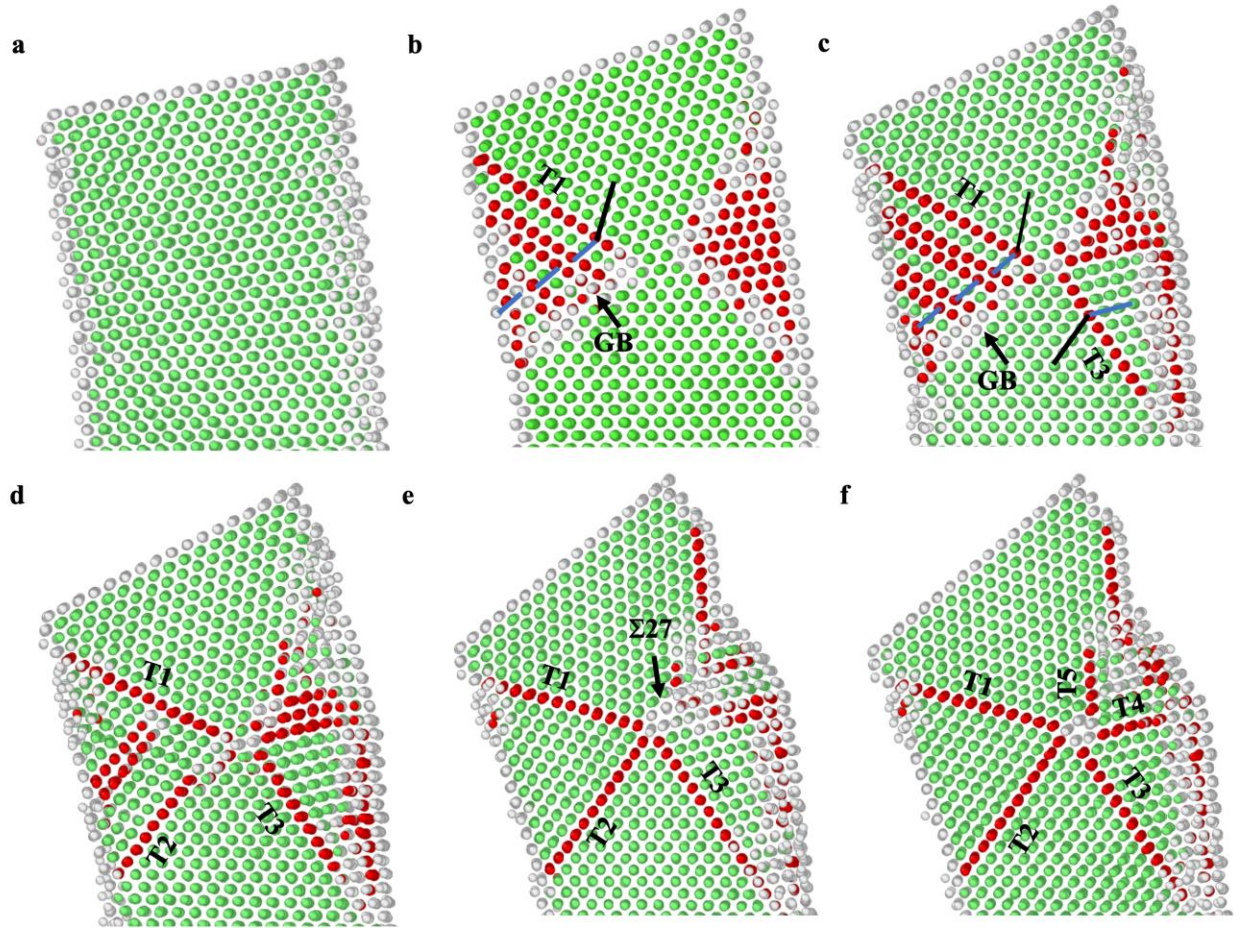

Figure 5.4 MD simulation showing the atomic-scale process of fivefold twin formation in a single-crystalline Au nanocrystal upon bending. (a) The bending Au nanocrystal before defect nucleation. (b) Successive partial dislocations emit from the free surface and then terminate near the neutral plane, resulting in the formation of a twin boundary (TB) and a grain boundary (GB). (c) Transformation of a distorted area into a twin via atom adjustment. (d) Formation of threefold twin through partial-dislocation-slip-mediated lattice reorientation. (e) Formation of a Σ27 GB at the node of the threefold twin. (f) Formation of two TBs caused by the decomposition of Σ27 GB resulting in the formation of fivefold twin. Based on common nerighbor analysis[208], the atoms with face centered cubic (FCC), hexagonal close packed (HCP) and other structures are colored in green, red and grey, respectively.

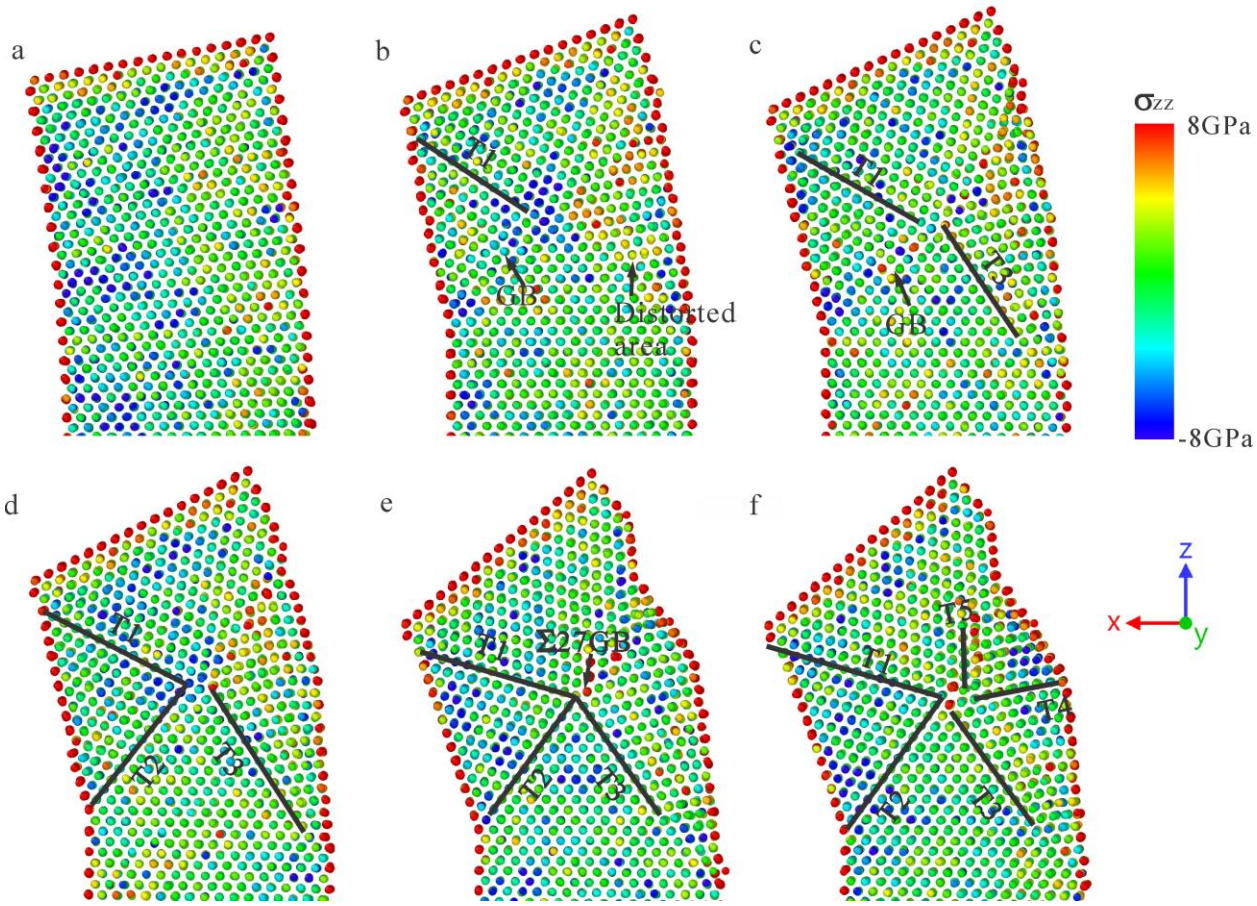

Figure 5.5 Quantitative stress mappings of the nanoscale Au single crystal under bending in MD simulation. (a) Au nanocrystal before defect nucleation. The high compressive stress of ~ 8.6 GPa appears near free surface. (b) Formation of a TB and a GB caused by partial dislocation slip. Meanwhile, a distorted area forms in the area under the tensile stress of ~4.9 GPa. (c) Transformation of the distorted area into a twin via atom adjustment. (d) Formation of threefold twin by absorbing and emitting partial dislocations at GB under the compressive stress of ~6.6 GPa. (e) Formation of a Σ27 GB at the node of the threefold twin. (f) Formation of two TBs caused by the decomposition of Σ27 GB under the tensile stress of ~9.8 GPa. The color variation from blue to red corresponds to the stress from -8 GPa to 8 GPa.

The different pathways for FFT formation in the experimental and computational results are probably related to the surface conditions of the Au nanocrystals. The nanoscale Au single crystal in the experiment is fabricated via *in situ* nanowelding, probably introducing some mass-deficient defects at the surface of the "pristine" nanocrystal, which are preferential dislocation nucleation sites[42, 53]. Moreover, the diameter of the as-fabricated Au nanocrystal is not as uniform as that in the MD simulations. Numerous atomic-scale steps exist at the free surface of the Au nanocrystal. Upon mechanical loading, stress concentration could appear at the surface step, facilitating dislocation slip[58, 96]. By contrast, the surface of the Au nanocrystal in MD simulations is atomically flat. Hence, partial dislocation slip is prone to be activated during *in situ* bending tests, compared to that in MD simulations. Despite the different surface conditions and the orders of magnitude difference in loading rate and timescale between MD simulations and experiments, both the experimental and computational results show that fivefold twin could form in the nanoscale Au single crystal under bending, which is energetically favorable.

5.3.2 Formation And Annihilation Of FFT In A Au Nanocrystal With A Multifold Twin Under Shearing And Tension

Not in the single-crystalline Au nanocrystal under uniaxial tension[96, 113, 114], but in the Au nanocrystal with a preexisting twin under shearing and tension, FFT is observed to form (Figure 5.6). As shown in Figure 5.6a, a Au nanocrystal with a fourfold twin is subjected to shear loading along the [111]-direction at room temperature and a strain rate of 10^{-3} s^{-1}. Upon shear loading, partial dislocations sequentially glide along the preexisting SF and then are absorbed into the TB (TB_4 in Figure 5.6a), resulting in the nucleation and growth of a deformation twin in domain III and the generation of a FFT (Figure 5.6a-b). The absorption of partial dislocations into TB_4 results

in the emission of partial dislocations from TB_4 into domain IV, leading to the migration of TB (TB_6 in Figure 5.6a-b) and the consequent extension of domain IV (Figure 5.6a-b). When the shearing direction is reversed, detwinning occurs in domains III and IV through the successive slip of partial dislocations along the TBs (TB_3 and TB_6 in Figure 5.6c-g) in the opposite direction. Consequently, four TBs, i.e., TB_3, TB_4, TB_5 and TB_6, annihilate, producing an Σ9 asymmetric tilt GB that extends from the node of the V-shaped twin to the nanocrystal surface (Figure 5.6g). The FFT is transformed into a triple junction of a V-shaped twin and a Σ9 GB. The formation and dissolution of FFT can be controlled by applying and removing shear, or equivalently reversing the shear direction.

The as-formed triple junction can be transformed back into a FFT under tensile loading along [110]-direction at room temperature and a strain rate of 10^{-3} s^{-1} (Figure 5.6h-j). Given that the calculated Young's modulus for the <110>-oriented Au nanocrystal is 81.5 GPa (see Appendix A) and the lattice strain in the Au nanocrystal upon tension is measured to be 2.08% via comparing the change in (110) interplanar spacing[28, 42, 145] (Figure 5.7), the tensile stress in the Au nanocrystal is estimated to be 1.7 GPa. Considering that the largest Schmid factor for leading partial dislocations in Au nanocrystal under <110> tension is 0.47, the resolved shear stress on <112>{111} slip system is 0.8 GPa, which is comparable to the shear stress of 0.47GPa required for partial dislocation nucleation in Au nanowire[58]. Partial dislocation slip could be activated in the Au nanocrystal upon tensile deformation. As shown in Figure 5.6i, the surface nucleation and glide of a partial dislocation generates a SF in the Au nanocrystal. Subsequently, the consecutive slip of twinning partials nearby the SF results in twin formation in domain IV (Figure 5.6j). Concurrently, the Σ9 GB decomposes into two TBs[255] (TB_3 and TB_4 in Figure 5.6j), transforming

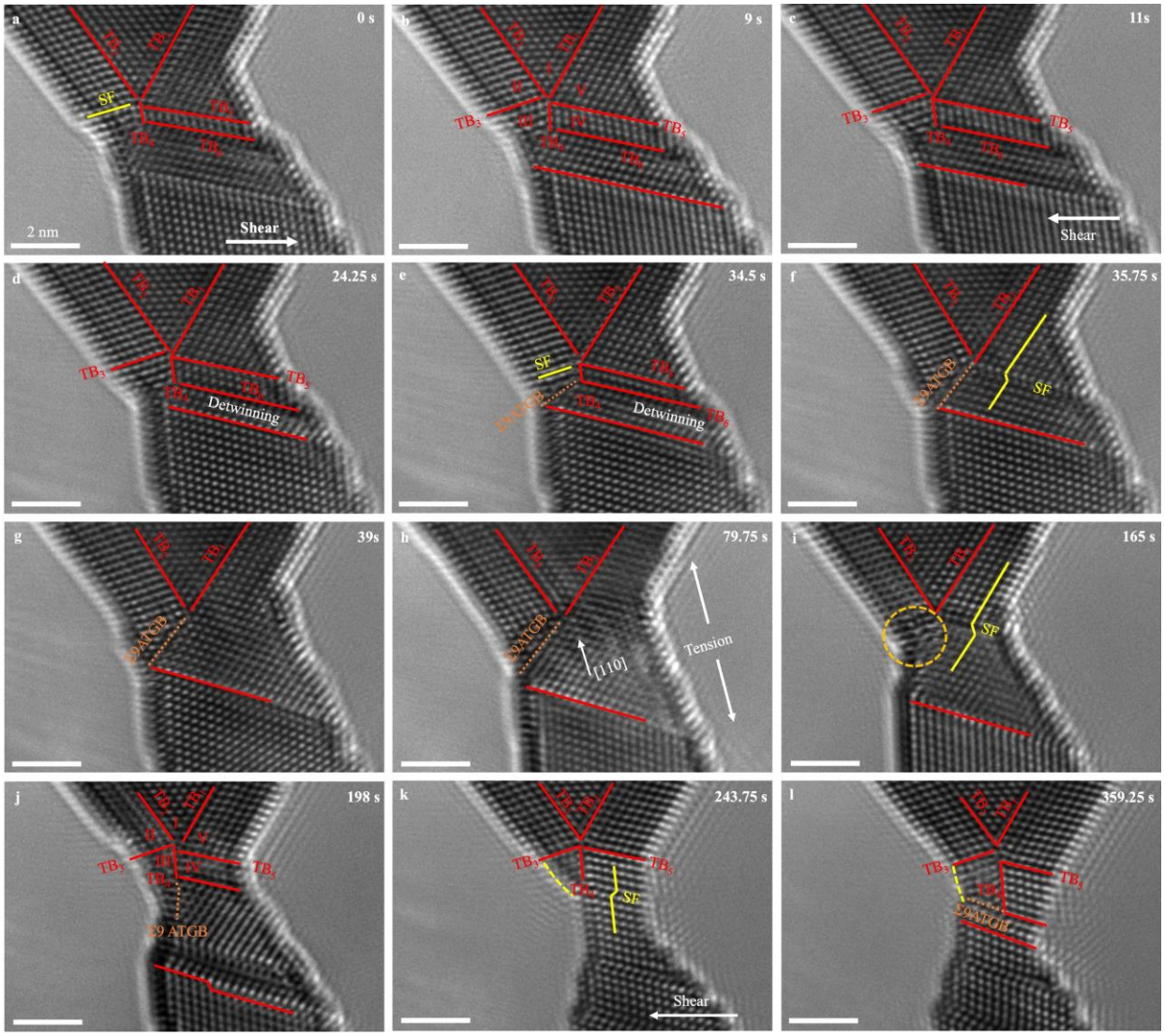

Figure 5.6 Shear- and tension-induced formation and dissolution of fivefold twin in a multifold twinned nanocrystal at room temperature. (a) An as-fabricated Au nanocrystal with a fourfold twinned structure. The nanocrystal is viewed along [$\bar{1}$10]. (b) Formation of fivefold twin via successive twinning partial slip along the preexisting stacking fault and the TB under shearing. (c-g) Detwinning of the fivefold twin into a V-shaped twin upon reversed shear loading. A twofold twin and a Σ9 GB form after the detwinning process. (h-j) Formation of fivefold twin through partial dislocation slipping and Σ9 GB decomposition under tensile loading at the strain rate of 10^{-3} s^{-1}. (k, l) The change in the twin morphology of the fivefold twin upon shear loading. All the scale bars are 2 nm.

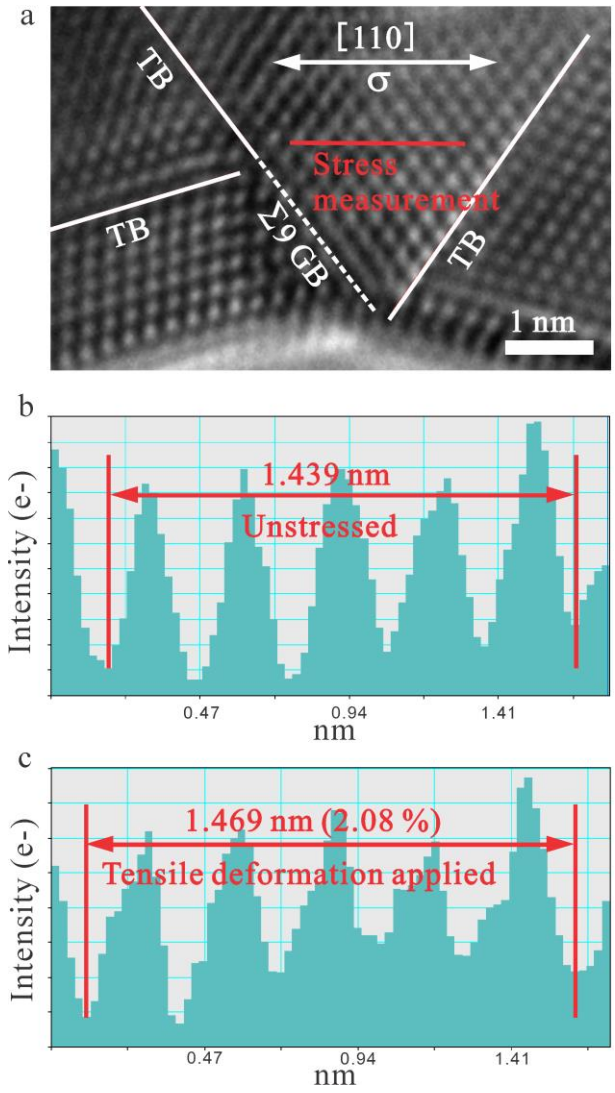

Figure 5.7 Lattice stress measurement in a Au nanocrystal during tensile test. (a) TEM image of the Au nanocrystal with a triple junction of a Σ9 GB and a TB under [110] tensile loading at room temperature and a strain rate of 10^{-3} s^{-1}. (b-c) The intensity profile of the atomic columns along the loading direction. The 5-planes measurements of the lattice spacing along [110] loading direction are (b) 1.439 nm in the unstressed nanocrystal and (c) 1.469 nm in the deformed nanocrystal. Lattice strain of 2.08% is obtained by comparing the change in the (110) interplanar spacing.

the V-shaped twin-triple junction back into a FFT. During the whole process of FFT formation and dissolution, the morphology of the V-shaped twin, composed of TB_1 and TB_2, remains unchanged, indicating that there is no interaction between dislocations and these two TBs. The twin morphology of the newly formed FFT could be further altered via partial dislocation slip along TB_3 and TB_5 and dislocation transmission through TB_4 under shear deformation[256], as shown in Figure 5.6k-l. Hence, the formation, dissolution and even morphology of FFT could be controlled through partial dislocation slip along the TBs and the decomposition and generation of GBs. To demonstrate the universality of the FFT formation mechanism discovered above, *in situ* tensile test of a Au nanocrystal with a preexisting twofold twin is performed along [112]-direction at room temperature under a strain rate of 10^{-3} s^{-1} (Figure 5.8). Under tensile loading, the decomposition of Σ9 GB and a series of twinning dislocation slip at the node of the twofold twin result in FFT formation.

To further understand the critical role of GB decomposition in the process of FFT formation, atomistic simulations of a Au nanocrystal with a triple junction of a Σ9 {001}/{112} asymmetric tilt GB and a TB were conducted. When the Au nanocrystal is compressed along [001]-direction, the segments of the Σ9 GB above and below the TB dissociate into four TBs (Figure 5.9a-b). As the deformation proceeds, the emission of partial dislocations from the Σ9 GB and free surfaces is observed, resulting in the migration of the newly formed TBs and the consequent formation of FFT (Figure 5.9c-d). With further deformation, the newly formed FFT rearranges itself through partial dislocation slip, reducing the overall system energy (Figure 5.9d-f). Similar process of FFT formation, mediated by GB decomposition and partial dislocation slip, is also found in a Au nanocrystal with a Σ9 {111}/{115} asymmetric tilt GB during compression (Figure 5.10). Moreover, the MD simulations reveal that there are two pathways for Σ9 GB decomposition.

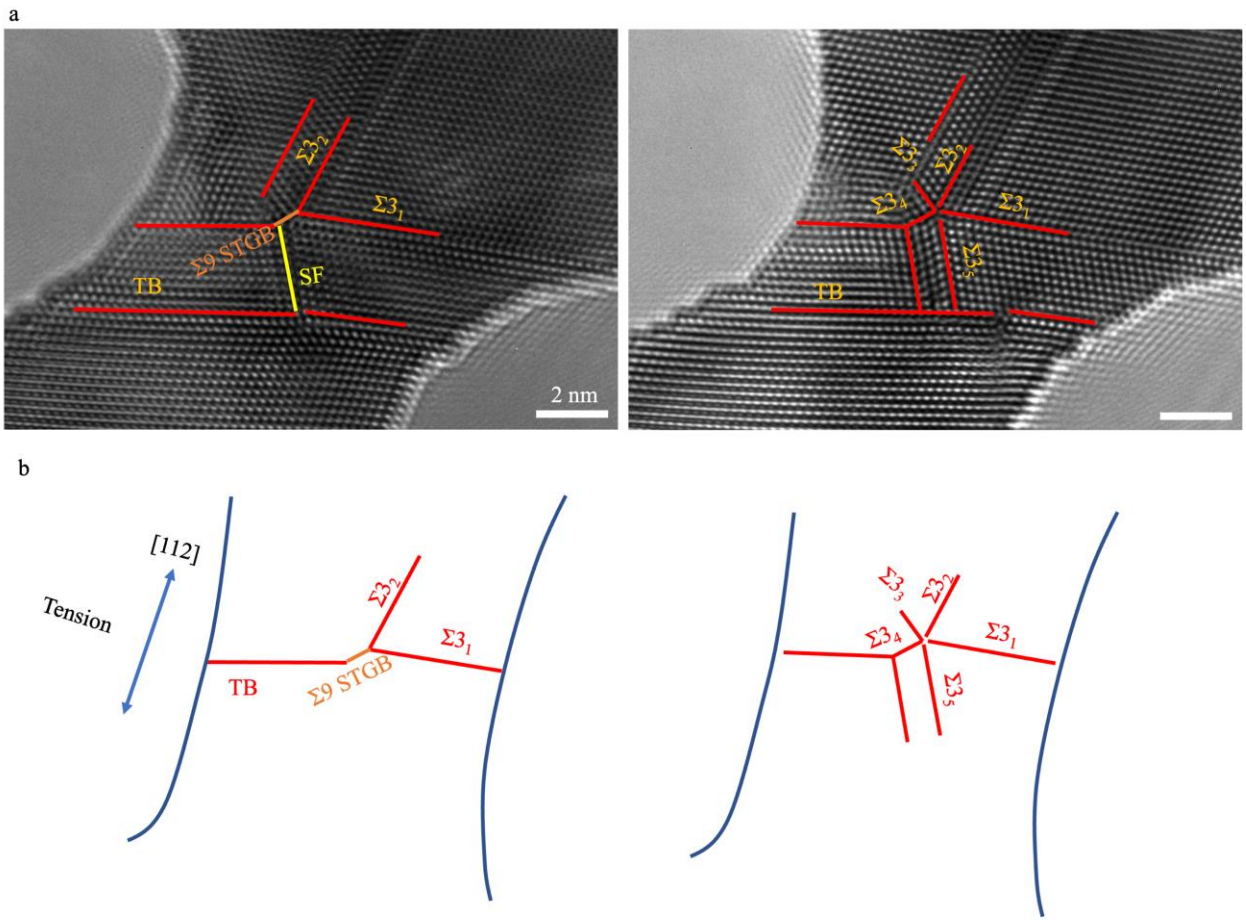

Figure 5.8 Fivefold twin formation in a Au nanocrystal with a twofold twin under <112> tensile loading at room temperature under a strain rate of 10^{-3} s^{-1}. (a) Decomposition of Σ9 GB and partial dislocation slipping resulting in the formation of a fivefold twin. All the scale bars are 2 nm. (b) Schematics showing the formation of fivefold twin resulting from Σ9 GB decomposition and partial dislocation slipping.

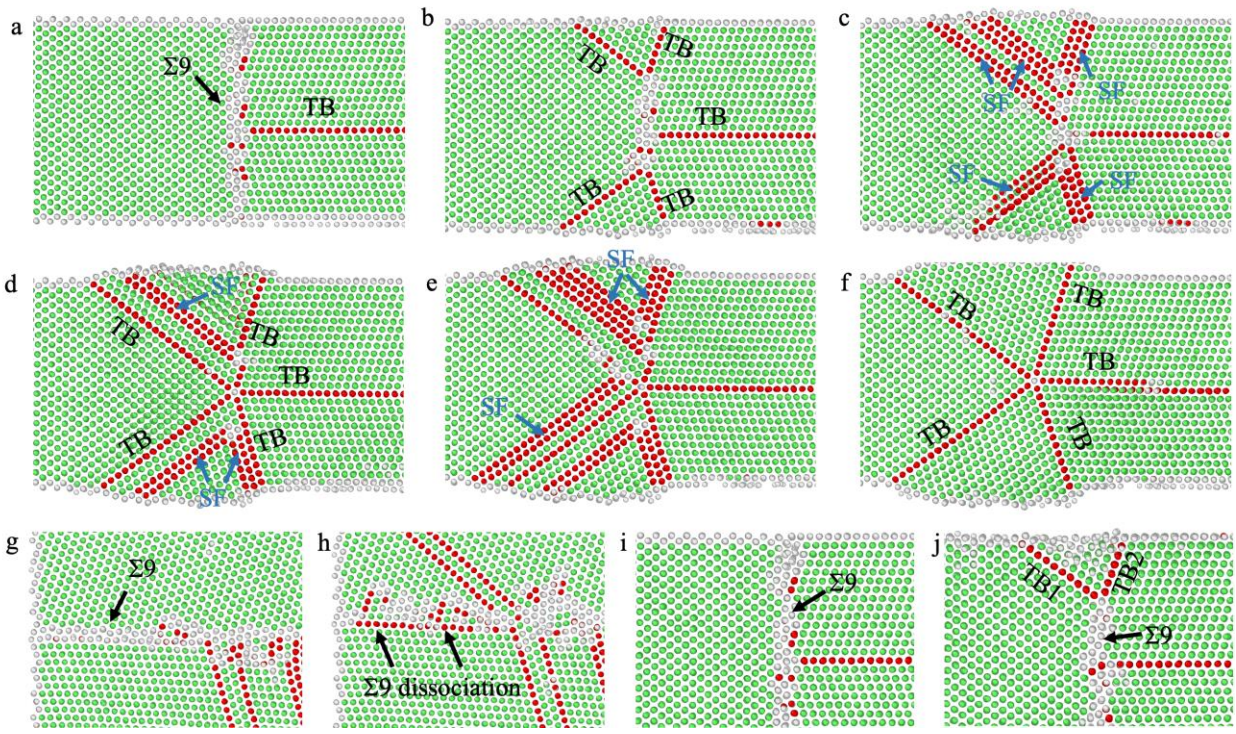

Figure 5.9 MD simulations showing atomic-scale processes of fivefold twin formation in the Au nanocrystal and the decomposition of Σ9 asymmetric tilt GB. (a) A Au nanocrystal with a TB intersected with a Σ9 {001}/{112} asymmetric tilt GB under <112> compression. (b) Formation of four TBs via Σ9 GB decomposition upon compression. (c-f) Adjustment of the fivefold twin via a series of partial dislocation slip from the free surface and the Σ9 GBs. (g-j) Atomic-scale processes of the decomposition of Σ9 {111}/{115} (g,h) and Σ9 {001}/{112} (i,j) asymmetrical tilt GBs. Based on common nerighbor analysis[208], the atoms with FCC, HCP and other structures are colored in green, red and grey, respectively.

At the Σ9 {111}/{115} asymmetric tilt GB, the two dissociated TBs are parallel and inclined to the initial Σ9 GB (Figure 5.9g-h), while at the Σ9 {001}/{112} asymmetric tilt GB, the two dissociated TBs are both inclined to the initial Σ9 GB (Figure 5.9i-j).

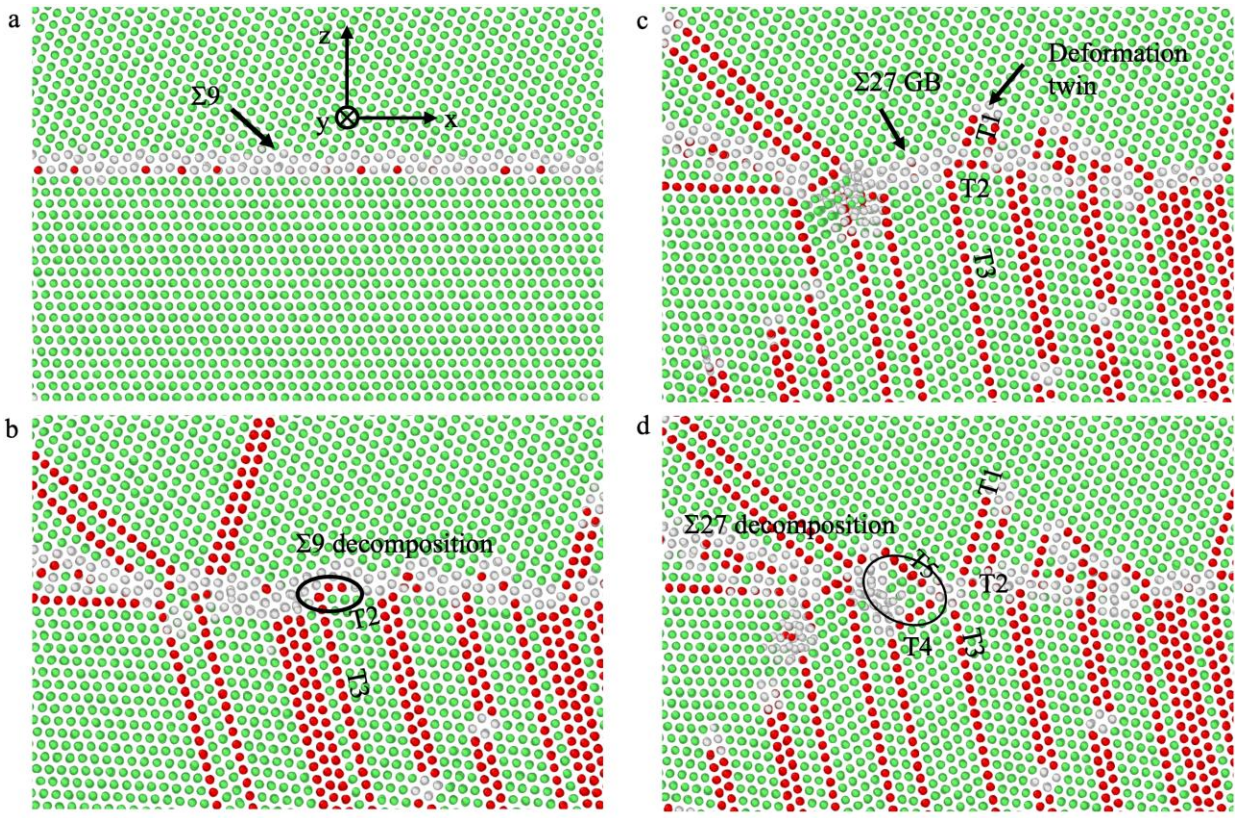

Figure 5.10 MD simulation showing fivefold twin formation in a Au bicrystal. (a) A pristine Au nanocrystal with a Σ9 {111}/{115} asymmetric tilt GB. (b) Formation of two TBs through Σ9 GB decomposition. (c) Partial dislocation slip at GB causing the formation of a threefold twin and a Σ27 GB. (f) Σ27 GB decomposition at the node of the threefold twin, resulting in the formation of fivefold twin. The five TBs are indicated as T1, T2, T3, T4 and T5, respectively.

5.3.3 FFT Formation In A Bi-Twinned Au Nanocrystal Under Tension

Figure 5.11a-b show the atomically resolved process of FFT formation in the Au nanocrystal with a TB parallel to the $[11\bar{2}]$ loading direction under the strain rate of 10^{-3} s^{-1}. A neck exists in the bi-twinned Au nanocrystal, as shown in Figure 5.11a. After tensile failure, a FFT is observed to form in the fractured Au nanocrystal (Figure 5.11b), which is reproduceable in a different but similarly bi-twinned Au nanocrystal (Figure 5.12). The formation of this kind of FFT took place too rapidly that its evolution was not recorded in the experiments. Thus, to further understand the formation mechanisms of the FFT, atomistic simulations of bi-twinned Au nanocrystal were performed to model this process (Figure 5.11c-f). The bi-twinned nanowires are constructed along the <112>-direction and deformed at room temperature under a strain rate of 10^{8} s^{-1}. Upon tensile loading, perfect dislocation slip on the inclined $(1\bar{1}1)$ and $(\bar{1}11)$ planes dominates the plastic deformation (Figure 5.11c), which can be well explained by the quantitative analysis on the Schmid factors for the perfect and partial dislocation slip on {111} planes. The Schmid factors for perfect dislocation slip $([01\bar{1}](\bar{1}11)$ and $[10\bar{1}](1\bar{1}1))$ are 0.408, which are larger than those of 0.393 for partial dislocation slip $([12\bar{1}](\bar{1}11)$ and $[21\bar{1}](1\bar{1}1))$. Upon initiation of plastic deformation, a large number of perfect dislocations nucleate in a localized region, resulting in the formation of a neck in the nanocrystal (Figure 5.11d). During further loading, partial dislocation slip on $(\bar{1}\bar{1}1)$ plane is observed, resulting in the nucleation and growth of deformation twins and the ultimate formation of a FFT (Figure 5e-f). Notably, the twinning elements of the formed FFT in the bi-twinned Au nanocrystal are the $[11\bar{2}](111)$ type, the activation of which leads to the contraction rather than the elongation of the Au nanocrystal. Moreover, the Schmid factor for $1/6[\bar{1}\bar{1}\bar{2}]$ partial dislocation slip on $(\bar{1}\bar{1}1)$ plane in the $[11\bar{2}]$-oriented nanocrystal under tension

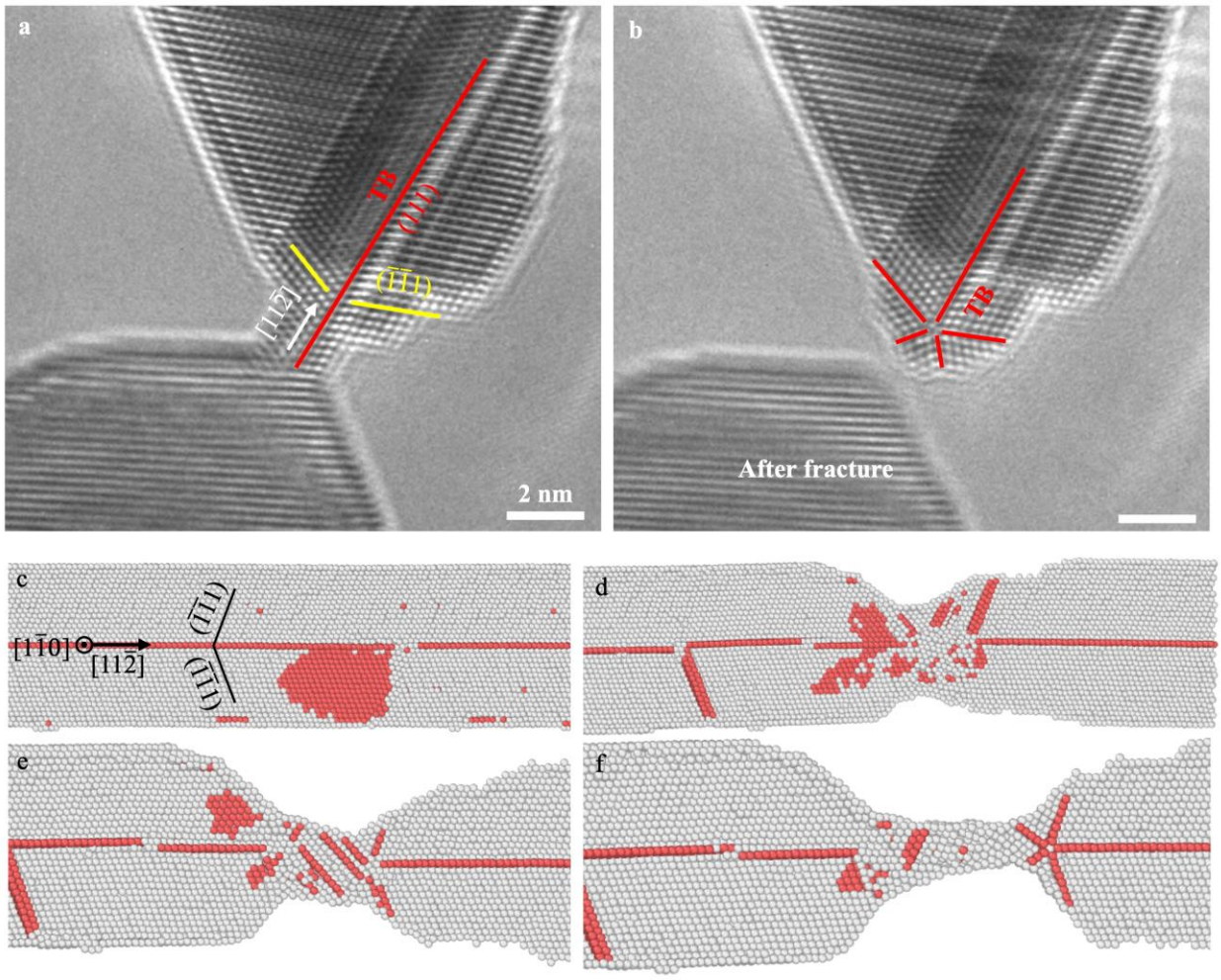

Figure 5.11 Fivefold twin formation in the neck area of a Au nanocrystal with a TB parallel to the tensile loading direction. (a-b) *In situ* atomic-scale observation of fivefold twin formation in the neck area of the Au nanocrystal loaded along <112>-direction at room temperature under a strain rate of 10^{-3} s^{-1}. All the scale bars are 2 nm. (c) MD snapshot showing dislocation slip on inclined {111} planes. Based on common nerighbor analysis[208], the atoms with HCP structure are colored in red, and the atoms with other structures are colored in grey. (d) Formation of a neck in the bi-twinned Au nanocrystal at the final stage of tensile test. (e-f) A series of MD snapshots showing fivefold twin formation in the neck area.

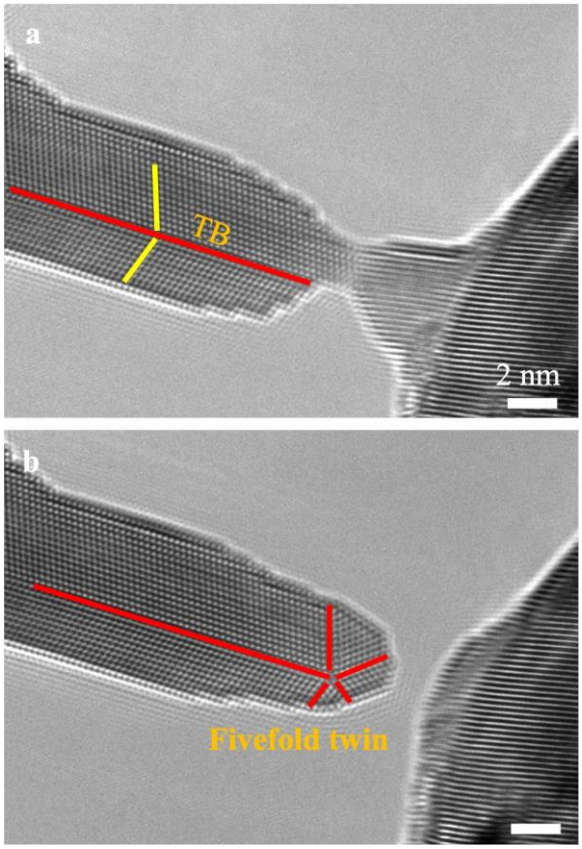

Figure 5.12 Fivefold twin formation in the Au nanotip after the tensile failure of a bi-twinned Au nanocrystal. All the scale bars are 2 nm.

is -0.314. Hence, perfect and partial dislocation slip on the inclined $(1\bar{1}1)$ and $(\bar{1}11)$ slip planes are favored over partial dislocation slip that would lead to FFT formation. This indicates that the formation of FFT in the bi-twinned Au nanocrystal is specific to the deformation in the neck region. No similar behavior is observed in the experiments or simulations outside of this neck region. Consequently, it is concluded that the complex stress state in the neck and the need for material reorientation in this region favor the FFT formation in the neck area just prior to tensile failure.

5.4 Discussion

Distinct from FFT formation in nanocrystalline metals under extreme loading conditions (ball milling and high-pressure torsion)[109, 123, 125], this work reveals that FFT could be formed in a single-crystalline Au under bending, which is attributed to the following reasons. First, localized stress concentration exists near surface steps in the nanoscale Au single crystal upon mechanical loading, favoring surface nucleation and glide of partial dislocations on <112>{111} slip system[58]. The emission of partial dislocations from the preferential surface sites on non-neighboring {111} planes results in the nucleation and growth of deformation twins unfollowing the traditional layer-by-layer fashion[95, 120]. Different from the *in situ* bending tests, the high strain rate employed in the atomistic simulations accounts for the untraditional twinning route during the process of FFT formation. Second, bending deformation induces lattice rotation and complex stress state in the sample (Figure 5.2d and Figure 5.5a), which favors the activation of partial dislocation slip in varying slip systems[102, 109, 123, 125] causing FFT formation in a single-crystalline metal. For the Au nanocrystals with preexisting defects (TBs and GBs) under uniaxial tension or simple shearing, the different orientations of the constituent crystal lattice induce complex stress state, facilitating the operation of different twinning systems and thus causing the formation of FFT.

In addition to partial dislocation slip, GB decomposition also plays a critical role in FFT formation. Partial dislocation slip in different slip systems usually causes the formation of twofold and threefold twins in the nanostructured metals[52, 257]. Geometrically necessary GBs, that is Σ9 GB with the GB energy of ~542 mJ/m^2 [257] and Σ27 GB with the GB energy of ~560 mJ/m^2 [257], subsequently generate at the node of the two- and three-order twins, respectively, which lead to a substantial increase in excessive elastic strain energy. From the point view of thermodynamics, the

high-energy Σ9 and Σ27 GBs are prone to decompose into two Σ3 GBs (coherent TB) with relatively low energy (~17.5 mJ/m^2 [258]), reducing the overall system energy[257]. A threefold twin could directly develop into a FFT through Σ27 GB decomposition, while partial dislocation slipping is needed to be activated to cooperate with Σ9 GB decomposition causing the transition from a twofold twin into a FFT. The experimental observations of transformation from two- and three-order twins to a FFT in this study are energetically favorable[259].

The findings in this study reveal the pathways for FFT formation in the Au nanocrystals with different microstructural features. Given that introducing FFT into nanostructured metals greatly improved their mechanical properties[165, 166, 167], deep insights into the atomic-scale formation processes of FFT are of vital importance for providing new clues to design high-performance metal materials. Considering that previous studies mostly focused on the mechanical behaviors of the chemically synthesized metallic nanowires with the common <110> axis of fivefold twin parallel to the loading direction[171, 193, 198, 249, 260], the approaches for mechanically introducing FFT into the nanoscale Au, reported in this study, provide an opportunity to investigate the intrinsic deformation features of FFT.

5.5 Conclusion

In conclusion, combined *in situ* TEM experiments and atomistic simulations reveal that partial dislocation slip in varying slip systems and the decomposition of high-energy grain boundary are responsible for the formation of fivefold twin in the nanoscale Au single crystal under bending and the reversible formation and dissolution of fivefold twin in the Au nanocrystals with preexisting twin under shearing and tension. Moreover, the complex stress state in the neck

area leads to fivefold twin formation in a bi-twinned Au nanocrystal, disobeying Schmid law. This work provides atomistic insights into the formation process of fivefold twin in single crystal metal under mechanical loading, which paves the road for rationally manipulating microstructure features to fabricate high-performance nanostructured metals.

6.0 Atomistic Processes Of High-Temperature Plastic Deformation Of Nanoscale Body-Centered Cubic Tungsten

In this chapter, the high-temperature mechanical behaviors of tungsten nanocrystals will be investigated at the atomic scale. Much scientific and practical interest is currently focused on the atomic-scale mechanical behaviors of metallic nanocrystals with different crystal structures at room temperature, while the high-temperature plastic deformation in tungsten nanocrystals remains not well understood, due to the technical difficulty in elevating the experimental temperature during *in situ* mechanical tests in an extremely small chamber of transmission electron microscopes. In this study, a *in situ* high-temperature nanomechanical testing method is developed based on electric-current-induced Joule heating in the metallic nanocrystal. By this method, it is found that three distinct deformation modes, that is deformation twinning, body-centered-cubic-face-centered-cubic-body-centered-cubic phase transformation and perfect dislocation slip, are sequentially activated in the tungsten nanocrystal during high-temperature tensile test. Such ductile behavior is related to not only the experimental temperature and but also the loading orientation. These findings shed light on the atomic-scale plastic deformation in body-centered cubic metals at elevated temperature.

6.1 Introduction

Many body-centered cubic (BCC) refractory metals, such as molybdenum (Mo) and tungsten (W), are critical constituents of high temperature alloys used in fusion reactors[153, 261] and

turbine engines[262, 263]. BCC structured metal materials usually have high strength, Young's modulus and chemical durability, but they are brittle at room temperature and exhibit quite limited ductility at high temperature[232, 233, 234], which makes it difficult to investigate their ductile behaviors. In addition, the deformation characteristics of BCC metals are complex, due to the unique nonplanar nature of screw dislocation core[153, 264, 265, 266]. To date, compared to face-centered cubic (FCC) metals, the plastic deformation behaviors and the underlying mechanisms for BCC metals remain much less understood. Considering the widespread use of BCC metals in industrial applications, deep insights into their atomic-scale plastic deformation mechanisms are of vital importance.

Recent advances in *in situ* experimental mechanics open new avenues to investigate the mechanical behaviors of nanostructured metals. Some deformation behaviors and the underlying atomic-scale mechanisms in BCC nanostructured metals have been revealed, including surface dislocation nucleation[143], dislocation slip[143, 158], deformation twinning[143, 144, 146], shear band dynamics[97, 158] and phase transformation[43, 145, 267, 268]. However, the prior studies focused on the mechanical properties and deformation behaviors of nanoscale BCC metals at room temperature. To date, the plastic behaviors of BCC nanocrystals at elevated temperature remain largely unexplored, especially at the atomic scale, due to the technical difficulties in achieving high temperature environmental conditions in an extremely small TEM chamber. It naturally raises the question of whether the plastic deformation mechanisms of BCC metals at room and elevated temperatures are different. Molecular dynamics (MD) simulations are usually employed to investigate the high-temperature deformation behaviors of nanoscale metal materials[37, 39, 160, 161]. Suffering from the inherent high strain rates, the accuracy of interatomic potentials[57, 59, 79] and the uncertainty in sample geometry[60], the computational results remain questionable, when they are

directly extrapolated to those under the laboratory conditions. Thus, *in situ* atomic-scale high-temperature mechanical testing method is in urgent need for studying the high-temperature plastic deformation in BCC metallic nanocrystals to fill the knowledge gap.

Here, a novel testing method is developed, which allows *in situ* deformation at elevated temperature. This high-temperature testing method is based on the Joule heating effect produced by electrical current flow along the metallic nanocrystals. W nanocrystal is used as a model system to study the plastic deformation behaviors of BCC metallic nanocrystals. By conducting *in situ* tensile tests at elevated temperature and imaging using high resolution transmission electron microscopy (HRTEM), deformation twinning, BCC-FCC-BCC phase transformation and perfect dislocation slip are observed to sequentially occur in the W nanocrystals. Such ductile behavior is related to not only the experimental temperature and but also the loading orientation. Deep insights into the high-temperature ductile behaviors of BCC metals are of considerable importance from the standpoints of both scientific understanding and their practical applications.

6.2 Experimental Procedures

The single-crystalline W nanocrystals were fabricated directly inside TEM using *in situ* nanowelding, as described in Chapter 3.1.3. Following Huang's testing method used to investigate the ductile behaviors of carbon nanotube at high temperature[240, 241, 242], *in situ* high-temperature nanomechanical testing method for metallic nanocrystals is developed here. The underlying concept of this method is that Joule heating, induced by the electric current, could elevate the experimental temperature of the W nanocrystal, and the temperature becomes steady in a quite short period of time[269] (Figure 6.1). In this study, Nanofactory TEM-STM (scanning tunneling

microscope) holder allows for measuring the electric current of the metallic nanocrystals under a constant bias voltage[270]. Then COMSOL Multiphysics based on finite element analysis (FEA) is utilized to provide accurate prediction of the temperature of the W nanocrystals, based on the thermal conductivity of the metallic nanocrystal (111.24 $W \cdot m^{-1} \cdot K^{-1}$ [271]), emissivity (0.35 [272]), the measured electric current and the bias voltage applied on the two ends of the sample[273]. Due to the fact that the sample in TEM chamber is under vacuum condition, natural convection can be ignored to simplify the simulation. The calculated temperatures of the 7.4-nm-diameter W nanocrystal (Figures 6.2 and 6.4) during tensile test under the constant bias of 0.4 V and the electric current of 2.6 mA-3.7 mA are within the range from 1007 K to 1019 K, which are higher than the ductile-to-brittle transition temperature (DBTT) of nearly 500 K-700 K[274] for W. Thus, the bias voltage of 0.4 V is chosen in this study to investigate the high-temperature deformation behaviors of the 7.4-nm-diameter W nanocrystal. Likewise, the bias voltage of 0.35 V (the electric current of 3.5 mA-5.7 mA) is chosen for the 6.7-nm-diameter W nanocrystal (Figure 6.10). *In situ* tensile tests at high temperature are conducted inside a FEI Titan TEM equipped with a Nanofactory STM holder. The strain rate of 10^{-3} s^{-1} during tensile tests are controlled by the movement speed of the W nanoprobe. Moreover, all the tests are operated at 200 kV with low dose conditions (electron beam intensity < $10^{5} A \cdot m^{-2}$) in a short time (less than 3 min) to minimize the potential beam effects on the deformation behavior of W nanocrystals[220, 221].

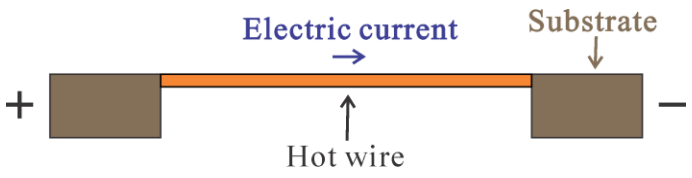

Figure 6.1 The experimental temperature is elavated due to the Joule heating effect induced by the electric current through the metallic nanocrystal.

6.3 Experimental Results

6.3.1 Deformation Twinning In W Nanocrystal At High Temperature

Figure 6.2 shows the atomic-scale deformation process of a 7.4-nm-diameter W nanocrystal at the strain rate of 10^{-3} s^{-1} and under the temperature range of 1011 K to 1019 K. The loading direction is along [002] direction, and the viewing direction is along $[1\bar{1}0]$ zone axis, which allows for observing perfect and partial dislocation slip during mechanical test. As shown in Figure 6.2a, the as-fabricated W nanocrystal is defect free. The gauge section, used to quantify the nanocrystal elongation, is selected based on the shape evolution of the W nanocrystal during tensile test[28, 37, 42]. During the entire loading process, plastic deformation occurs within the gauge section, and the diameters of the boundaries of the chosen gauge section remain nearly unchanged. Under tensile loading, the W nanocrystal firstly undergoes elastic deformation. As the lattice stress inside the W nanocrystal reaches the yielding point, a deformation twin with the operating twinning system of either $(1\bar{1}2)$ $[\bar{1}11]$ or $(\bar{1}12)$ $[1\bar{1}1]$ nucleates, resulting in a uniform elongation of 14.1% (Figure 6.2b and Figure 6.3a-b), which is determined by monitoring the change in gauge length. With the increase of tensile strain, the deformation twin grows along the loading direction, which is mediated by the consecutive slip of $1/6[\bar{1}11]$ or $1/6[1\bar{1}1]$ twinning partial dislocations (Figure 6.2c and Figure 6.2b-c). The completion of the twinning process ultimately results in the uniform elongation as large as 40% (Figure 6.2d and Figure 6.3d), which agrees well with the theoretical value of 41.4% resulted from twinning-induced lattice reorientation[275, 276]. Though the newly formed coherent twin boundaries, either $(1\bar{1}2)$ or $(\bar{1}12)$, are not in the edge-on condition when viewed along $[1\bar{1}0]$ crystal direction, the occurrence of deformation twinning can be further confirmed through examining the crystallographic orientation relationship between the matrix and

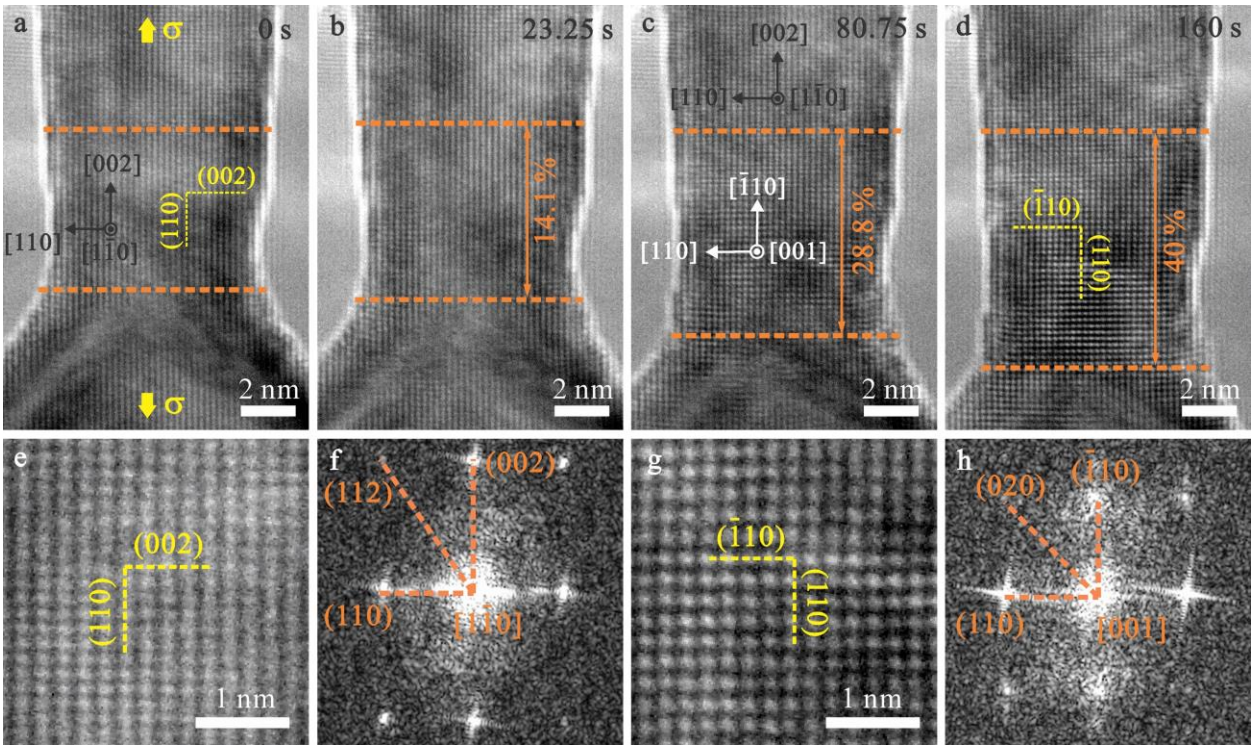

Figure 6.2 Deformation twinning in the 7.4-nm-diameter W nanocrystal under [002] tensile loading at the strain rate of 10^{-3} s^{-1} and under the temperature of 1011 K-1019 K(a) High-resolution TEM image of the pristine W nanocrystal. The viewing and loading directions are along [1$\bar{1}$0] and [002], rexpectively. The dashed lines indicate the gauge section used for calculating the elongation strain during tensile test. (b) Nucleation of a deformation twin with a twinning system of (11$\bar{2}$) [1$\bar{1}$1] or (1$\bar{1}$2) [11$\bar{1}$], causing a sudden elongation of 14.1%. (c) Growth of the deformation twin during further tensile loading. (d) The deformed W nanocrystal after deformation twinning exhibites an uniform elongation of nearlly 40%. (e-f) Magnified high resolution TEM image (e) and fast Fourier transform pattern (f) of the pristine W nanocrystal before tensile test. (g-h) Enlarged high resolution TEM image (g) and fast Fourier transform pattern (h) of the area in the deformation twin.

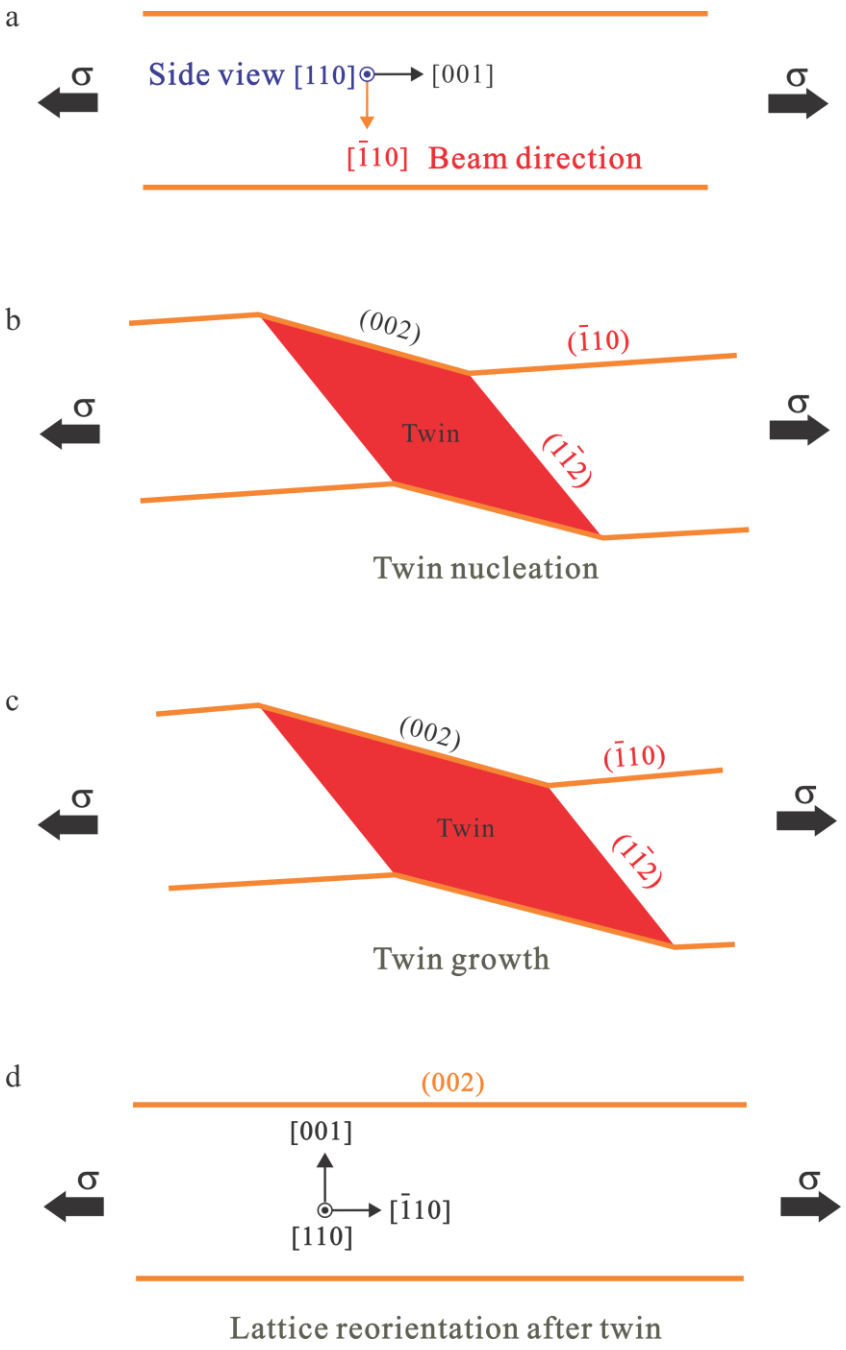

Figure 6.3 Schematics showing the process of deformation twinning in W nanocrystal, when viewed along the [110] zone axis. One of the two possible equivalent twinning systems, namely 1/6[$\bar{1}$11](1$\bar{1}$2), is selected.

the twin. The enlarged HRTEM images (Figures 6.2e and 6.2g) and the corresponding fast Fourier transform pattern (Figures 6.2f and 6.2h) show that the axial direction of the W nanocrystal is reoriented from the original [002] to [$\bar{1}$10], and the viewing direction is changed from the original [1$\bar{1}$0] to the [001] zone axis, which is consistent with lattice reorientation caused by deformation twinning[161, 277]. Given that the Burgers vector directions of the twinning partials (1/6[$\bar{1}$11] and 1/6[1$\bar{1}$1]) are perpendicular to the direction of sample width ([110]), deformation twinning does not induce any change in sample diameter.

6.3.2 BCC-FCC-BCC Phase Transformation In The W Nanocrystal At High Temperature

After the completion of twinning process (Figure 6.4a), two regions (Region II and III) with different structural features appear in the twinned region (Region I) of W nanocrystal at the temperature of 1007 K-1011 K (Figure 6.4b), indicating the occurrence of phase transformation. A close observation of the crystal lattices in the different regions shows that the [001] lattices of BCC-structured W in Region I exhibit square-shape (the inset in Figure 6.4a), while the lattice shapes in Region II (the inset in Figure 6.4 b) and Region III (the inset in Figure 6.4 c) are rhombus. To identify the crystal structure of the new phases, the vectors between the transmission spot and the nearest (R1), second nearest (R2) and third nearest diffraction spots (R3) are examined in the fast Fourier transformed images of the three regions (Figure 6.4d-f). The ratios of R3/R1 and R2/R1 and the angle between R1 and R2 in Region II are 1.16, 1, 70.4°, respectively, which are different from the characteristic parameters of the <100>-BCC lattice (1.4, 1, 90° in Figure 6.4d), but match well with the characteristic parameters of the <110>-FCC lattice (1.15, 1, 70.5°)[278], suggesting that the crystal structure in Region II is FCC rather than BCC. Moreover, the experimental data for the lattice in Region III (1, 1, 60°) are consistent with the characteristic

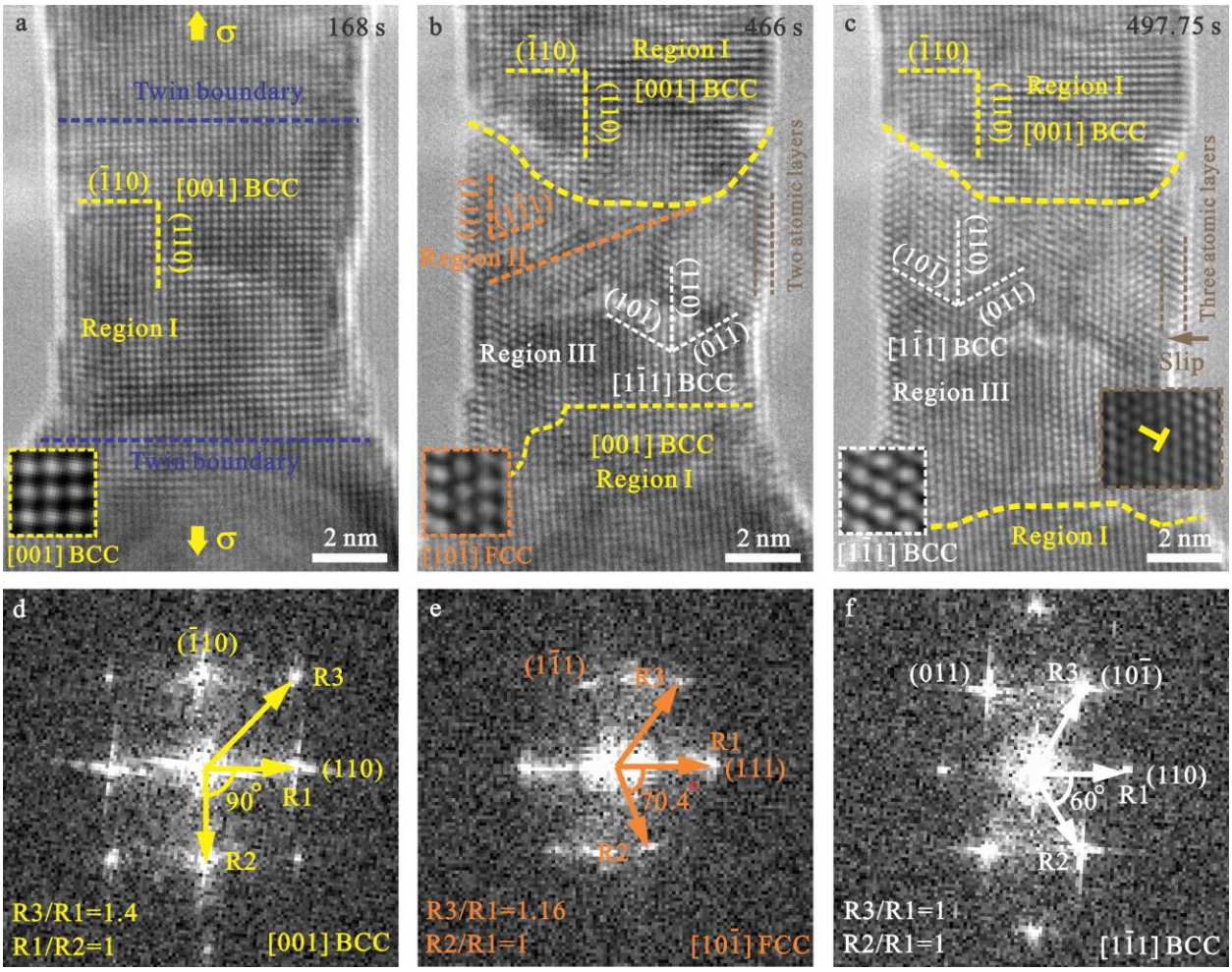

Figure 6.4 BCC-FCC-BCC phase transformation in 7.4-nm-diameter W nanocrystal within the temperature range from 1007 K to 1011 K. (a) TEM image of the deformed W nanocrystal after deformation twinning. Filtered TEM image in the inset shows the atomic structures of the <001>-BCC lattice. (b-c) Occurrence of BCC-FCC-BCC phase transition. Filtered TEM images in the insets of (b) and (c) show the atomic structures of the <110>-FCC lattices and <111>-BCC lattices, respectively. The red dashed line represents the <111>-BCC/<110>-FCC interface. The yellow dashed line represents the interface between the <001>-BCC lattice and the other two phases. After phase transformation, the loading direction is reoriented from <110> to <112>, and the viewing direction changes from <001> to <111>. Perfect dislocation slip is observed in <111>-BCC lattice, causing the increase in the surface step hight by one atomic layer. The TEM image in the inset of (c) shows the surface nucleated perfect dislocation. (d-f) Fast Fourier transform patterns of the <001>-BCC, <110>-FCC and <111>-BCC lattices.

parameters of the <111>-BCC lattice (1, 1, 60°)[278]. Thus, the crystal lattice in Region III is determined to be BCC-structured W along <111> zone axis. In addition, Figure 6.4b and Figure 6.4d-f show that the orientation relation between the <001>-BCC lattice and the <110>-FCC lattice is consistent with the Nishiyama-Wassermann (N-W) relationship ([001]//[10 $\bar{1}$] and (110)//(111))[279], and the orientation relationship between the <110>-FCC lattice and the <111>-BCC lattice follows the Kurdjumov-Sachs (K-S) relation ([10$\bar{1}$]//[1$\bar{1}$1] and (111)//(110))[280]. The good agreement with the well-established crystallographic relationship between FCC and BCC phases corroborates the above analysis on the crystal structures. The comparison between the filtered TEM images in the three regions (the insets in Figure 6.4a-c) and the simulated HRTEM images of FCC- and BCC-structured W (Figure 6.5) also demonstrates that the lattices in Region I, II and III should be <001>-BCC lattice, <110>-FCC lattice and <111>-BCC lattice, respectively. With further tensile loading, the <110>-FCC lattices, bridging the two BCC lattices, transform to new <111>-BCC lattices (Figure 6.4b-c), indicating that the FCC phase is a metastable intermediate phase for the phase transition from <001>-BCC lattice to <111>-BCC lattice, which is similar to the two-step BCC-FCC-BCC phase transition observed in Nb nanowire[145] and Mo thin film[268]. The first phase transition from <001>-BCC lattice to <110>-FCC lattice follows the N-W transformation process, and the second phase transition from <110>-FCC lattice to <111>-BCC lattice follows the K-S transformation process.

In addition to the BCC-FCC-BCC phase transformation, perfect dislocation slip occurs in Region III with <111>-BCC lattice, as demonstrated by the observation of a perfect dislocation (the inset in Figure 6.4c) and the increase in the height of a surface step (Figure 6.4b-c) [97, 145]. After tensile failure, the BCC-structured W along <111> zone axis could stably exist in the fractured nanocrystal under zero external stress at room temperature (Figure 6.6a). The fast Fourier

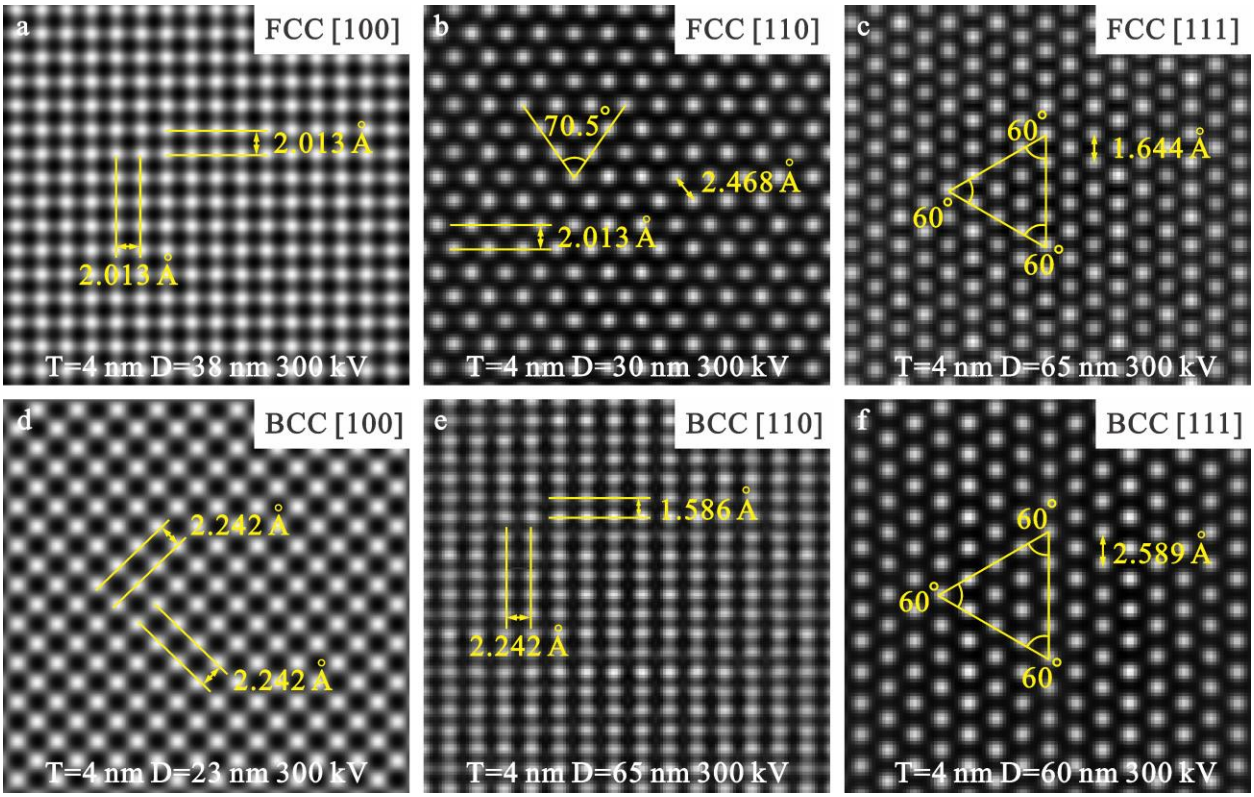

Figure 6.5 Simulated HRTEM images of FCC- and BCC-structured W viewed along several low-indexed zone axes. The interplanar angles and the projecting lattice distances of the adjacent atomic coloumns along different crystallographic directions are both indicated. By comparing the experimental observation of the new lattices in the W nanocrystal with the simulated HRTEM images, the new lattices can be determined to be FCC-structured W in the <110> zone axis and BCC-structured W in the <111> zone axis. "T" and "D" in all the images indicate the thickness of the simulated W nanocrystal and the defocus distance used in simulation,

respectively.

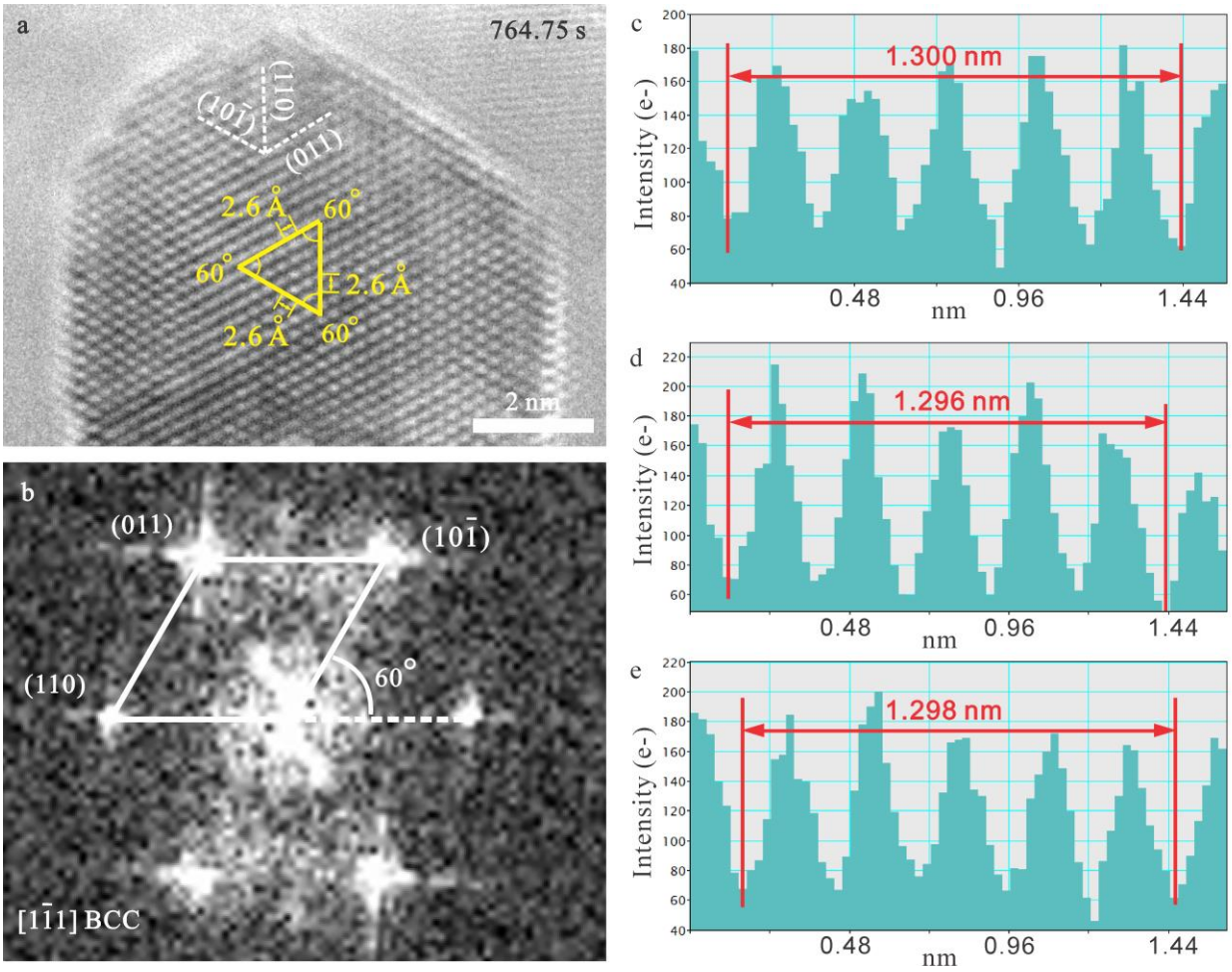

Figure 6.6 <111>-BCC phase in the fractured W nanocrystal. (a) TEM image of the fractured W nanocrystal showing that <111>-BCC phase could exist for a long time under zero external stress at room temperature. (b) Fast Fourier transform patterns of (a), which is in good agreement with the transmission electron pattern of BCC-structured W in [111] zone axis. (c-e) Measurement of the lattice distances of 5 atomic columns along <112> directions. The lattice distances of the two neighboring atomic columns along <112> directions are measured to be 2.6 Å, and the interplaner angles between the edge-on {111} planes are determined to be 60°.

transform patterns of the crystal lattice in the fracture nanocrystal (Figure 6.6b) is in good agreement with the transmission electron pattern of BCC-structured W in [111] zone axis[278]. To further validate the above analysis on the crystalline structure in Region III, the distances between the adjacent atomic columns along <112> directions are carefully measured (Figure 6.6 c-e), based on the difference in the contrast of the areas inside and outside the atomic columns[28, 37, 42]. To minimize the measurement errors, the lattice spacing measurements for 5 atomic columns are conducted in this study[170, 207] (Figure 6.6 c-e). The lattice distances of the two neighboring atomic columns along <112> directions (indicated by the yellow lines in Figure 6.6a) are determined to be 2.6 Å, and the interplanar angles between the {110} planes are measured to be 60°, which are consistent with the characteristic parameters of the <111>-BCC lattice (2.589 Å and 60° in Figure 6.5f). It further proves the occurrence of BCC-FCC-BCC phase transformation in W nanocrystal.

Based on the above microstructural analysis, it is demonstrated that deformation twinning, BCC-FCC-BCC phase transformation and perfect dislocation slip sequentially occur in the 7.4-nm-diameter W nanocrystal during high-temperature tensile test (Figure 6.2 and Figure 6.4). Different from the high-temperature ductile behaviors, only deformation twinning is observed to occur in the W nanocrystal under [002] tensile loading at room temperature, as shown in Figure 6.7. Moreover, the room-temperature tensile test of the <110>-oriented W nanocrystal shows that perfect dislocation slip on {110} planes is the dominant mechanism, and no phase transformation is observed (Figure 6.8). Thus, the experimental observation of BCC-FCC-BCC phase transformation in W nanocrystal is associated with the experimental temperature.

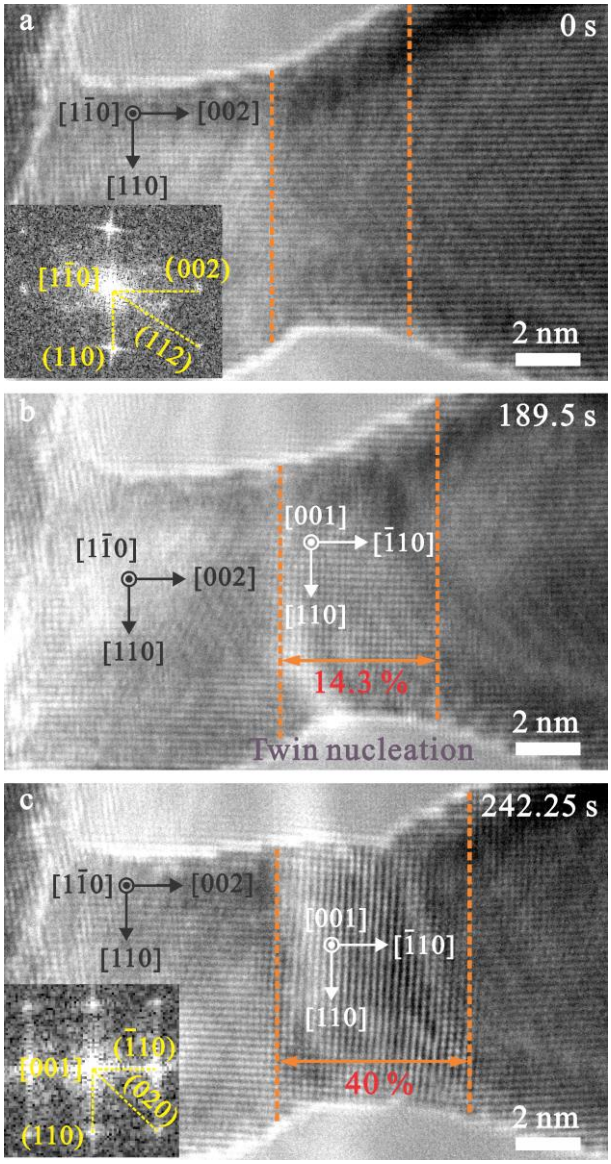

Figure 6.7 Deformation twinning in W nanocrystal at room temperature. (a) TEM image of the pristine 8.2-nm-diameter W nanocrystal under [002] tensile loading at the strain rate of 10^{-3} s^{-1}. The viewing direction is [1$\bar{1}$0]. The dashed lines indicate the gauge section used for calculating the elongation strain of the nanocrystal. The inset in (a) is the fast Fourier transform pattern of the pristine W nanocrystal. (b) Nucleation of a deformation twin resulting in the uniform elongation of 14.3%. (c) The deformed W nanocrystal exhibited an uniform elongation of nearlly 40% caused by deformation twinning. The inset in (c) is the fast Fourier transform pattern of the twinned W nanocrystal showing lattice reorientation from [002] to [$\bar{1}$10] direction.

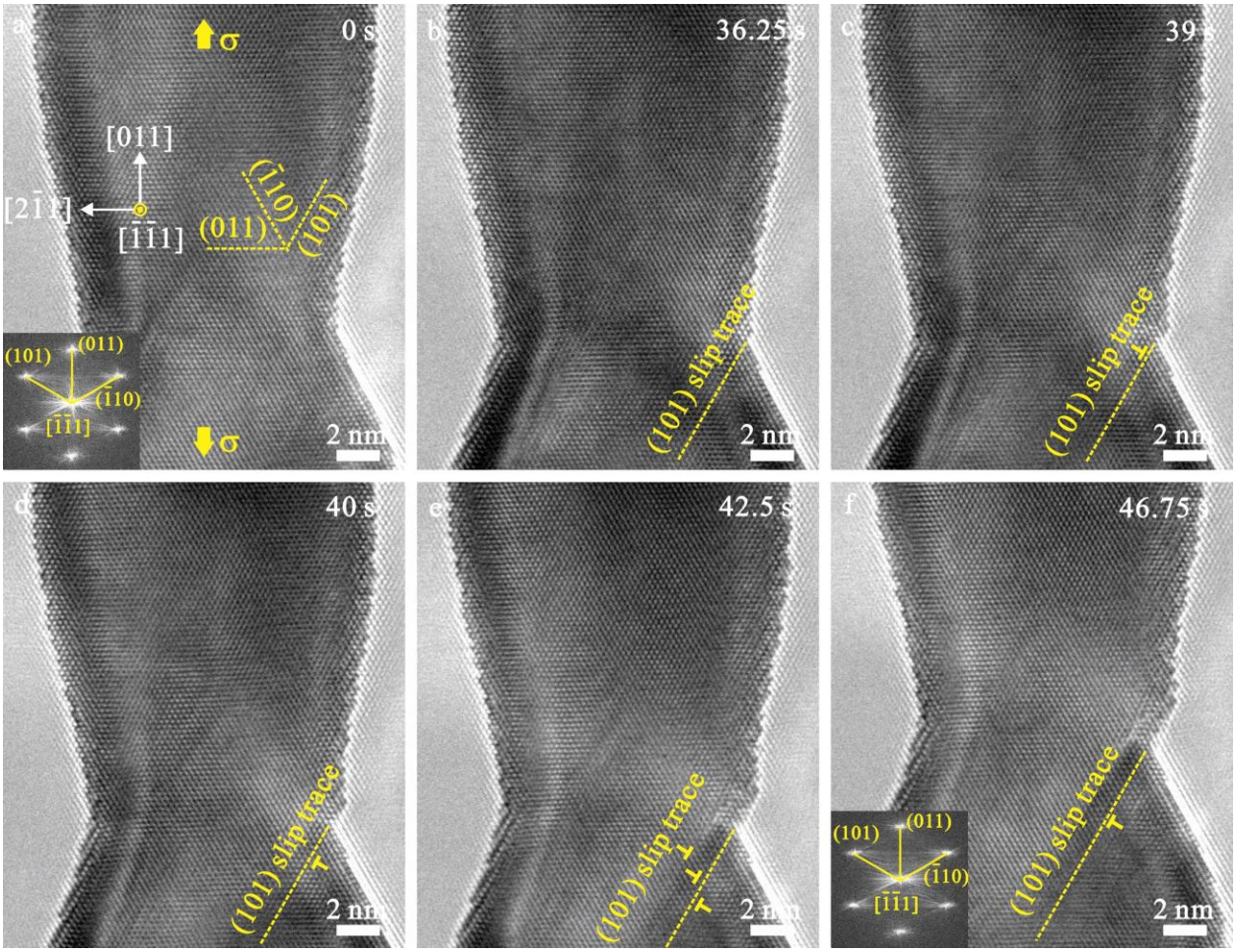

Figure 6.8 Dislocation-mediated plasticity in a 12.1-nm-diameter W nanocrystal under <110> tensile loading at room temeperature. (a) TEM image of the pristine W nanocrystal loaded at the strain rate of 10^{-3} s^{-1}. The viewing direction is [$\bar{1}\bar{1}$1] zone axis. The inset in (a) is the fast Fourier transform pattern of the pristine W nanocrystal. (b-f) A series of TEM images showing the occurrence of perfect dislocation slip on (101) planes in the W nanocrystal upon tensile loading. The inset in (f) is the fast Fourier transform patern of the deformed W nanocrystal demonstrating that no phase transformation occurs.

6.3.3 Orientation Dependence Of The Deformation Behaviors Of W Nanocrystals

To probe the orientation dependence of the deformation behaviors of W nanocrystals, *in situ* tensile test of a [112]-oriented W nanocrystal with the diameter of 8.7 nm is conducted at room temperature under a strain rate of 10^{-3} s^{-1} (Figure 6.9). The fast Fourier transform pattern of the pristine W nanocrystal shows that the axial and viewing directions of the nanocrystal are parallel to [112] and $[\bar{1}\bar{1}1]$ direction, respectively (Figure 6.9a). Before tensile test, no lattice defects are observed in the as-fabricated W nanocrystal. Upon the yielding of the W nanocrystal, $1/2[\bar{1}11]$-type dislocations nucleate from the free surface and then glide on (101) slip planes, as shown in Figure 6.9b. The annihilation of these dislocations at the free surface results in the formation and enlargement of the surface step (Figure 6.9b). Further tensile deformation of the W nanocrystal is mediated by perfect dislocation slip, causing continuous decrease in the nanocrystal width (Figure 6.9c-f). The room-temperature deformation behaviors of W nanocrystals are consistent with the previous experimental observation of dislocation-dominated plasticity in BCC nanocrystals[97, 143, 158]. The fast Fourier transform pattern of the deformed W nanocrystal (the inset in Figure 6.9f) shows that no phase transformation occurs in the W nanocrystal during tensile loading.

To investigate the high-temperature deformation behaviors of W nanocrystals under [112] tension, the tensile test of a 6.7-nm-diameter W nanocrystal is performed at the strain rate of 10^{-3} s^{-1} under the temperature range of 912 K to 915 K (Figure 6.10). Similar to the room-temperature deformation behaviors, plastic deformation in the W nanocrystal at high temperature is mediated by the slip of 1/2<111> perfect dislocations, including the nucleation of dislocations from free surface, the subsequent dislocation propagation across the nanocrystal and dislocation annihilation at free surface (Figure 6.10). The fast Fourier transform patterns of the pristine and deformed W nanocrystals (the insets in Figure 6.10a and 6.10f) show that the lattice structures of the W

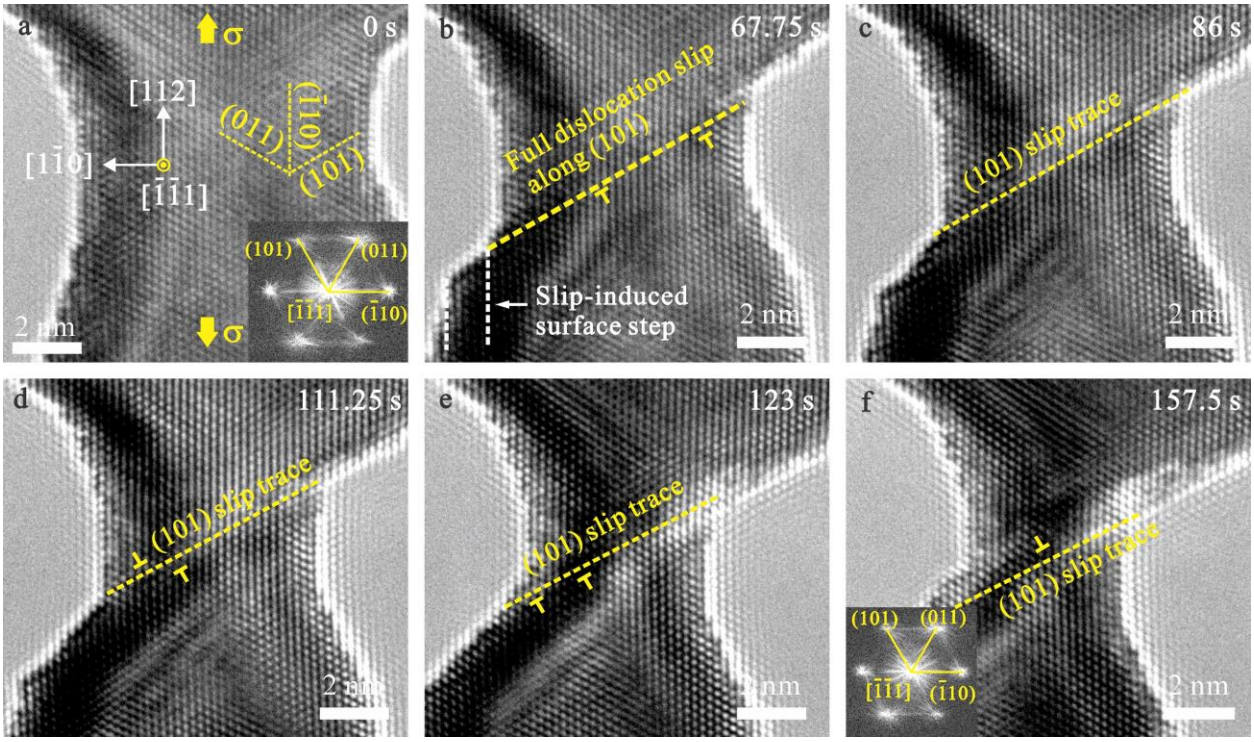

Figure 6.9 Dislocation-mediated plasticity in a 8.7-nm-diameter W nanocrystal under <112> tensile loading at room temeperature. (a) TEM image of the pristine W nanocrystal loaded at the strain rate of 10^{-3} s^{-1}. The viewing direction is along [$\bar{1}\bar{1}$1]. (b-f) Sequential TEM images showing that dislocation slip occurs in the W nanocrystal during tensile test. The insets in (a) and (f) are the fast Fourier transform images of the pristine and deformed W nanocrystals, rexpectively, demonstrating that no phase transformation occurs.

nanocrystals remain unchanged during the high-temperature tensile test. Thus, no phase transformation occurs in the [112]-oriented W nanocrystals at room and high temperatures. The BCC-FCC-BCC phase transformation could only occur in the W nanocrystal under [110] tensile loading at high temperature. Thus, the occurrence of BCC-FCC-BCC phase transformation in W nanocrystal is related to the loading direction and the experimental temperature. It should be noted that dislocation starvation is not always observed in the W nanocrystals during mechanical loading (Figure 6.8, Figure 6.9 and Figure 6.10), which is associated with the low mobility of screw dislocations with non-planar core structure[230, 232, 281, 282, 283].

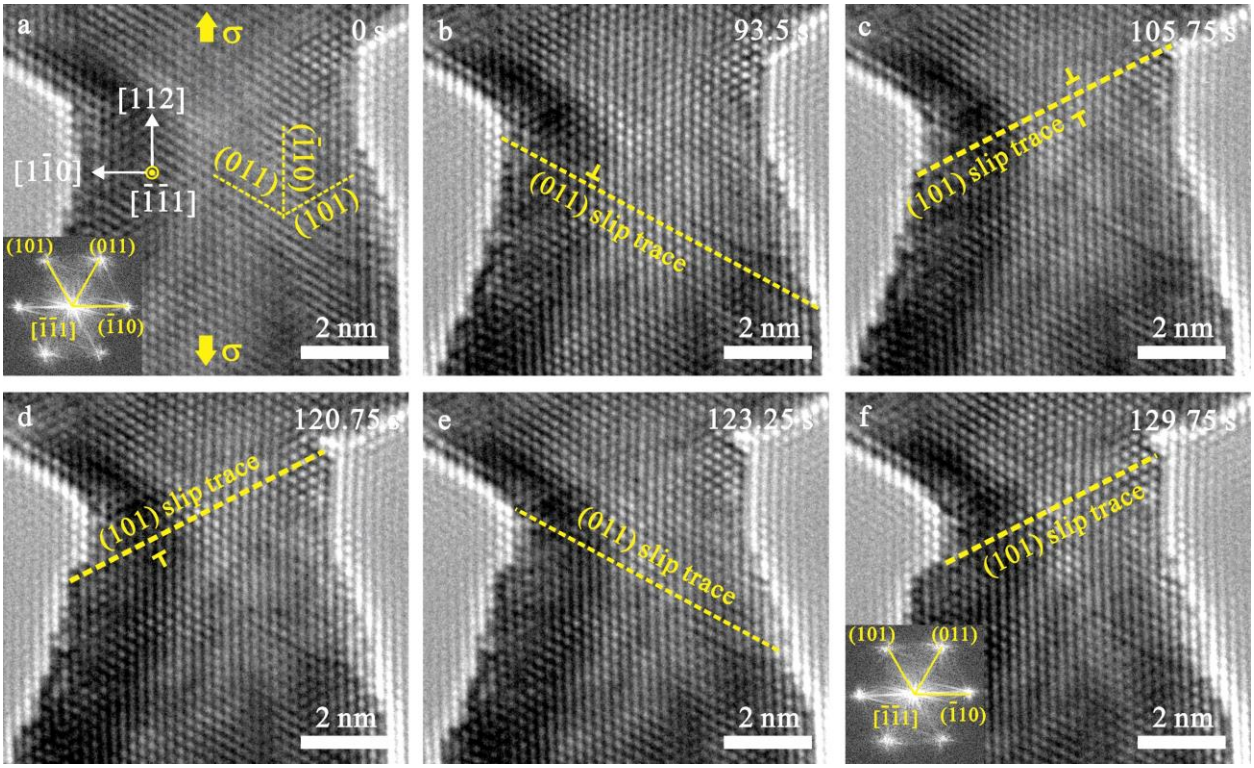

Figure 6.10 Dislocation-mediated plasticity in a 6.7-nm-diameter W nanocrystal under [112] tensile loading within the temeperature range from 912 K to 915 K. (a) TEM image of the pristine W nanocrystal loaded at the strain rate of 10^{-3} s^{-1}. The viewing direction is along [$\bar{1}\bar{1}$1] zone axis. The inset in (a) is the fast Fourier transform pattern of the pristine W nanocrystal. (b-f) Sequential TEM images showing ththe occurrence of perfect dislocation slip on (101) and (011) planes in the W nanocrystal upon tensile deformation. The inset in (f) is the fast Fourier transform pattern of the deformed W nanocrystal demonstrating that no phase transformation occurs.

6.4 Discussion

To date, a wealth of experimental and theoretical studies on the deformation behaviors of bulk BCC metals[137, 284, 285, 286, 287, 288] and BCC nanopillars[135, 230, 232, 281, 289, 290] showed that 1/2<1 1 1> screw dislocation was the only plastic deformation carrier. As the microstructural feature size

of BCC metal decreases to nanoscale, the high stress, resulting from the well-established 'smaller is stronger' norm, facilitates the activation of deformation twinning and phase transformation[143, 144, 145, 146, 268, 291]. The experimental observation of BCC-FCC-BCC phase transformation in this study is also attributed to the high lattice stress accumulated in the twinned region of the W nanocrystal during tensile deformation. The high stress in the W nanocrystal could provide sufficient energy to stimulate lattice instabilities and serves as a thermodynamic driving force for overcoming the energy barrier for phase transformation[145, 268, 291]. Furthermore, according to transition state theory, the increase in temperature and stress could lower the activation energy for structural transformation[56, 80, 133, 218, 292]. Thus, phase transformation is energetically favorable in the deformed W nanocrystal at high temperature. In addition to the high stress and the experimental temperature, the loading orientation is also a critical factor influencing the activation of phase transformation. In this study, the applied tensile loading direction for the W nanocrystal is parallel to the BCC (110) and the FCC (111) planes (Figure 6.4). Given that the yield strength for W nanocrystal is ~19.2 GPa[143], the extremely high resolved shear stress (~19.2 GPa) on the BCC (110) and the FCC (111) planes could induce successive atomic shear on the (110) and the (111) planes, resulting in the occurrence of BCC-FCC-BCC phase transformation[268, 293].

This work reveals that the loading orientation significantly influences the dominant deformation mode in nanoscale W. Different from FCC metals, the orientation-dependent deformation behaviors observed in W nanocrystal cannot be well explained by Schmid factor analysis, due to the interplay between the non-planar screw dislocation core and the applied stress[146, 294]. In BCC metals, the dominant deformation mechanism is related to the so-called twinning-antitwinning slip asymmetry of 1/6<111> partial dislocations on {112} planes[157, 159, 295, 296]. Under uniaxial tensile loading, the <100>-oriented W nanocrystal is in the twinning-orientation

favoring the activation of deformation twinning, while the <110>- and <112>-oriented W nanocrystals are in the antitwinning-orientations, favoring the activation of perfect dislocation slip. Furthermore, the largest Schmid factors for dislocation slip and twinning in <100>-oriented W nanocrystal are 0.41 and 0.47, respectively, further facilitating the operation of deformation twinning. In contrast, the largest Schmid factors for slip and twinning in <112>-oriented W nanocrystal are 0.41 and 0.39, respectively, and the largest Schmid factors for slip and twinning in <110>-oriented W nanocrystal are 0.47 and 0.41, respectively, facilitating the activation of perfect dislocation slip. As a result, W nanocrystal with <100> orientation is observed to deform by deformation twinning on {112} planes (Figure 6.2 and Figure 6.47), whereas the deformation in <110>- and <112>-oriented W nanocrystal is mediated by perfect dislocation slip on {110} planes (Figure 6.8, Figure 6.9 and Figure 6.10), which is consistent with the previous experimental and computational results[29, 143, 159, 160, 283, 297, 298, 299].

In addition to the loading orientation, experimental temperature is another critical factor influencing the deformation behaviors of W nanocrystals. It has been well documented that the tendency for twinning in bulk FCC and BCC metals usually decreases with increasing experimental temperature[52, 300]. However, previous MD simulations revealed that deformation twinning occurred in W nanowire at temperature higher than 1500 K[161]. Consistent with the previous computational results, this study provides the direct experimental evidence that deformation twinning is the dominant deformation mechanism in W nanocrystals at high temperature (1007-1019 K). After the completion of twinning process, BCC-FCC-BCC phase transformation subsequently occurs in the twinned region to mediate the plasticity of W nanocrystal. Moreover, computational studies on the tensile behavior of W nanowire revealed that the [112]-oriented W nanowire failed in a brittle manner at 300 K but deformed by twinning on

{112} planes at 800 K, exhibiting the temperature-dependent brittle-to-ductile transition in deformation behaviors[301]. Different from the computational results, the experimental observations in this study show that perfect dislocation slip mediates the plasticity of the [112]-oriented W nanocrystals at both room (300 K) and high temperatures (912 K-915 K). Such difference between the experimental and computational results is probably attributed to the high strain rates used in MD simulations[28, 53, 80, 302] and the uncertainty in interatomic potentials[57, 59, 79] and sample geometry[60]. Directly validating the research findings from computational investigations, the *in situ* high-temperature nanomechanical testing method developed in this study opens new avenues to investigate the high-temperature deformation behaviors of nanostructured metals at the atomic scale.

6.5 Conclusion

In conclusion, a *in situ* high-temperature nanomechanical testing method is proposed, which is based on the Joule heating effect caused by the electric current through W nanocrystals. Using such method, the atomic-scale deformation behaviors of W nanocrystals at high temperature are investigated. Deformation twinning, BCC-FCC-BCC transformation and perfect dislocation slip are sequentially activated to mediate the plasticity of W nanocrystal. The dominant deformation mode in W nanocrystals is related to the loading orientation and the experimental temperature. This *in situ* study sheds light on understanding the high-temperature deformation behaviors of BCC metals at the atomic scale.

7.0 Summary And Conclusions

The main goal of this dissertation is to understand the mechanical behaviors of nanoscale metals at the atomic scale, which is of importance not only for scientific understanding but also for developing high-performance flexible and stretchable electronics. FCC- and BCC-structured nanocrystals are adopted as the model systems for this project, and TEM-based *in situ* nanomechanical testing is used to directly reveal the dynamic deformation process of FCC- and BCC-structured nanocrystals.

Atomic-scale compressive deformation behaviors, mediated by coupled displacive-diffusive mechanisms, are revealed in Ag nanocrystals. Preexisting dislocations and crystal slip result in a change in surface contour, altering the coordinated environment of the surface atoms. Driven by the difference in chemical potential, diffusional events are activated at the free surface of the Ag nanocrystal, resulting in the migration of surface steps toward the nanocrystal end. The coupled displacive-diffusive mechanisms mediate the compressive deformation of nanoscale Ag, leading to a continuous decrease in the nanocrystal width. As the width of Ag nanocrystal reduces to a critical value, tensile-fracture-like failure occurs, caused by the breaking of atomic bonds and the diffusion of surface atoms. In contrast to the coupled displacive-diffusive deformations in Ag nanocrystal, pure displacive deformation is dominant in Pt nanocrystal during compression. The nucleation, propagation and annihilation of perfect dislocations result in the local thickening of Pt nanocrystal. These findings bolster the current understanding of compressive deformation behaviors in small volume metals.

Atomic-scale processes of fivefold twin formation in Au nanocrystals are revealed. Sequential twinning dislocation slip in varying slip systems and the decomposition of high-energy

grain boundary at the node of a multifold twin are responsible for the formation of fivefold twin in the nanoscale Au single crystal under bending as well as the formation and dissolution of fivefold twin in Au nanocrystals with preexisting twin under shearing and tension. The morphology of fivefold twin can be tuned via dislocation nucleation from nanocrystal surface, twinning dislocation slip along twin boundaries and the transmission of partial dislocations across twin boundaries under compression or shearing. Moreover, the complex stress state in the neck area and the need for material reorientation favor partial dislocation slip on different twinning systems and thus result in the formation of a fivefold twin in a Au nanocrystal with a twin boundary parallel to the loading direction, which is different from the prediction of Schmid law. These results provide atomistic insights into the formation process of fivefold twin in nanostructured metals under mechanical loading, providing new clues to rationally control microstructural evolution for fabricating high-performance nanostructured metals.

A novel TEM-based *in situ* high-temperature nanomechanical testing method is proposed to investigate the ductile behaviors of BCC metallic nanocrystals at the atomic scale. Such testing method is based on the Joule heating effect produced by the electric current through the metal materials. By this method, the high-temperature deformation behaviors of W nanocrystals are investigated at the atomic scale. Deformation twinning, BCC-FCC-BCC phase transformation and perfect dislocation slip sequentially occur in the W nanocrystal during tensile loading at elevated temperature. The activated deformation modes in W nanocrystals are related to the loading orientation and the experimental temperature. The newly developed high-temperature testing method proposed here opens new avenues to directly validate the research findings from computational investigations. Deep insights into the high-temperature ductile behaviors of BCC metal materials are of considerable importance for their practical applications.

The results from this dissertation advance the fundamental understanding of the mechanical behaviors of metallic nanocrystals with different crystal structures, which are of critical importance for the use of nanoscale metals in emerging technologies.

8.0 Outlook

8.1 Coupled Displacive-Diffusive Deformation In Metallic Nanocrystals

Diffusion, a time-dependent process, often occurs in metal materials at moderate and high temperatures[303]. When the feature size of the metal materials (e.g. gain size and sample size) decreases to the nanoscale regime[304, 305], diffusive deformation could be activated even at room temperature[304, 305]. In nanoscale metal materials, free surface acts as a highway for mass transport, similar to the roles of grain boundary in nanocrystalline metals[82, 83, 306]. Atomic diffusion at free surface could alter the surface atomic configuration of the nanoscale metals[219, 307, 308, 309], and leads to surface-diffusion-assisted dislocation nucleation[42]. Moreover, free surface also serves as both source and sink for vacancies, thereby resulting in small diffusion distance and fast kinetics for lattice vacancy transport, which raises the possibility of the occurrence of vacancy-diffusion-assisted dislocation climb in nanoscale metals. To date, the atomic-scale mechanisms of diffusional deformation remain elusive, due to the significant experimental challenge. Although MD simulations have been proved to be an effective method to investigate the atomic-scale deformation mechanisms of nanoscale metals, it falls short in investigating the diffusive plasticity, due to the extremely high strain rate[56, 98]. The TEM-based *in situ* nanomechanical testing method in this dissertation can be employed to directly visualize the interplay between the displacive and diffusive deformations at the atomic scale and reveals their fundamental mechanisms. The influence of size, strain rate, the type of material and experimental temperature on surface diffusion-assisted dislocation nucleation and vacancy-diffusion-assisted dislocation climb can be

systematically investigated. The room-temperature mechanical properties of nanoscale metals, mediated by the displacive-diffusive mechanisms, can also be investigated.

8.2 Atomic-Scale Mechanical Behaviours Of Fivefold Twinned Nanocrystal

Nanoscale metal materials often surprise us with unexpected mechanical properties and deformation behaviors. Fivefold twin has been reported to substantially improve the mechanical properties of Ag nanowires, such as Young's modulus[165, 166, 167], strain hardening capability[249] and yield strength[171]. Fivefold twinned Ag nanowire also exhibits reversible plastic behavior mediated by surface nucleation, propagation and retraction of partial dislocations. Although the mechanical behaviors of the fivefold twinned metallic nanowires have attracted numerous research interests, the understanding of the deformation features of fivefold twin is still in their infancy, due to the following two reasons. First, conducting *in situ* atomic-scale nanomechanical testing for nanoscale metals remains technically challenging. Second, the chemically synthesized metallic nanowires with a longitudinal fivefold twin were adopted in the previous studies. Since the central line of the fivefold twin is perpendicular to the <110> zone axis, the structure evolution of fivefold twin cannot be observed during mechanical tests. Moreover, the deformation of fivefold twin in the axially loaded nanowires is suppressed, due to the fact that the resolved shear stresses on each constituent twin boundaries are negligible. Hence, fabricating a nanoscale metal with a radially grown fivefold twin is of critical importance for investigating the intrinsic deformation behaviors of fivefold twin at the atomic scale.

The study in Chapter 5 shows that fivefold twin with its central line perpendicular to the axial direction and parallel to the <110> zone axis could be introduced into the Au nanocrystals

via mechanical deformation (tension, shearing and bending). Such mechanically prepared Au nanocrystal allows direct observation of twin boundary migration and perfect/partial dislocation slip during mechanical test. Not only mechanical deformation but also *in situ* nanowelding could be employed to introduce a radial fivefold twin into a Au nanocrystal via applying a bias between two Au nanotips (Figure 8.1), which is attributed to the Joule heating and electron wind force induced by electrical pulse effect[50, 196]. Upon electrical-pulse-induced thermal heating, lattice vacancies are produced in the nanocrystal interior, and then they are condensed, contributing to the generation of partial dislocations[199]. Moreover, the directional electrical wind force drives the movement of the partial dislocations on {111} planes, resulting in the formation of nanoscale twins[50]. The two approaches for preparing fivefold twinned nanocrystal (mechanical deformation-induced fivefold twin and *in situ* nanowelding-induced fivefold twin) provide unique opportunities to investigate the intrinsic deformation behaviors of fivefold twin itself. In addition to the deformation features, the mechanical properties of the nanoscale metals with a radially grown fivefold twin remain unclear, due to the technical challenge in fabricating such sample. The study on investigating the mechanical properties of fivefold twinned nanocrystals could bolster the current understanding on the microstructure-mechanical property-deformation mechanism relationship at small scale.

In summary, future research directions about diffusion-mediated deformation and the intrinsic deformation behaviors of fivefold twin in nanoscale metals are proposed. Substantial efforts are expected to be made for better understanding the atomic-scale deformation behaviors of nanoscale metals. A comprehensive understanding of the mechanical behaviors of small-volume materials is of vital importance for not only fundamental science but also achieving the degradation control of nanoscale materials to realize their potential applications in the nanodevices.

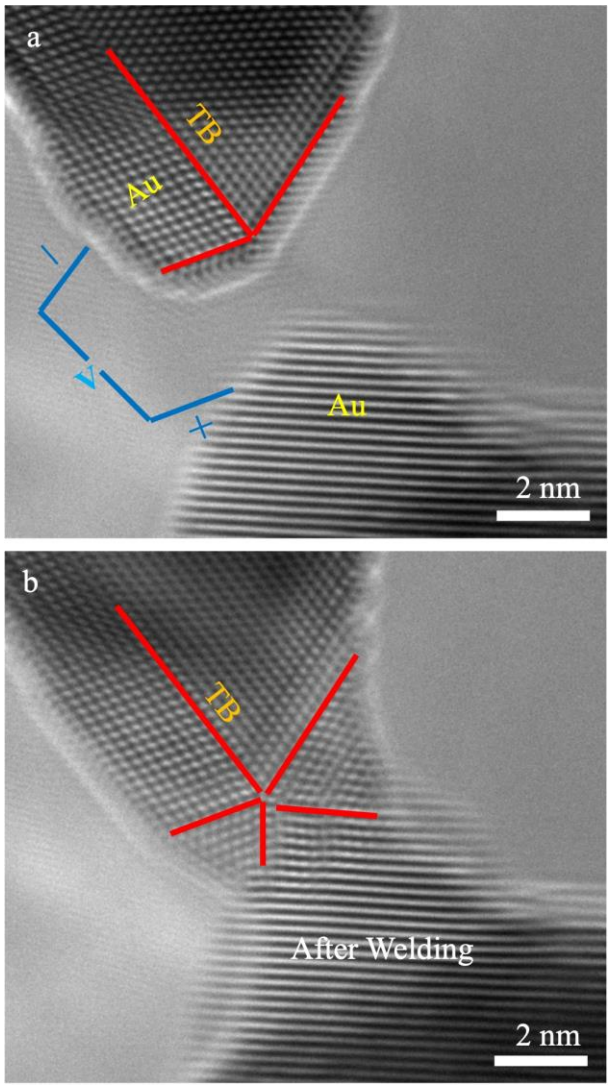

Figure 8.1 Fivefold twin formation in the Au nanocrystal via *in situ* welding. (a-b) The Au nanocrystal before (a) and after (b) *in situ* welding.

Appendix A Young's Modulus Of Au Nanocrystal

The Young's modulus (E_{ijk}) for a [ijk]-oriented single crystal with cubic structure is given by[147]

$$\frac{1}{E_{ijk}} = S_{11} - 2\left(S_{11} - S_{12} - \frac{1}{2}S_{44}\right) \times \left(l_{i1}^2 l_{j2}^2 + l_{j2}^2 l_{k3}^2 + l_{i1}^2 l_{k3}^2\right),$$

where S_{11}, S_{12} and S_{44} are elastic compliances and l_{i1}, l_{j2} and l_{k3} are the direction cosines of the loading direction [ijk]. Considering that the elastic compliances for Au single crystal at room temperature are $S_{11}=2.33\times10^{-2}$ GPa^{-1}, $S_{12}=-1.065\times10^{-2}$ GPa^{-1} and $S_{44}=2.38\times10^{-2}$ GPa^{-1} [147], the Young's modulus for [110]-oriented Au is calculated to be 81.5 GPa.

Bibliography

1. Yao S, Ren P, Song R, Liu Y, Huang Q, Dong J, *et al.* Nanomaterial‐Enabled Flexible and Stretchable Sensing Systems: Processing, Integration, and Applications. *Advanced Materials* 2019**:** 1902343.

2. Segev‐Bar M, Bachar N, Wolf Y, Ukrainsky B, Sarraf L, Haick H. Multi‐Parametric Sensing Platforms Based on Nanoparticles. *Advanced Materials Technologies* 2017, **2**(1)**:** 1600206.

3. Kim J, Lee J, Son D, Choi MK, Kim D-H. Deformable devices with integrated functional nanomaterials for wearable electronics. *Nano Convergence* 2016, **3**(1)**:** 1-13.

4. Kim D-H, Lu N, Ghaffari R, Rogers JA. Inorganic semiconductor nanomaterials for flexible and stretchable bio-integrated electronics. *NPG Asia Materials* 2012, **4**(4)**:** e15-e15.

5. Kim J, Lee M, Shim HJ, Ghaffari R, Cho HR, Son D, *et al.* Stretchable silicon nanoribbon electronics for skin prosthesis. *Nature communications* 2014, **5**(1)**:** 1-11.

6. Ying M, Bonifas AP, Lu N, Su Y, Li R, Cheng H, *et al.* Silicon nanomembranes for fingertip electronics. *Nanotechnology* 2012, **23**(34)**:** 344004.

7. Chang J, Dommer M, Chang C, Lin L. Piezoelectric nanofibers for energy scavenging applications. *Nano energy* 2012, **1**(3)**:** 356-371.

8. Huang Q, Zhu Y. Printing conductive nanomaterials for flexible and stretchable electronics: A review of materials, processes, and applications. *Advanced Materials Technologies* 2019, **4**(5)**:** 1800546.

9. Cui Z, Poblete FR, Zhu Y. Tailoring the Temperature Coefficient of Resistance of Silver Nanowire Nanocomposites and their Application as Stretchable Temperature Sensors. *ACS applied materials & interfaces* 2019, **11**(19)**:** 17836-17842.

10. Yao S, Yang J, Poblete FR, Hu X, Zhu Y. Multifunctional Electronic Textiles Using Silver Nanowire Composites. *ACS applied materials & interfaces* 2019, **11**(34)**:** 31028-31037.

11. Xu F, Zhu Y. Highly conductive and stretchable silver nanowire conductors. *Advanced materials* 2012, **24**(37)**:** 5117-5122.

12. Choi S, Lee H, Ghaffari R, Hyeon T, Kim DH. Recent advances in flexible and stretchable bio‐electronic devices integrated with nanomaterials. *Advanced materials* 2016, **28**(22)**:** 4203-4218.

13. Zhang K, Li J, Fang Y, Luo B, Zhang Y, Li Y, *et al.* Unraveling the solvent induced welding of silver nanowires for high performance flexible transparent electrodes. *Nanoscale* 2018, **10**(27)**:** 12981-12990.

14. Roh E, Hwang B-U, Kim D, Kim B-Y, Lee N-E. Stretchable, transparent, ultrasensitive, and patchable strain sensor for human–machine interfaces comprising a nanohybrid of carbon nanotubes and conductive elastomers. *ACS nano* 2015, **9**(6)**:** 6252-6261.

15. Cui Z, Poblete FR, Cheng G, Yao S, Jiang X, Zhu Y. Design and operation of silver nanowire based flexible and stretchable touch sensors. *J Mater Res* 2015, **30**(1)**:** 79-85.

16. Li C, Zhang D, Cheng G, Zhu Y. Microelectromechanical Systems for Nanomechanical Testing: Electrostatic Actuation and Capacitive Sensing for High-Strain-Rate Testing. *Experimental Mechanics* 2020, **60**(3)**:** 329-343.

17. Guo D, Xie G, Luo J. Mechanical properties of nanoparticles: basics and applications. *Journal of physics D: applied physics* 2013, **47**(1)**:** 013001.

18. Liu P, Wang L, Yue Y, Song S, Wang X, Reddy KM, *et al.* Room-temperature superplasticity in Au nanowires and their atomistic mechanisms. *Nanoscale* 2019, **11**(18)**:** 8727-8735.

19. Cui Z, Han Y, Huang Q, Dong J, Zhu Y. Electrohydrodynamic printing of silver nanowires for flexible and stretchable electronics. *Nanoscale* 2018, **10**(15)**:** 6806-6811.

20. Liang J, Li L, Tong K, Ren Z, Hu W, Niu X, *et al.* Silver nanowire percolation network soldered with graphene oxide at room temperature and its application for fully stretchable polymer light-emitting diodes. *ACS nano* 2014, **8**(2)**:** 1590-1600.

21. Yao S, Zhu Y. Nanomaterial‐enabled stretchable conductors: strategies, materials and devices. *Advanced materials* 2015, **27**(9)**:** 1480-1511.

22. Yao S, Swetha P, Zhu Y. Nanomaterial‐enabled wearable sensors for healthcare. *Advanced healthcare materials* 2018, **7**(1)**:** 1700889.

23. Lin F, Yao S, McKnight M, Zhu Y, Bozkurt A. Silver nanowire based wearable sensors for multimodal sensing. 2016 IEEE Topical Conference on Biomedical Wireless Technologies, Networks, and Sensing Systems (BioWireleSS); 2016: IEEE; 2016. p. 55-58.

24. Lacour SP, Jones J, Wagner S, Li T, Suo Z. Stretchable interconnects for elastic electronic surfaces. *Proceedings of the IEEE* 2005, **93**(8)**:** 1459-1467.

25. Huang Q, Zhu Y. Gravure printing of water-based silver nanowire ink on plastic substrate for flexible electronics. *Scientific reports* 2018, **8**(1)**:** 1-10.

26. Yao S, Cui J, Cui Z, Zhu Y. Soft electrothermal actuators using silver nanowire heaters. *Nanoscale* 2017, **9**(11)**:** 3797-3805.

27. Yao S, Lee JS, Miller J, Narasimhan V, Dickerson AJ, Zhu X, *et al.* Silver nanowire strain sensors for wearable body motion tracking. 2015 IEEE SENSORS; 2015: IEEE; 2015. p. 1-4.

28. Zheng S, Shinzato S, Ogata S, Mao S. Experimental molecular dynamics for individual atomic-scale plastic events in nanoscale crystals. *Journal of the Mechanics and Physics of Solids* 2022, **158:** 104687.

29. Zheng S, Mao SX. In situ atomic-scale observation of dislocation-mediated discrete plasticity in nanoscale crystals. *Material Science & Engineering International Journal* 2021, **5**(3)**:** 93-94.

30. Zhang GP, Volkert CA, Schwaiger R, Wellner P, Arzt E, Kraft O. Length-scale-controlled fatigue mechanisms in thin copper films. *Acta Mater* 2006, **54**(11)**:** 3127-3139.

31. Chen LY, Terrab S, Murphy KF, Sullivan JP, Cheng X, Gianola DS. Temperature controlled tensile testing of individual nanowires. *Review of Scientific Instruments* 2014, **85**(1)**:** 013901.

32. Wang L, Teng J, Sha X, Zou J, Zhang Z, Han X. Plastic deformation through dislocation saturation in ultrasmall Pt nanocrystals and its in situ atomistic mechanisms. *Nano letters* 2017, **17**(8)**:** 4733-4739.

33. Lu Y, Xiang S, Xiao L, Wang L, Deng Q, Zhang Z, *et al.* Dislocation "bubble-like-effect" and the ambient temperature super-plastic elongation of body-centred cubic single crystalline molybdenum. *Scientific reports* 2016, **6:** 22937.

34. Luo J, Wang J, Bitzek E, Huang JY, Zheng H, Tong L, *et al.* Size-dependent brittle-to-ductile transition in silica glass nanofibers. *Nano letters* 2016, **16**(1)**:** 105-113.

35. Kong D, Xin T, Sun S, Lu Y, Shu X, Long H, *et al.* Surface Energy Driven Liquid-Drop-Like Pseudoelastic Behaviors and In Situ Atomistic Mechanisms of Small-Sized Face-Centered-Cubic Metals. *Nano letters* 2018, **19**(1)**:** 292-298.

36. Yue Y, Chen N, Li X, Zhang S, Zhang Z, Chen M, *et al.* Crystalline liquid and rubber-like behavior in Cu nanowires. *Nano letters* 2013, **13**(8)**:** 3812-3816.

37. Zhong L, Sansoz F, He Y, Wang C, Zhang Z, Mao SX. Slip-activated surface creep with room-temperature super-elongation in metallic nanocrystals. *Nat Mater* 2017, **16**(4)**:** 439-445.

38. Zhang H, Wang W, Sun J, Zhong L, He L, Sun L. Surface-Condition-Dependent Deformation Mechanisms in Lead Nanocrystals. *Research* 2022, **2022**.

39. Sun J, He L, Lo Y-C, Xu T, Bi H, Sun L, *et al.* Liquid-like pseudoelasticity of sub-10-nm crystalline silver particles. *Nature materials* 2014, **13**(11)**:** 1007-1012.

40. Shan ZW, Mishra RK, Syed Asif SA, Warren OL, Minor AM. Mechanical annealing and source-limited deformation in submicrometre-diameter Ni crystals. *Nat Mater* 2008, **7**(2)**:** 115-119.

41. Wang ZJ, Li QJ, Cui YN, Liu ZL, Ma E, Li J, *et al.* Cyclic deformation leads to defect healing and strengthening of small-volume metal crystals. *Proc Natl Acad Sci U S A* 2015, **112**(44)**:** 13502-13507.

42. Wang X, Zheng S, Shinzato S, Fang Z, He Y, Zhong L, *et al.* Atomistic processes of surface-diffusion-induced abnormal softening in nanoscale metallic crystals. *Nature Communications* 2021, **12**(1)**:** 1-9.

43. Zheng S, Wang X, Tan S, Wang G, Mao SX. Atomistic processes of diffusion-induced unusual compression fracture in metallic nanocrystals. *Mater Res Lett* 2022, **10**(12)**:** 805-812.

44. Kong D, Sun S, Xin T, Xiao L, Sha X, Lu Y, *et al.* Reveal the size effect on the plasticity of ultra-small sized Ag nanowires with in situ atomic-scale microscopy. *Journal of Alloys and Compounds* 2016, **676:** 377-382.

45. Zheng H, Wang J, Huang JY, Wang J, Mao SX. Void-assisted plasticity in Ag nanowires with a single twin structure. *Nanoscale* 2014, **6**(16)**:** 9574-9578.

46. Lee S, Im J, Yoo Y, Bitzek E, Kiener D, Richter G, *et al.* Reversible cyclic deformation mechanism of gold nanowires by twinning–detwinning transition evidenced from in situ TEM. *Nature communications* 2014, **5**(1)**:** 1-10.

47. Greer JR, De Hosson JTM. Plasticity in small-sized metallic systems: Intrinsic versus extrinsic size effect. *Progress in Materials Science* 2011, **56**(6)**:** 654-724.

48. Weinberger CR, Cai W. Plasticity of metal nanowires. *Journal of Materials Chemistry* 2012, **22**(8)**:** 3277-3292.

49. Liang W, Zhou M. Atomistic simulations reveal shape memory of fcc metal nanowires. *Phys Rev B* 2006, **73**(11)**:** 115409.

50. Zhao S, Zhu Q, An X, Wei H, Song K, Mao SX, *et al.* In situ atomistic observation of the deformation mechanism of Au nanowires with twin-twin intersection. *Journal of Materials Science & Technology* 2020, **53:** 118-125.

51. Chen Y, Huang Q, Zhao S, Zhou H, Wang J. Interactions between Dislocations and Penta-Twins in Metallic Nanocrystals. *Metals* 2021, **11**(11)**:** 1775.

52. Zhu Y, Liao X, Wu X. Deformation twinning in nanocrystalline materials. *Progress in Materials Science* 2012, **57**(1)**:** 1-62.

53. Zheng S, Mao SX. Advances in experimental mechanics at atomic scale. *Extreme Mechanics Letters* 2021, **45:** 101284.

54. Xie D, Nie Z, Shinzato S, Yang Y, Liu F, Ogata S, *et al.* Controlled growth of single-crystalline metal nanowires via thermomigration across a nanoscale junction. *Nature communications* 2019, **10**(1)**:** 1-8.

55. Guo W, Wang Z, Li J. Diffusive versus displacive contact plasticity of nanoscale asperities: temperature-and velocity-dependent strongest size. *Nano letters* 2015, **15**(10)**:** 6582-6585.

56. Li J, Sarkar S, Cox WT, Lenosky TJ, Bitzek E, Wang Y. Diffusive molecular dynamics and its application to nanoindentation and sintering. *Phys Rev B* 2011, **84**(5)**:** 054103.

57. Deng C, Sansoz F. Fundamental differences in the plasticity of periodically twinned nanowires in Au, Ag, Al, Cu, Pb and Ni. *Acta Mater* 2009, **57**(20)**:** 6090-6101.

58. Zheng H, Cao A, Weinberger CR, Huang JY, Du K, Wang J, *et al.* Discrete plasticity in sub-10-nm-sized gold crystals. *Nature Communications* 2010, **1**(1)**:** 1-8.

59. Park N-Y, Nam H-S, Cha P-R, Lee S-C. Size-dependent transition of the deformation behavior of Au nanowires. *Nano Research* 2015, **8**(3)**:** 941-947.

60. Wang J, Sansoz F, Huang J, Liu Y, Sun S, Zhang Z, *et al.* Near-ideal theoretical strength in gold nanowires containing angstrom scale twins. *Nat Commun* 2013, **4:** 1742.

61. Li QJ, Xu B, Hara S, Li J, Ma E. Sample-size-dependent surface dislocation nucleation in nanoscale crystals. *Acta Mater* 2018, **145:** 19-29.

62. Jennings AT, Weinberger CR, Lee S-W, Aitken ZH, Meza L, Greer JR. Modeling dislocation nucleation strengths in pristine metallic nanowires under experimental conditions. *Acta Mater* 2013, **61**(6)**:** 2244-2259.

63. Zhu Q, Kong L, Lu H, Huang Q, Chen Y, Liu Y, *et al.* Revealing extreme twin-boundary shear deformability in metallic nanocrystals. *Science advances* 2021, **7**(36)**:** eabe4758.

64. Wang L, Lu Y, Kong D, Xiao L, Sha X, Sun J, *et al.* Dynamic and atomic-scale understanding of the twin thickness effect on dislocation nucleation and propagation activities by in situ bending of Ni nanowires. *Acta Mater* 2015, **90:** 194-203.

65. Tian L, Li J, Sun J, Ma E, Shan Z. Visualizing size-dependent deformation mechanism transition in Sn. *Scientific Reports* 2013, **3**(1)**:** 1-7.

66. Anderson PM, Hirth JP, Lothe J. *Theory of dislocations*, Third edn. Cambridge University Press: New York, USA, 2017.

67. Yamakov V, Wolf D, Phillpot S, Mukherjee A, Gleiter H. Deformation-mechanism map for nanocrystalline metals by molecular-dynamics simulation. *Nature materials* 2004, **3**(1)**:** 43.

68. Schiøtz J, Jacobsen KW. A maximum in the strength of nanocrystalline copper. *Science* 2003, **301**(5638)**:** 1357-1359.

69. Li X, Wei Y, Lu L, Lu K, Gao H. Dislocation nucleation governed softening and maximum strength in nano-twinned metals. *Nature* 2010, **464**(7290)**:** 877.

70. Lu L, Chen X, Huang X, Lu K. Revealing the Maximum Strength in Nanotwinned Copper. *Science* 2009, **323**(5914)**:** 607-610.

71. Lu L, Dao M, Zhu T, Li J. Size dependence of rate-controlling deformation mechanisms in nanotwinned copper. *Scripta Mater* 2009, **60**(12)**:** 1062-1066.

72. Lu L, Schwaiger R, Shan Z, Dao M, Lu K, Suresh S. Nano-sized twins induce high rate sensitivity of flow stress in pure copper. *Acta Mater* 2005, **53**(7)**:** 2169-2179.

73. Lu L, Zhu T, Shen Y, Dao M, Lu K, Suresh S. Stress relaxation and the structure size-dependence of plastic deformation in nanotwinned copper. *Acta Mater* 2009, **57**(17)**:** 5165-5173.

74. Chisholm C, Bei H, Lowry M, Oh J, Asif SS, Warren O, *et al.* Dislocation starvation and exhaustion hardening in Mo alloy nanofibers. *Acta Mater* 2012, **60**(5)**:** 2258-2264.

75. Kiener D, Minor A. Source truncation and exhaustion: insights from quantitative in situ TEM tensile testing. *Nano letters* 2011, **11**(9)**:** 3816-3820.

76. Oh SH, Legros M, Kiener D, Dehm G. In situ observation of dislocation nucleation and escape in a submicrometre aluminium single crystal. *Nature materials* 2009, **8**(2)**:** 95.

77. Shin J, Chen LY, Sanli UT, Richter G, Labat S, Richard M-I, *et al.* Controlling dislocation nucleation-mediated plasticity in nanostructures via surface modification. *Acta Mater* 2019, **166:** 572-586.

78. Weinberger CR, Jennings AT, Kang K, Greer JR. Atomistic simulations and continuum modeling of dislocation nucleation and strength in gold nanowires. *Journal of the Mechanics and Physics of Solids* 2012, **60**(1)**:** 84-103.

79. Zheng H, Cao A, Weinberger CR, Huang JY, Du K, Wang J, *et al.* Discrete plasticity in sub-10-nm-sized gold crystals. *Nature Communications* 2010, **1**.

80. Zhu T, Li J. Ultra-strength materials. *Progress in Materials Science* 2010, **55**(7)**:** 710-757.

81. Li QJ, Ma E. When 'smaller is stronger' no longer holds. *Mater Res Lett* 2018, **6**(5)**:** 283-292.

82. Brune H, Bromann K, Röder H, Kern K, Jacobsen J, Stoltze P, *et al.* Effect of strain on surface diffusion and nucleation. *Phys Rev B* 1995, **52**(20)**:** R14380.

83. Göbel H, Von Blanckenhagen P. A study of surface diffusion on gold with an atomic force microscope. *Surf Sci* 1995, **331:** 885-890.

84. Li Q, Xu B, Hara S, Li J, Ma E. Sample-size-dependent surface dislocation nucleation in nanoscale crystals. *Acta Mater* 2018, **145:** 19-29.

85. Chachamovitz D, Mordehai D. The Stress-Dependent Activation Parameters for Dislocation Nucleation in Molybdenum Nanoparticles. *Scientific reports* 2018, **8**(1)**:** 1-10.

86. Diao J, Gall K, Dunn ML, Zimmerman JA. Atomistic simulations of the yielding of gold nanowires. *Acta Mater* 2006, **54**(3)**:** 643-653.

87. Diao J, Gall K, Dunn ML. Yield strength asymmetry in metal nanowires. *Nano Letters* 2004, **4**(10)**:** 1863-1867.

88. Sun J, He L, Lo YC, Xu T, Bi H, Sun L, *et al.* Liquid-like pseudoelasticity of sub-10-nm crystalline silver particles. *Nat Mater* 2014, **13**(11)**:** 1007-1012.

89. Strachan DR, Smith DE, Fischbein MD, Johnston DE, Guiton BS, Drndić M, *et al.* Clean electromigrated nanogaps imaged by transmission electron microscopy. *Nano letters* 2006, **6**(3)**:** 441-444.

90. Wang B, Han Y, Xu S, Qiu L, Ding F, Lou J, *et al.* Mechanically Assisted Self‐Healing of Ultrathin Gold Nanowires. *Small* 2018, **14**(20)**:** 1704085.

91. Rodrigues V, Fuhrer T, Ugarte D. Signature of atomic structure in the quantum conductance of gold nanowires. *Physical review letters* 2000, **85**(19)**:** 4124.

92. Shan Z, Stach E, Wiezorek J, Knapp J, Follstaedt D, Mao S. Grain boundary-mediated plasticity in nanocrystalline nickel. *Science* 2004, **305**(5684)**:** 654-657.

93. Shan Z, Wiezorek JK, Stach E, Follstaedt D, Knapp J, Mao S. Dislocation dynamics in nanocrystalline nickel. *Physical review letters* 2007, **98**(9)**:** 095502.

94. Wolf D, Yamakov V, Phillpot S, Mukherjee A, Gleiter H. Deformation of nanocrystalline materials by molecular-dynamics simulation: relationship to experiments? *Acta Mater* 2005, **53**(1)**:** 1-40.

95. Sun S, Kong D, Li D, Liao X, Liu D, Mao S, *et al.* Atomistic Mechanism of Stress-Induced Combined Slip and Diffusion in Sub-5 Nanometer-Sized Ag Nanowires. *ACS nano* 2019, **13**(8)**:** 8708-8716.

96. Cao G, Wang J, Du K, Wang X, Li J, Zhang Z, *et al.* Superplasticity in Gold Nanowires through the Operation of Multiple Slip Systems. *Advanced Functional Materials* 2018, **28**(51)**:** 1805258.

97. Wang J, Wang Y, Cai W, Li J, Zhang Z, Mao SX. Discrete shear band plasticity through dislocation activities in body-centered cubic tungsten nanowires. *Scientific Reports* 2018, **8**(1)**:** 1-8.

98. Yue Y, Liu P, Zhang Z, Han X, Ma E. Approaching the theoretical elastic strain limit in copper nanowires. *Nano letters* 2011, **11**(8)**:** 3151-3155.

99. Lu L, Shen YF, Chen XH, Qian LH, Lu K. Ultrahigh strength and high electrical conductivity in copper. *Science* 2004, **304**(5669)**:** 422-426.

100. Frøseth A, Van Swygenhoven H, Derlet P. The influence of twins on the mechanical properties of nc-Al. *Acta Mater* 2004, **52**(8)**:** 2259-2268.

101. Chen M, Ma E, Hemker KJ, Sheng H, Wang Y, Cheng X. Deformation twinning in nanocrystalline aluminum. *Science* 2003, **300**(5623)**:** 1275-1277.

102. Liao X, Zhou F, Lavernia E, Srinivasan S, Baskes M, He D, *et al.* Deformation mechanism in nanocrystalline Al: Partial dislocation slip. *Applied Physics Letters* 2003, **83**(4)**:** 632-634.

103. Liao X, Srinivasan S, Zhao Y, Baskes M, Zhu Y, Zhou F, *et al.* Formation mechanism of wide stacking faults in nanocrystalline Al. *Applied physics letters* 2004, **84**(18)**:** 3564-3566.

104. Van Swygenhoven H, Derlet PM, Frøseth A. Stacking fault energies and slip in nanocrystalline metals. *Nature materials* 2004, **3**(6)**:** 399.

105. Kibey S, Liu J, Johnson D, Sehitoglu H. Predicting twinning stress in fcc metals: Linking twin-energy pathways to twin nucleation. *Acta Mater* 2007, **55**(20)**:** 6843-6851.

106. Li BQ, Sui ML, Li B, Ma E, Mao SX. Reversible twinning in pure aluminum. *Phys Rev Lett* 2009, **102**(20)**:** 205504.

107. Wang J, Li N, Anderoglu O, Zhang X, Misra A, Huang J, *et al.* Detwinning mechanisms for growth twins in face-centered cubic metals. *Acta Mater* 2010, **58**(6)**:** 2262-2270.

108. Wu X, Qi Y, Zhu Y. Partial-mediated slips in nanocrystalline Ni at high strain rate. *Applied physics letters* 2007, **90**(22)**:** 221911.

109. Liao X, Zhao Y, Srinivasan S, Zhu Y, Valiev R, Gunderov D. Deformation twinning in nanocrystalline copper at room temperature and low strain rate. *Applied physics letters* 2004, **84**(4)**:** 592-594.

110. Wu X, Zhu Y, Chen M, Ma E. Twinning and stacking fault formation during tensile deformation of nanocrystalline Ni. *Scripta Mater* 2006, **54**(9)**:** 1685-1690.

111. Zhu Y, Liao X, Srinivasan S, Zhao Y, Baskes M, Zhou F, *et al.* Nucleation and growth of deformation twins in nanocrystalline aluminum. *Applied physics letters* 2004, **85**(21)**:** 5049-5051.

112. Wu X, Zhu Y. Inverse grain-size effect on twinning in nanocrystalline Ni. *Physical review letters* 2008, **101**(2)**:** 025503.

113. Seo J-H, Yoo Y, Park N-Y, Yoon S-W, Lee H, Han S, *et al.* Superplastic deformation of defect-free Au nanowires via coherent twin propagation. *Nano Letters* 2011, **11**(8)**:** 3499-3502.

114. Seo J-H, Park HS, Yoo Y, Seong T-Y, Li J, Ahn J-P, *et al.* Origin of size dependency in coherent-twin-propagation-mediated tensile deformation of noble metal nanowires. *Nano letters* 2013, **13**(11)**:** 5112-5116.

115. Li B, Li B, Wang Y, Sui M, Ma E. Twinning mechanism via synchronized activation of partial dislocations in face-centered-cubic materials. *Scripta Mater* 2011, **64**(9)**:** 852-855.

116. Seo JH, Yoo Y, Park NY, Yoon SW, Lee H, Han S, *et al.* Superplastic deformation of defect-free Au nanowires via coherent twin propagation. *Nano Lett* 2011, **11**(8)**:** 3499-3502.

117. Sedlmayr A, Bitzek E, Gianola DS, Richter G, Mönig R, Kraft O. Existence of two twinning-mediated plastic deformation modes in Au nanowhiskers. *Acta Mater* 2012, **60**(9)**:** 3985-3993.

118. Kim H-K, Kim S-H, Ahn J-P, Lee J-C. Deformation criterion for face-centered-cubic metal nanowires. *Materials Science and Engineering: A* 2018, **736:** 431-437.

119. Kim S-H, Kim H-K, Seo J-H, Whang D-M, Ahn J-P, Lee J-C. Deformation twinning of ultrahigh strength aluminum nanowire. *Acta Mater* 2018, **160:** 14-21.

120. Wang L, Guan P, Teng J, Liu P, Chen D, Xie W, *et al.* New twinning route in face-centered cubic nanocrystalline metals. *Nature communications* 2017, **8**(1)**:** 2142.

121. Arakawa K, Ono K, Isshiki M, Mimura K, Uchikoshi M, Mori H. Observation of the one-dimensional diffusion of nanometer-sized dislocation loops. *Science* 2007, **318**(5852)**:** 956-959.

122. Sainath G, Goyal S, Nagesha A. Atomistic mechanisms of twin–twin interactions in Cu nanopillars. *Computational Materials Science* 2020, **185:** 109950.

123. Liao X, Huang J, Zhu Y, Zhou F, Lavernia E. Nanostructures and deformation mechanisms in a cryogenically ball-milled Al-Mg alloy. *Philos Mag* 2003, **83**(26)**:** 3065-3075.

124. An X, Lin Q, Wu S, Zhang Z, Figueiredo R, Gao N, *et al.* Formation of fivefold deformation twins in an ultrafine-grained copper alloy processed by high-pressure torsion. *Scripta Mater* 2011, **64**(3)**:** 249-252.

125. Zhu Y, Liao X, Valiev R. Formation mechanism of fivefold deformation twins in nanocrystalline face-centered-cubic metals. *Applied physics letters* 2005, **86**(10)**:** 103112.

126. Cao A, Wei Y. Formation of fivefold deformation twins in nanocrystalline face-centered-cubic copper based on molecular dynamics simulations. *Applied physics letters* 2006, **89**(4)**:** 041919.

127. Shao Y, Wang S. Quasicontinuum study on formation of fivefold deformation twin in nanocrystalline aluminum. *Scripta Mater* 2010, **62**(6)**:** 419-422.

128. Zhang Z, Huang S, Chen L, Zhu Z, Guo D. Formation mechanism of fivefold deformation twins in a face-centered cubic alloy. *Scientific reports* 2017, **7**(1)**:** 1-7.

129. Huang P, Dai G, Wang F, Xu K, Li Y. Fivefold annealing twin in nanocrystalline Cu. *Applied Physics Letters* 2009, **95**(20)**:** 203101.

130. Cao Z, Xu L, Sun W, Shi J, Wei M, Pan G, *et al.* Size dependence and associated formation mechanism of multiple-fold annealing twins in nanocrystalline Cu. *Acta Mater* 2015, **95:** 312-323.

131. Bringa EM, Farkas D, Caro A, Wang Y, McNaney J, Smith R. Fivefold twin formation during annealing of nanocrystalline Cu. *Scripta Mater* 2008, **59**(12)**:** 1267-1270.

132. Thomas SL, King AH, Srolovitz DJ. When twins collide: Twin junctions in nanocrystalline nickel. *Acta Mater* 2016, **113:** 301-310.

133. Zhu T, Li J, Samanta A, Leach A, Gall K. Temperature and strain-rate dependence of surface dislocation nucleation. *Physical Review Letters* 2008, **100**(2)**:** 025502.

134. Fan Y, Osetsky YN, Yip S, Yildiz B. Onset mechanism of strain-rate-induced flow stress upturn. *Physical review letters* 2012, **109**(13)**:** 135503.

135. Marichal C, Van Swygenhoven H, Van Petegem S, Borca C. {110} Slip with {112} slip traces in bcc Tungsten. *Scientific reports* 2013, **3**(1)**:** 1-7.

136. Min Han S, Feng G, Young Jung J, Joon Jung H, Groves JR, Nix WD, *et al.* Critical-temperature/Peierls-stress dependent size effects in body centered cubic nanopillars. *Applied Physics Letters* 2013, **102**(4)**:** 041910.

137. Caillard D. Kinetics of dislocations in pure Fe. Part I. In situ straining experiments at room temperature. *Acta Mater* 2010, **58**(9)**:** 3493-3503.

138. Hagen A, Thaulow C. Low temperature in-situ micro-compression testing of iron pillars. *Materials Science and Engineering: A* 2016, **678:** 355-364.

139. Abad OT, Wheeler JM, Michler J, Schneider AS, Arzt E. Temperature-dependent size effects on the strength of Ta and W micropillars. *Acta Mater* 2016, **103:** 483-494.

140. Xie KY, Shrestha S, Cao Y, Felfer PJ, Wang Y, Liao X, *et al.* The effect of pre-existing defects on the strength and deformation behavior of α-Fe nanopillars. *Acta Mater* 2013, **61**(2)**:** 439-452.

141. Weinberger CR, Boyce BL, Battaile CC. Slip planes in bcc transition metals. *International Materials Reviews* 2013, **58**(5)**:** 296-314.

142. Chisholm C, Bei H, Lowry MB, Oh J, Asif SAS, Warren OL, *et al.* Dislocation starvation and exhaustion hardening in Mo alloy nanofibers. *Acta Mater* 2012, **60**(5)**:** 2258-2264.

143. Wang J, Zeng Z, Weinberger CR, Zhang Z, Zhu T, Mao SX. In situ atomic-scale observation of twinning-dominated deformation in nanoscale body-centred cubic tungsten. *Nature Materials* 2015, **14**(6)**:** 594-600.

144. Wang J, Faisal AH, Li X, Hong Y, Zhu Q, Bei H, *et al.* Discrete twinning dynamics and size-dependent dislocation-to twin transition in body-centred cubic tungsten. *Journal of Materials Science & Technology* 2022, **106:** 33-40.

145. Wang Q, Wang J, Li J, Zhang Z, Mao SX. Consecutive crystallographic reorientations and superplasticity in body-centered cubic niobium nanowires. *Science Advances* 2018, **4**(7)**:** eaas8850.

146. Wang J, Zeng Z, Wen M, Wang Q, Chen D, Zhang Y, *et al.* Anti-twinning in nanoscale tungsten. *Science Advances* 2020, **6**(23)**:** eaay2792.

147. Meyers MA, Chawla KK. *Mechanical behavior of materials*, 2 edn. Cambridge University Press: Cambridge, 2008.

148. Roos B, Kapelle B, Richter G, Volkert C. Surface dislocation nucleation controlled deformation of Au nanowires. *Applied Physics Letters* 2014, **105**(20)**:** 201908.

149. Yue Y, Liu P, Deng Q, Ma E, Zhang Z, Han X. Quantitative evidence of crossover toward partial dislocation mediated plasticity in copper single crystalline nanowires. *Nano Lett* 2012, **12**(8)**:** 4045-4049.

150. Oh SH, Legros M, Kiener D, Gruber P, Dehm G. In situ TEM straining of single crystal Au films on polyimide: Change of deformation mechanisms at the nanoscale. *Acta Mater* 2007, **55**(16)**:** 5558-5571.

151. Hwang B, Kang M, Lee S, Weinberger CR, Loya P, Lou J, *et al.* Effect of surface energy on size-dependent deformation twinning of defect-free Au nanowires. *Nanoscale* 2015, **7**(38)**:** 15657-15664.

152. Yin S, Cheng G, Richter G, Gao H, Zhu Y. Transition of Deformation Mechanisms in Single-Crystalline Metallic Nanowires. *ACS nano* 2019, **13**(8)**:** 9082-9090.

153. Xu K, Niu L-L, Jin S, Shu X, Xie H, Wang L, *et al.* Atomistic simulations of screw dislocations in bcc tungsten: From core structures and static properties to interaction with vacancies. *Nuclear Instruments and Methods in Physics Research Section B: Beam Interactions with Materials and Atoms* 2017, **393:** 174-179.

154. Dezerald L, Rodney D, Clouet E, Ventelon L, Willaime F. Plastic anisotropy and dislocation trajectory in BCC metals. *Nature communications* 2016, **7**(1)**:** 1-7.

155. Po G, Cui Y, Rivera D, Cereceda D, Swinburne TD, Marian J, *et al.* A phenomenological dislocation mobility law for bcc metals. *Acta Mater* 2016, **119:** 123-135.

156. Kotrechko S, Ovsjannikov O, Stetsenko N, Mikhailovskij I, Mazilova T, Starostenkov M. Yield strength temperature dependence of tungsten nanosized crystals: experiment and simulation. *Philos Mag* 2016, **96**(5)**:** 473-485.

157. Narayanan S, McDowell DL, Zhu T. Crystal plasticity model for BCC iron atomistically informed by kinetics of correlated kinkpair nucleation on screw dislocation. *Journal of the Mechanics and Physics of Solids* 2014, **65:** 54-68.

158. Wei S, Wang Q, Wei H, Wang J. Bending-induced deformation twinning in body-centered cubic tungsten nanowires. *Mater Res Lett* 2019, **7**(5)**:** 210-216.

159. Sainath G, Choudhary BK. Orientation dependent deformation behaviour of BCC iron nanowires. *Computational Materials Science* 2016, **111:** 406-415.

160. Feng Y-X, Shang J-X, Qin S-J, Lu G-H, Chen Y. Twin and dislocation mechanisms in tensile W single crystal with temperature change: a molecular dynamics study. *Physical Chemistry Chemical Physics* 2018, **20**(26)**:** 17727-17738.

161. Li SZ, Ding XD, Deng JK, Lookman T, Li J, Ren XB, *et al.* Superelasticity in bcc nanowires by a reversible twinning mechanism. *Phys Rev B* 2010, **82**(20)**:** 205435.

162. Zheng YG, Zhang HW, Chen Z, Wang L, Zhang ZQ, Wang JB. Formation of two conjoint fivefold deformation twins in copper nanowires with molecular dynamics simulation. *Applied Physics Letters* 2008, **92**(4)**:** 041913.

163. Bringa EM, Farkas D, Caro A, Wang YM, McNaney J, Smith R. Fivefold twin formation during annealing of nanocrystalline Cu. *Scripta Materialia* 2008, **59**(12)**:** 1267-1270.

164. Niu JJ, Zhang P, Wang RH, Zhang JY, Liu G, Zhang GJ, *et al.* Formation of multiple twins and their strengthening effect in nanocrystalline Cu/Zr multilayer films. *Materials Science and Engineering: A* 2012, **539:** 68-73.

165. Wu J, Nagao S, He J, Zhang Z. Role of five-fold twin boundary on the enhanced mechanical properties of fcc Fe nanowires. *Nano letters* 2011, **11**(12)**:** 5264-5273.

166. Chang T-H, Cheng G, Li C, Zhu Y. On the size-dependent elasticity of penta-twinned silver nanowires. *Extreme Mechanics Letters* 2016, **8:** 177-183.

167. Wu B, Heidelberg A, Boland JJ, Sader JE, Sun X, Li Y. Microstructure-hardened silver nanowires. *Nano letters* 2006, **6**(3)**:** 468-472.

168. Schwaiger R, Kraft O. High cycle fatigue of thin silver films investigated by dynamic microbeam deflection. *Scripta Mater* 1999, **41**(8)**:** 823-829.

169. Zhang X, He Y, Sushko ML, Liu J, Luo L, De Yoreo JJ, *et al.* Direction-specific van der Waals attraction between rutile TiO2 nanocrystals. *Science* 2017, **356**(6336)**:** 434-437.

170. Wang J, Sansoz F, Deng C, Xu G, Han G, Mao SX. Strong Hall-Petch Type Behavior in the Elastic Strain Limit of Nanotwinned Gold Nanowires. *Nano Letters* 2015, **15**(6)**:** 3865-3870.

171. Zhu Y, Qin Q, Xu F, Fan F, Ding Y, Zhang T, *et al.* Size effects on elasticity, yielding, and fracture of silver nanowires: In situ experiments. *Phys Rev B* 2012, **85**(4)**:** 045443.

172. Lu Y, Lou J. Quantitative in-situ nanomechanical characterization of metallic nanowires. *Jom* 2011, **63**(9)**:** 35-42.

173. Cheng G, Miao C, Qin Q, Li J, Xu F, Haftbaradaran H, *et al.* Large anelasticity and associated energy dissipation in single-crystalline nanowires. *Nature nanotechnology* 2015, **10**(8)**:** 687-691.

174. Richter G, Hillerich K, Gianola DS, Monig R, Kraft O, Volkert CA. Ultrahigh strength single crystalline nanowhiskers grown by physical vapor deposition. *Nano Letters* 2009, **9**(8)**:** 3048-3052.

175. Wang LH, Xin TJ, Kong DL, Shu XY, Chen YH, Zhou H, *et al.* In situ observation of stress induced grain boundary migration in nanocrystalline gold. *Scripta Mater* 2017, **134:** 95-99.

176. Legros M, Gianola DS, Hemker KJ. In situ TEM observations of fast grain-boundary motion in stressed nanocrystalline aluminum films. *Acta Mater* 2008, **56**(14)**:** 3380-3393.

177. Wang L, Teng J, Liu P, Hirata A, Ma E, Zhang Z, *et al.* Grain rotation mediated by grain boundary dislocations in nanocrystalline platinum. *Nat Commun* 2014, **5**(1)**:** 1-7.

178. Kraft O, Hommel M, Arzt E. X-ray diffraction as a tool to study the mechanical behaviour of thin films. *Mat Sci Eng a-Struct* 2000, **288**(2)**:** 209-216.

179. Legros M, Gianola D, Motz C. Quantitative in situ mechanical testing in electron microscopes. *MRS bulletin* 2010, **35**(5)**:** 354-360.

180. Kiener D, Motz C, Rester M, Jenko M, Dehm G. FIB damage of Cu and possible consequences for miniaturized mechanical tests. *Materials Science and Engineering: A* 2007, **459**(1-2)**:** 262-272.

181. Espinosa HD, Bernal RA, Filleter T. In situ TEM electromechanical testing of nanowires and nanotubes. *Small* 2012, **8**(21)**:** 3233-3252.

182. Ramachandramoorthy R, Bernal R, Espinosa HD. Pushing the envelope of in situ transmission electron microscopy. *ACS nano* 2015, **9**(5)**:** 4675-4685.

183. Yu Q, Legros M, Minor A. In situ TEM nanomechanics. *Mrs Bulletin* 2015, **40**(1)**:** 62-70.

184. Ohmura T, Minor A, Stach E, Morris J. Dislocation–grain boundary interactions in martensitic steel observed through in situ nanoindentation in a transmission electron microscope. *J Mater Res* 2004, **19**(12)**:** 3626-3632.

185. Bobji M, Ramanujan C, Pethica J, Inkson B. A miniaturized TEM nanoindenter for studying material deformation in situ. *Measurement Science and Technology* 2006, **17**(6)**:** 1324.

186. Chang T-H, Zhu Y. A microelectromechanical system for thermomechanical testing of nanostructures. *Applied Physics Letters* 2013, **103**(26)**:** 263114.

187. Kang W, Saif MTA. A novel SiC MEMS apparatus for in situ uniaxial testing of micro/nanomaterials at high temperature. *Journal of Micromechanics and Microengineering* 2011, **21**(10)**:** 105017.

188. Lu Y, Huang JY, Wang C, Sun S, Lou J. Cold welding of ultrathin gold nanowires. *Nature nanotechnology* 2010, **5**(3)**:** 218.

189. Wang L, Han X, Liu P, Yue Y, Zhang Z, Ma E. In situ observation of dislocation behavior in nanometer grains. *Physical review letters* 2010, **105**(13)**:** 135501.

190. Wang L, Teng J, Liu P, Hirata A, Ma E, Zhang Z, *et al.* Grain rotation mediated by grain boundary dislocations in nanocrystalline platinum. *Nat Commun* 2014, **5:** 4402.

191. Wang L, Teng J, Wu Y, Sha X, Xiang S, Mao S, *et al.* In situ atomic scale mechanisms of strain-induced twin boundary shear to high angle grain boundary in nanocrystalline Pt. *Ultramicroscopy* 2018, **195:** 69-73.

192. Wang L, Teng J, Wu Y, Zou J, Yu G, Zhang Z, *et al.* Size dependence of dislocation activities and independence on theoretical elastic strain limit in Pt nanocrystals revealed by atomic-resolution in situ investigation. *Materials Today Nano* 2018, **2:** 1-6.

193. Qin Q, Yin S, Cheng G, Li X, Chang T-H, Richter G, *et al.* Recoverable plasticity in penta-twinned metallic nanowires governed by dislocation nucleation and retraction. *Nature communications* 2015, **6**(1)**:** 1-8.

194. Kim SY, Lee I-H, Jun S. Transition-pathway models of atomic diffusion on fcc metal surfaces. I. Flat surfaces. *Phys Rev B* 2007, **76**(24)**:** 245407.

195. Kim SY, Lee I-H, Jun S. Transition-pathway models of atomic diffusion on fcc metal surfaces. II. Stepped surfaces. *Phys Rev B* 2007, **76**(24)**:** 245408.

196. Zhao S, Zhu Q, Song K, Zhou H, Wang J. Role of intersecting grain boundary on the deformation of twin-twin intersection. *Scripta Mater* 2020, **188:** 184-189.

197. Chen Y, Zhao S, Huang Q, Zhu Q, Song K, Zhou H, *et al.* A geometrical model for grain boundary migration mediated formation of multifold twins. *International Journal of Plasticity* 2021, **148:** 103128.

198. Chen Y, Huang Q, Zhao S, Zhou H, Wang J. Penta-Twin Destruction by Coordinated Twin Boundary Deformation. *Nano Letters* 2021, **21**(19)**:** 8378-8384.

199. Nam S-W, Chung H-S, Lo YC, Qi L, Li J, Lu Y, *et al.* Electrical wind force–driven and dislocation-templated amorphization in phase-change nanowires. *Science* 2012, **336**(6088)**:** 1561-1566.

200. Zhu Q, Cao G, Wang J, Deng C, Li J, Zhang Z, *et al.* In situ atomistic observation of disconnection-mediated grain boundary migration. *Nature communications* 2019, **10**(1)**:** 156.

201. Zhu Q, Huang Q, Guang C, An X, Mao SX, Yang W, *et al.* Metallic nanocrystals with low angle grain boundary for controllable plastic reversibility. *Nature communications* 2020, **11**(1)**:** 1-8.

202. Zhu Q, Zhao S, Deng C, An X, Song K, Mao SX, *et al.* In situ atomistic observation of grain boundary migration subjected to defect interaction. *Acta Mater* 2020.

203. Chen Y, Huang Q, Zhu Q, Song K, Zhou Y, Zhou H, *et al.* Coordinated grain boundary deformation governed nanograin annihilation in shear cycling. *Journal of Materials Science & Technology* 2021, **86:** 180-191.

204. Zhong L, Wang J, Sheng H, Zhang Z, Mao SX. Formation of monatomic metallic glasses through ultrafast liquid quenching. *Nature* 2014, **512**(7513)**:** 177-+.

205. Thompson AP, Aktulga HM, Berger R, Bolintineanu DS, Brown WM, Crozier PS, *et al.* LAMMPS-a flexible simulation tool for particle-based materials modeling at the atomic, meso, and continuum scales. *Computer Physics Communications* 2022, **271:** 108171.

206. Grochola G, Russo SP, Snook IK. On fitting a gold embedded atom method potential using the force matching method. *The Journal of chemical physics* 2005, **123**(20)**:** 204719.

207. Wang J, Sansoz F, Huang J, Liu Y, Sun S, Zhang Z, *et al.* Near-ideal theoretical strength in gold nanowires containing angstrom scale twins. *Nature Communications* 2013, **4**(1)**:** 1-8.

208. Stukowski A. Visualization and analysis of atomistic simulation data with OVITO–the Open Visualization Tool. *Modelling and simulation in materials science and engineering* 2009, **18**(1)**:** 015012.

209. Cheung KS, Yip S. Atomic‐level stress in an inhomogeneous system. *J Appl Phys* 1991, **70**(10)**:** 5688-5690.

210. Hirel P. Atomsk: A tool for manipulating and converting atomic data files. *Computer Physics Communications* 2015, **197:** 212-219.

211. Nosé S. A unified formulation of the constant temperature molecular dynamics methods. *The Journal of chemical physics* 1984, **81**(1)**:** 511-519.

212. Hoover WG. Canonical dynamics: Equilibrium phase-space distributions. *Physical review A* 1985, **31**(3)**:** 1695.

213. Loh OY, Espinosa HD. Nanoelectromechanical contact switches. *Nature nanotechnology* 2012, **7**(5)**:** 283-295.

214. Gao W, Emaminejad S, Nyein HYY, Challa S, Chen K, Peck A, *et al.* Fully integrated wearable sensor arrays for multiplexed in situ perspiration analysis. *Nature* 2016, **529**(7587)**:** 509-514.

215. Gong S, Schwalb W, Wang Y, Chen Y, Tang Y, Si J, *et al.* A wearable and highly sensitive pressure sensor with ultrathin gold nanowires. *Nature communications* 2014, **5**(1)**:** 1-8.

216. Yin S, Cheng G, Zhu Y, Gao H. Competition between shear localization and tensile detwinning in twinned nanowires. *Physical Review Materials* 2020, **4**(2)**:** 023603.

217. Ramachandramoorthy R, Wang Y, Aghaei A, Richter G, Cai W, Espinosa HD. Reliability of single crystal silver nanowire-based systems: stress assisted instabilities. *ACS nano* 2017, **11**(5)**:** 4768-4776.

218. Chen LY, He MR, Shin J, Richter G, Gianola DS. Measuring surface dislocation nucleation in defect-scarce nanostructures. *Nat Mater* 2015, **14**(7)**:** 707-713.

219. Tian L, Li J, Sun J, Ma E, Shan Z-W. Visualizing size-dependent deformation mechanism transition in Sn. *Sci Rep* 2013, **3:** 2113.

220. Sun J, He L, Lo Y-C, Xu T, Bi H, Sun L, *et al.* Liquid-like pseudoelasticity of sub-10-nm crystalline silver particles. *Nature materials* 2014, **13**(11)**:** 1007.

221. Zhong L, Sansoz F, He Y, Wang C, Zhang Z, Mao SX. Slip-activated surface creep with room-temperature super-elongation in metallic nanocrystals. *Nature materials* 2017, **16**(4)**:** 439-445.

222. Li P, Han Y, Zhou X, Fan Z, Xu S, Cao K, *et al.* Thermal effect and Rayleigh instability of ultrathin 4H hexagonal gold nanoribbons. *Matter* 2020, **2**(3)**:** 658-665.

223. Egerton RF, Wang F, Crozier PA. Beam-induced damage to thin specimens in an intense electron probe. *Microscopy and Microanalysis* 2006, **12**(1)**:** 65.

224. Hummel R, Geier H. Activation energy for electrotransport in thin silver and gold films. *Thin Solid Films* 1975, **25**(2)**:** 335-342.

225. Ala-Nissila T, Ferrando R, Ying SJAiP. Collective and single particle diffusion on surfaces. 2002, **51**(3)**:** 949-1078.

226. Egerton R, Li P, Malac M. Radiation damage in the TEM and SEM. *Micron* 2004, **35**(6)**:** 399-409.

227. Takahashi Y, Suzuki A, Furutaku S, Yamauchi K, Kohmura Y, Ishikawa T. Bragg x-ray ptychography of a silicon crystal: Visualization of the dislocation strain field and the production of a vortex beam. *Phys Rev B* 2013, **87**(12)**:** 121201.

228. Wang B, Liu M, Wang Y, Chen X. Structures and energetics of silver and gold nanoparticles. *The Journal of Physical Chemistry C* 2011, **115**(23)**:** 11374-11381.

229. Cao K, Han Y, Zhang H, Gao L, Yang H, Chen J, *et al.* Size-dependent fracture behavior of silver nanowires. *Nanotechnology* 2018, **29**(29)**:** 295703.

230. Greer JR, Weinberger CR, Cai W. Comparing the strength of fcc and bcc sub-micrometer pillars: Compression experiments and dislocation dynamics simulations. *Materials Science and Engineering: A* 2008, **493**(1-2)**:** 21-25.

231. Brinckmann S, Kim J-Y, Greer JR. Fundamental differences in mechanical behavior between two types of crystals at the nanoscale. *Physical review letters* 2008, **100**(15)**:** 155502.

232. Kim JY, Jong DC, Greer JR. Tensile and compressive behavior of tungsten, molybdenum, tantalum and niobium at the nanoscale. *Acta Mater* 2010, **58**(7)**:** 2355-2363.

233. Huang L, Li Q-J, Shan Z-W, Li J, Sun J, Ma E. A new regime for mechanical annealing and strong sample-size strengthening in body centred cubic molybdenum. *Nature communications* 2011, **2**(1)**:** 1-6.

234. Schneider AS, Kaufmann D, Clark BG, Frick CP, Gruber PA, Monig R, *et al.* Correlation between Critical Temperature and Strength of Small-Scale bcc Pillars. *Physical Review Letters* 2009, **103**(10)**:** 105501.

235. Uchic MD, Dimiduk DM, Florando JN, Nix WD. Sample dimensions influence strength and crystal plasticity. *Science* 2004, **305**(5686)**:** 986-989.

236. Hong MH, Samant A, Pirouz P. Stacking fault energy of 6H-SiC and 4H-SiC single crystals. *Philosophical Magazine A* 2000, **80**(4)**:** 919-935.

237. Wu Z, Zhang YW, Jhon MH, Gao H, Srolovitz DJ. Nanowire failure: long = brittle and short = ductile. *Nano Lett* 2012, **12**(2)**:** 910-914.

238. Torres J, Tosatti E, Dal Corso A, Ercolessi F, Kohanoff J, Di Tolla F, *et al.* The puzzling stability of monatomic gold wires. *Surf Sci* 1999, **426**(3)**:** L441-L446.

239. Vitos L, Ruban A, Skriver HL, Kollár J. The surface energy of metals. *Surf Sci* 1998, **411**(1-2)**:** 186-202.

240. Mishra S, Gupta SK, Jha PK, Pratap A. Study of dimension dependent diffusion coefficient of titanium dioxide nanoparticles. *Materials Chemistry and Physics* 2010, **123**(2-3)**:** 791-794.

241. Guisbiers G, Kazan M, Van Overschelde O, Wautelet M, Pereira S. Mechanical and thermal properties of metallic and semiconductive nanostructures. *The Journal of Physical Chemistry C* 2008, **112**(11)**:** 4097-4103.

242. Dick K, Dhanasekaran T, Zhang Z, Meisel D. Size-dependent melting of silica-encapsulated gold nanoparticles. *Journal of the American Chemical Society* 2002, **124**(10)**:** 2312-2317.

243. Luo X, Li X, Zhang G. Forming incoherent twin boundaries: a new way for nanograin growth under cyclic loading. *Mater Res Lett* 2016, **5**(2)**:** 95-101.

244. Wang X, Wang J, He Y, Wang C, Zhong L, Mao SX. Unstable twin in body-centered cubic tungsten nanocrystals. *Nature communications* 2020, **11**(1)**:** 1-7.

245. Huang Q, Yu D, Xu B, Hu W, Ma Y, Wang Y, *et al.* Nanotwinned diamond with unprecedented hardness and stability. *Nature* 2014, **510**(7504)**:** 250-253.

246. Song M, Zhou G, Lu N, Lee J, Nakouzi E, Wang H, *et al.* Oriented attachment induces fivefold twins by forming and decomposing high-energy grain boundaries. *Science* 2020, **367**(6473)**:** 40-45.

247. Marks L, Smith DJ. High resolution studies of small particles of gold and silver: I. Multiply-twinned particles. *Journal of Crystal Growth* 1981, **54**(3)**:** 425-432.

248. Parajuli P, Mendoza-Cruz R, Velazquez-Salazar JJ, Yacaman MJ, Ponce A. Fivefold annealing twin in nanocrystalline Au/Pd film. *Mater Lett* 2019, **244:** 88-91.

249. Narayanan S, Cheng G, Zeng Z, Zhu Y, Zhu T. Strain hardening and size effect in five-fold twinned Ag nanowires. *Nano letters* 2015, **15**(6)**:** 4037-4044.

250. Xie Z, Shin J, Renner J, Prakash A, Gianola DS, Bitzek E. Origins of strengthening and failure in twinned Au nanowires: Insights from in− situ experiments and atomistic simulations. *Acta Mater* 2020, **187:** 166-175.

251. Yue Y, Zhang Q, Yang Z, Gong Q, Guo L. Study of the mechanical behavior of radially grown fivefold twinned nanowires on the atomic scale. *small* 2016, **12**(26)**:** 3503-3509.

252. Zheng H, Wang J, Huang JY, Cao A, Mao SX. In Situ Visualization of Birth and Annihilation of Grain Boundaries in an Au Nanocrystal. *Physical Review Letters* 2012, **109**(22)**:** 225501.

253. Hÿtch M, Snoeck E, Kilaas R. Quant itative measurement of displacement and strain fields from HREM micrographs. *Ultramicroscopy* 1998, **74**(3)**:** 131-146.

254. Rohith P, Sainath G, Choudhary B. Effect of orientation and mode of loading on deformation behaviour of Cu nanowires. *Computational Condensed Matter* 2018, **17:** e00330.

255. Randle V. Mechanism of twinning-induced grain boundary engineering in low stacking-fault energy materials. *Acta Mater* 1999, **47**(15-16)**:** 4187-4196.

256. Wang J, Cao G, Zhang Z, Sansoz F. Size-dependent dislocation–twin interactions. *Nanoscale* 2019, **11**(26)**:** 12672-12679.

257. Wolf D. Structure-energy correlation for grain boundaries in FCC metals—III. Symmetrical tilt boundaries. *Acta metallurgica et materialia* 1990, **38**(5)**:** 781-790.

258. Howie A, Marks L. Elastic strains and the energy balance for multiply twinned particles. *Philosophical Magazine A* 1984, **49**(1)**:** 95-109.

259. Zhu Q, Huang Q, Tian Y, Zhao S, Chen Y, Cao G, *et al.* Hierarchical twinning governed by defective twin boundary in metallic materials. *Sci Adv* 2022, **8**(20)**:** eabn8299.

260. Filleter T, Ryu S, Kang K, Yin J, Bernal RA, Sohn K, *et al.* Nucleation‐controlled distributed plasticity in penta‐twinned silver nanowires. *Small* 2012, **8**(19)**:** 2986-2993.

261. Zinkle S, Ghoniem N. Operating temperature windows for fusion reactor structural materials. *Fusion Engineering and design* 2000, **51:** 55-71.

262. El-Genk MS, Tournier J-M. A review of refractory metal alloys and mechanically alloyed-oxide dispersion strengthened steels for space nuclear power systems. *Journal of Nuclear materials* 2005, **340**(1)**:** 93-112.

263. Perepezko JH. The hotter the engine, the better. *Science* 2009, **326**(5956)**:** 1068-1069.

264. Rao S, Woodward C. Atomistic simulations of (a/2)〈111〉 screw dislocations in bcc Mo using a modified generalized pseudopotential theory potential. *Philosophical Magazine A* 2001, **81**(5)**:** 1317-1327.

265. Yang L, Söderlind P, Moriarty JA. Accurate atomistic simulation of (a/2)〈111〉 screw dislocations and other defects in bcc tantalum. *Philosophical Magazine A* 2001, **81**(5)**:** 1355-1385.

266. Vitek V. Core structure of screw dislocations in body-centred cubic metals: relation to symmetry and interatomic bonding. *Philos Mag* 2004, **84**(3-5)**:** 415-428.

267. Zhang J, Li Y, Li X, Zhai Y, Zhang Q, Ma D, *et al.* Timely and atomic-resolved high-temperature mechanical investigation of ductile fracture and atomistic mechanisms of tungsten. *Nature Communications* 2021, **12**(1)**:** 1-10.

268. Wang SJ, Wang H, Du K, Zhang W, Sui ML, Mao SX. Deformation-induced structural transition in body-centred cubic molybdenum. *Nature Communications* 2014, **5**(1)**:** 1-9.

269. Oshima Y, Kurui Y. In situ TEM observation of controlled gold contact failure under electric bias. *Phys Rev B* 2013, **87**(8)**:** 081404.

270. Zhao J, Sun H, Dai S, Wang Y, Zhu J. Electrical breakdown of nanowires. *Nano letters* 2011, **11**(11)**:** 4647-4651.

271. Stojanovic N, Maithripala D, Berg J, Holtz M. Thermal conductivity in metallic nanostructures at high temperature: Electrons, phonons, and the Wiedemann-Franz law. *Phys Rev B* 2010, **82**(7)**:** 075418.

272. Ahmad I, Khalid S, Khawaja E. Filament temperature of low power incandesecent lamps: Stefan-Boltzmann law. 2010.

273. Chen H, Luo X, Wang D, Ziegler M, Huebner U, Zhang B, *et al.* Length-scale dominated thermal fatigue behavior in nanocrystalline Au interconnect lines. *Materialia* 2019, **7:** 100337.

274. Gumbsch P, Riedle J, Hartmaier A, Fischmeister HF. Controlling factors for the brittle-to-ductile transition in tungsten single crystals. *Science* 1998, **282**(5392)**:** 1293-1295.

275. Wang P, Chou W, Nie A, Huang Y, Yao H, Wang H. Molecular dynamics simulation on deformation mechanisms in body-centered-cubic molybdenum nanowires. *J Appl Phys* 2011, **110**(9)**:** 093521.

276. Cao A. Shape memory effects and pseudoelasticity in bcc metallic nanowires. *J Appl Phys* 2010, **108**(11)**:** 113531.

277. Wang P, Chou W, Nie AM, Huang Y, Yao HM, Wang HT. Molecular dynamics simulation on deformation mechanisms in body-centered-cubic molybdenum nanowires. *J Appl Phys* 2011, **110**(9)**:** 093521.

278. Williams DB, Carter CB. *Transmission Electron Microscopy*, 2 edn. Springer New York: New York, 2009.

279. Nishiyama Z. X-ray investigation of the mechanism of the transformation from face centered cubic lattice to body centered cubic. *Sci Rep Tohoku Univ* 1934, **23:** 637-664.

280. Kurdjumov G, Sachs G. Over the mechanisms of steel hardening. *Z Phys* 1930, **64:** 325-343.

281. Weinberger CR, Cai W. Surface-controlled dislocation multiplication in metal micropillars. *Proc Natl Acad Sci U S A* 2008, **105**(38)**:** 14304-14307.

282. Huang L, Li QJ, Shan ZW, Li J, Sun J, Ma E. A new regime for mechanical annealing and strong sample-size strengthening in body centred cubic molybdenum. *Nat Commun* 2011, **2**(1)**:** 1-6.

283. Sainath G, Choudhary B. Molecular dynamics simulations on size dependent tensile deformation behaviour of [110] oriented body centred cubic iron nanowires. *Materials Science and Engineering: A* 2015, **640:** 98-105.

284. Caillard D. A TEM in situ study of alloying effects in iron. II—Solid solution hardening caused by high concentrations of Si and Cr. *Acta Mater* 2013, **61**(8)**:** 2808-2827.

285. Couzinié J-P, Lilensten L, Champion Y, Dirras G, Perrière L, Guillot I. On the room temperature deformation mechanisms of a TiZrHfNbTa refractory high-entropy alloy. *Materials Science and Engineering: A* 2015, **645:** 255-263.

286. Lei Z, Liu X, Wu Y, Wang H, Jiang S, Wang S, *et al.* Enhanced strength and ductility in a high-entropy alloy via ordered oxygen complexes. *Nature* 2018, **563**(7732)**:** 546-550.

287. Lilensten L, Couzinie J-P, Perriere L, Hocini A, Keller C, Dirras G, *et al.* Study of a bcc multi-principal element alloy: Tensile and simple shear properties and underlying deformation mechanisms. *Acta Mater* 2018, **142:** 131-141.

288. Gröger R, Vitek V. Multiscale modeling of plastic deformation of molybdenum and tungsten. III. Effects of temperature and plastic strain rate. *Acta Mater* 2008, **56**(19)**:** 5426-5439.

289. Kim J-Y, Jang D, Greer JR. Insight into the deformation behavior of niobium single crystals under uniaxial compression and tension at the nanoscale. *Scripta Mater* 2009, **61**(3)**:** 300-303.

290. Schneider A, Kaufmann D, Clark B, Frick C, Gruber P, Mönig R, *et al.* Correlation between critical temperature and strength of small-scale bcc pillars. *Physical review letters* 2009, **103**(10)**:** 105501.

291. Lu Y, Sun S, Zeng Y, Deng Q, Chen Y, Li Y, *et al.* Atomistic mechanism of nucleation and growth of a face-centered orthogonal phase in small-sized single-crystalline Mo. *Mater Res Lett* 2020, **8**(9)**:** 348-355.

292. Li J. The mechanics and physics of defect nucleation. *MRS bulletin* 2007, **32**(2)**:** 151-159.

293. Weidner A. *Deformation Processes in TRIP/TWIP Steels: In-situ characterization techniques*, 1 edn. Springer Cham, 2020.

294. Gröger R, Vitek V. Breakdown of the Schmid law in bcc molybdenum related to the effect of shear stress perpendicular to the slip direction. Materials Science Forum; 2005: Trans Tech Publ; 2005. p. 123-126.

295. Duesbery MS, Vitek V. Plastic anisotropy in bcc transition metals. *Acta Mater* 1998, **46**(5)**:** 1481-1492.

296. Ito K, Vitek V. Atomistic study of non-Schmid effects in the plastic yielding of bcc metals. *Philosophical Magazine A* 2001, **81**(5)**:** 1387-1407.

297. Healy CJ, Ackland GJ. Molecular dynamics simulations of compression–tension asymmetry in plasticity of Fe nanopillars. *Acta Mater* 2014, **70:** 105-112.

298. Sainath G, Choudhary B, Jayakumar T. Molecular dynamics simulation studies on the size dependent tensile deformation and fracture behaviour of body centred cubic iron nanowires. *Computational Materials Science* 2015, **104:** 76-83.

299. Sainath G, Choudhary B. Atomistic simulations on ductile-brittle transition in⟨ 111⟩ BCC Fe nanowires. *J Appl Phys* 2017, **122**(9)**:** 095101.

300. Christian JW, Mahajan S. Deformation twinning. *Progress in materials science* 1995, **39**(1-2)**:** 1-157.

301. Xu S, Su Y, Chen D, Li L. An atomistic study of the deformation behavior of tungsten nanowires. *Applied Physics A* 2017, **123**(12)**:** 1-9.

302. Wang J, Mao SX. Atomistic perspective on in situ nanomechanics. *Extreme Mechanics Letters* 2016, **8:** 127-139.

303. Coble R. A model for boundary diffusion controlled creep in polycrystalline materials. *J Appl Phys* 1963, **34**(6)**:** 1679-1682.

304. Lu L, Sui ML, Lu K. Superplastic extensibility of nanocrystalline copper at room temperature. *Science* 2000, **287**(5457)**:** 1463-1466.

305. Yamakov V, Wolf D, Phillpot SR, Gleiter H. Grain-boundary diffusion creep in nanocrystalline palladium by molecular-dynamics simulation. *Acta Mater* 2002, **50**(1)**:** 61-73.

306. Tian L, Li J, Sun J, Ma E, Shan ZW. Visualizing size-dependent deformation mechanism transition in Sn. *Sci Rep-Uk* 2013, **3:** 2113.

307. Li J, Sarkar S, Cox W, Lenosky T, Bitzek E, Wang Y. Diffusive molecular dynamics and its application to nanoindentation and sintering. *Phys Rev B* 2011, **84**(5)**:** 054103.

308. Li J. Dislocation nucleation: Diffusive origins. *Nat Mater* 2015, **14**(7)**:** 656-657.

309. Zhong L, Sansoz F, He Y, Wang C, Zhang Z, Mao SX. Slip-activated surface creep with room-temperature super-elongation in metallic nanocrystals. *Nat Mater* 2017, **16:** 439-445.